



**INSTITUTO POTOSINO DE INVESTIGACIÓN
CIENTÍFICA Y TECNOLÓGICA, A.C.**

POSGRADO EN CIENCIAS APLICADAS

**Electronic transport and mechanical
properties in nanostructures**

Tesis que presenta

Samuel Eliazar Baltazar Rojas

Para obtener el grado de

Doctor en Ciencias Aplicadas

En la opción de

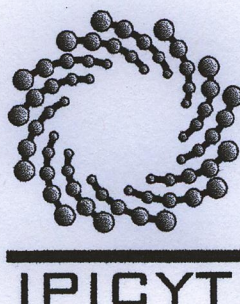
Nanociencias y Nanotecnología

Codirectores de la Tesis:

Dr. Martín E. García

Dr. Aldo H. Romero Castro

Dr. Roman López Sandoval



Constancia de aprobación de la tesis

La tesis titulada **Electronic transport and mechanical properties in nanostructures**, presentada para obtener el Grado de Doctor en Ciencias Aplicadas en la opción de Nanociencias y nanotecnología fue elaborada por **Samuel Eliazar Baltazar Rojas** y aprobada el **29 de agosto de 2007** por los suscritos, designados por el Colegio de Profesores de la División de Materiales Avanzados del Instituto Potosino de Investigación Científica y Tecnológica, A.C.

Dr. Martín E. García

Dr. Roman López Sandoval

Dr. Aldo H. Romero

Esta tesis fue elaborada en el Departamento de Materiales Avanzados para la Tecnología Moderna del Instituto Potosino de Investigación Científica y Tecnológica, A. C., y el instituto de Física de la Universidad de Kassel, Alemania, bajo la codirección de Dr. Aldo H. Romero, Dr. Roman López S. y Dr. Martin E. García.

Durante la realización del trabajo, el autor recibió una beca académica del Instituto Potosino de Investigación Científica y Tecnológica, A. C. así como una beca del DAAD (Alemania) por una estancia de investigación y finalmente el apoyo dado por Consejo Nacional de Ciencia y Tecnología a los proyectos: CONACYT–México J42647-F, J42645-F DFG– Alemania SPP1153.



IPICYT

Instituto Potosino de Investigación Científica y Tecnológica, A.C.

Acta de Examen de Grado

El Secretario Académico del Instituto Potosino de Investigación Científica y Tecnológica, A.C., certifica que en el Acta 023 del Libro Primero de Actas de Exámenes de Grado del Programa de Doctorado en Ciencias Aplicadas en la opción de Nanociencias y Nanotecnología está asentado lo siguiente:

En la ciudad de San Luis Potosí a los 29 días del mes de agosto del año 2007, se reunió a las 11:00 horas en las instalaciones del Instituto Potosino de Investigación Científica y Tecnológica, A.C., el Jurado integrado por:

Dr. Román López Sandoval	Presidente	IPICYT
Dr. Aldo Humberto Romero Castro	Secretario	CINVESTAV-Qro
Dr. Jesús Dorantes Dávila	Sinodal externo	UASLP
Dr. José Luis Rodríguez López	Sinodal	IPICYT
Dr. Martín García	Sinodal externo	University of Kassel

a fin de efectuar el examen, que para obtener el Grado de:

**DOCTOR EN CIENCIAS APLICADAS
EN LA OPCIÓN DE NANOCIENCIAS Y NANOTECNOLOGÍA**

sustentó el C.

Samuel Eliazar Baltazar Rojas

sobre la Tesis intitulada:

Electronic Transport and Mechanical Properties of Nanostructures

que se desarrolló bajo la dirección de

Dr. Román López Sandoval
Dr. Aldo Humberto Romero Castro (CINVESTAV-Qro.)
Dr. Martín García (University of Kassel)

El Jurado, después de deliberar, determinó

APROBARLO

Dándose por terminado el acto a las 13:00 horas, procediendo a la firma del Acta los integrantes del Jurado. Dando fé el Secretario Académico del Instituto.

A petición del interesado y para los fines que al mismo convengan, se extiende el presente documento en la ciudad de San Luis Potosí, S.L.P., México, a los 29 días del mes agosto de 2007.

L.C.C. Ivonne Lizette Cuevas Velez
Jefa del Departamento de Asuntos Escolares

Dr. Marcial Bonilla Marín
Secretario Académico



Propiedades mecánicas y de transporte electrónico en nanoestructuras

Mtro. Samuel Baltazar Rojas

Agosto, 2007

Resumen

El trabajo de investigación doctoral se ha desarrollado sobre transporte electrónico en moléculas orgánicas e inorgánicas y sobre el estudio de propiedades mecánicas en nanoestructuras bajo presión. Para la primera parte se ha considerado un modelo Huckel extendido (EHT) y cálculos de primeros principios (LSDA) para describir agregados de silicio ($\text{Si}_{29}\text{H}_{24}$) y moléculas orgánicas (styrene, biphenyl). Fenómenos de transporte son estudiados usando EHT y el formalismo de funciones de Green fuera de equilibrio. La importancia de la interacción agregado-superficie es estudiada así como el control de la conductancia a través de, por ejemplo, dopamiento de superficies, distorsión estructural de la molécula, efecto de punta STM, etc. Fenómenos asociados a dispositivos electrónicos, como diodos o el efecto de resistencia negativa, han sido encontrados en estas moléculas y métodos de control son además presentados. Estos resultados refuerzan la idea de poder utilizar moléculas orgánicas e inorgánicas como dispositivos electrónicos a escala atómica. Además se ha utilizado un modelo clásico para estudiar la respuesta mecánica de nanoestructuras como nanotubos de carbono bajo una presión externa encontrando transiciones estructurales a fases estables y metaestables.

Copyright © 2007 por Samuel Baltazar Rojas.

Electronic transport and mechanical properties in nanostructures

Msc. Samuel Baltazar Rojas

Submitted for the degree of Doctor in Applied Sciences

August, 2007

Summary

The doctoral research has been developed considering the electronic transport in organic and inorganic molecules and the study of mechanical properties in nanostructures under pressure. The first part considers the extended Huckel model (EHT) and first principle calculations (LSDA) to describe silicon clusters ($\text{Si}_{29}\text{H}_{24}$) and organic molecules (styrene, biphenyl). The electronic transport regime is modeled with the EHT approach and the formalism of non equilibrium Green functions. The importance of the cluster-surface interaction is studied as well as the control of the conductance by doping effect on surfaces, structural distortions of molecules, STM tip effect, etc. Several phenomena associated to electronic devices such as diode effect or negative differential resistance have been found in these molecules and control methods are also presented in this work. The obtained results reinforce the idea of using organic and inorganic molecules as electronic components at atomic scale. Besides this, we have used a classical model to study the mechanical response of nanostructures such as carbon nanotubes under an external pressure finding structural transitions to stable and metastable configurations.

Copyright © 2007 by Samuel Baltazar Rojas.

Acknowledgments

I would like to express my thankful to my advisors, Dr. Aldo Humberto Romero due to its numerous advices every day by e-mail or in person that helped to me to finish this work on time, and also Dr. Martin E. García for all the fruitful discussions about the study of electronic transport in molecules and the support that he gave me, in particular, during my research stay in Kassel, Germany. Also to Dr. Mario De Menech who allowed me to work with him in the theoretical study of charge transport in molecules and to use his code and develop some applications and for the discussion that helped me to get a better understanding about this topic.

I also would like to express my gratefully acknowledge Dr. Roman López S. and Dr. Mauricio Terrones M. for the recomendations and discussions to prepare the tesis on time.

I am also grateful for the fruitful discussion with Dr. Jose Luis Rodríguez-López and Dr. Ulf Saalman who contributed to the discussion and analysis of the results obtained during my research. At this point, I would like to thank the support given to me from my classmates and the rest of the Advanced Materials Department and the Institut für Physik der universität Kassel (researchers and technicians).

Finally, I would like to thank to my family, whose in spite of the distance, always have given to me their best wishes and support.

*Dedicated to my parents
Camilo and Juana,
and all my family*

Contents

1	Introduction	1
1.1	State of the art	1
1.2	Motivation	2
1.3	Objectives	3
	References I	3
2	Theoretical background	7
2.1	Introduction	7
2.2	Historical remarks	7
2.3	Green's functions	8
2.4	Molecule-reservoir interactions	10
2.5	Hamiltonian	14
2.6	Electron-phonon case	16
2.7	Semiclassical approximation (WKB)	19
2.8	Potential I	20
2.8.1	Density Matrix	21
	References II	23
3	Silicon cluster on semiconductor surfaces	26
3.1	Introduction	26
3.2	Surfaces	27
3.2.1	Si[111] surface	28
3.2.2	Si[111] surface saturated with H atoms	29
3.2.3	Si[100] surface	30

3.2.4	Si[100] surface saturated with H atoms.	32
3.3	Atomic clusters	33
3.3.1	Si ₂₉ H ₂₄ cluster	33
3.3.2	Molecular Orbitals and charge density	35
3.4	Cluster-surface interaction	39
3.4.1	Displacement effect	42
3.4.2	Modified cluster on Si[111]	43
3.4.3	Local density	44
3.4.4	Doped surfaces	46
3.5	Part III: Transport properties	48
3.5.1	Si ₂₉ H ₂₄ on Si[111]	48
3.5.2	Discussion	54
3.5.3	Si ₂₉ H ₂₄ on Au[111]	55
3.6	Conclusions	59
	References III	59
4	Transport properties in organic molecules	62
4.1	Introduction	62
4.2	Components	64
4.2.1	Surface	64
4.2.2	Styrene molecule	64
4.3	Molecule-surface Interaction	67
4.3.1	First configuration (case A)	67
4.3.2	Transport properties	69
4.3.3	Second configuration (case B)	73
4.4	Electronic transport in molecules as a function of the conformation	78
4.5	Discussion and Conclusions	81
	References IV	84
5	Nanostructures under hydrostatic pressure	86
5.1	Introduction	86
5.2	Simulation method	89

Contents	iii
5.3 Results	90
References V	99
6 Conclusions	105
6.1 Future work	107
References VI	109

List of Figures

2.1	Schematic diagram of the system	8
2.2	Diagram of the (a)isolated and (b) coupled molecule-contact system .	11
2.3	Characteristic distribution of states of the system	14
2.4	Potential	20
3.1	Si(111) surface	28
3.2	Configuration and band structure for Si(111)-H	29
3.3	Si(111)-H: Band structure	30
3.4	Si(100)	30
3.5	Si(100): Band structure	31
3.6	Si(100)- H_2	32
3.7	silicon cluster	34
3.8	Molecular orbitals	35
3.9	charge density of HOMO level	36
3.10	Total density	36
3.11	Cluster II	37
3.12	Molecular orbital II	38
3.13	Total density II	38
3.14	DOS of cluster on Au(111)	39
3.15	DOS of cluster on Si(100)	40
3.16	DOS of cluster II on Si(111)	41
3.17	DOS of cluster on Si(111) II	42
3.18	DOS of cluster on Si(111) III	43
3.19	DOS of cluster II on Si(111)	44

3.20	Local charge density I	45
3.21	Local charge density II	46
3.22	Doped surfaces	47
3.23	substrate- cluster- metallic electrode	49
3.24	DOS of cluster on Si[111]	50
3.25	total	51
3.26	Charge density	52
3.27	Changed density	53
3.28	Calculated current through the surface-molecule-electrode system considering doped surfaces (n-type and p-type).	54
3.29	Electronic configuration for the isolated cluster and surface and the coupled Au[111]- Si ₂₉ H ₂₄ system.	56
3.30	Molecular orbitals for supported Si ₂₉ H ₂₄ . Charge densities previously associated with HOMO (A) and LUMO (B) levels are shown.	56
3.31	Current as a function of the applied bias.	57
3.32	Charge distribution of the peak B of fig.3.30 as a function of the applied voltage.	58
3.33	DOS and transmittance for the supported Si ₂₉ H ₂₄ at different applied voltages.	58
4.1	Styrene A	65
4.2	Molecular orbitals for Styrene A	66
4.3	Styrene B	66
4.4	Molecular orbitals for Styrene B	67
4.5	DOS for C ₈ H ₈ A	68
4.6	I-V characteristics for C ₈ H ₈ -A	69
4.7	Partial DOS and Transmittance for C ₈ H ₈ -A	70
4.8	Total DOS and dI/dV for C ₈ H ₈ -A	71
4.9	Doped surfaces: I vs V	72
4.10	DOS and dI/dV characteristics	72
4.11	I-V characteristic considering tips	73
4.12	DOS and dI/dV considering tips	74

4.13	DOS for C_8H_8 -B	75
4.14	I-V characteristics for C_8H_8 -B	75
4.15	Total DOS and dI/dV for C_8H_8 -B	76
4.16	I-V characteristics for doped surfaces	77
4.17	DOS and dI/dV characteristics for doped surfaces	77
4.18	I-V characteristic considering tips for styrene B	78
4.19	Biphenyl molecule	79
4.20	I-V curve for Biphenyl molecule	80
4.21	dI/dV curve for Biphenyl molecule	81
5.1	Adapted convex volume definition	89
5.2	Nanotube (10,10) at different pressures	91
5.3	Cross sectional area as a function of pressure	94
5.4	Volume as a function of applied pressure	95
5.5	Transition pressure as a function of the tube diameter	96

Chapter 1

Introduction

1.1 State of the art

The industry based on semiconductors has experienced a dramatic development during the last decades in order to achieve the construction of faster and smaller electronic devices. That this development has been characterized by Moore's law that has established that the number of transistors per chip doubles every 2 years [1]. According to this prediction, the technology based in semiconductors was fueled to develop new electronics devices with higher performances, energy efficiency and capability to concentrate integrated transistors until reaching the forthcoming limits where a silicon chip of 45 nm is intended to be produced at the industrial scale [2]. In addition, as the silicon industry comes close to the design of components at atomic scale, it is necessary to explore other directions about miniaturization at atomic levels. The study of molecular devices provides us with the great opportunity to understand the behavior and the properties of physical systems at the nanoscopic scales. For instance, the concept of resistance has to be adjusted at small scales because electrons flow through a conductor in the ballistic regime in which the resistance becomes independent of the length of the system.

Physical understanding of systems at a small scale has considerably increased a lot in the last few years due to the potential applicability in areas such as microelectronics [3–7], optoelectronics [8–10], biology [11, 12], etc.

There are several well developed approaches for the transport properties at the

mesoscopic scale starting with the Landauer formula in the middle of the 20th century [13]. However, if we want to consider a more general theory that allows electronic interactions, high applied voltage, time dependent situations, etc., it is necessary to introduce and develop different set of tools which allow to take a system and bring it adiabatically out of equilibrium situation. In this context, Green's functions have been introduced, mainly because of the applicability to non-equilibrium situations [14–16]. Nowadays, we can find this technique applied, within tight-binding [17, 18] or ab-initio calculations [19], to the study of several mesoscopic systems, such as carbon nanotubes [20, 21], nanowires [3, 22–24], electromechanical devices [8, 25], biological systems such as DNA molecules [11, 12, 26–28], etc. We have also continued working in the project about nanostructures under an external pressure. This project contains the study of several nanostructures such as single walled carbon nanotubes, fullerenes and metallic clusters and the study is based in a classical molecular dynamics approach.

1.2 Motivation

Studies related to electronic properties in small systems has been recently enhanced due to many possible applications in electronics, biology, etc. In particular, the conductance in molecules interacting with surfaces has been studied because these systems with discrete levels and electronic band structures could be used to control charge transport. This can be understood in the same way as the nanotransistors that allow charge transfer at some specific voltages.

In addition, doping surfaces is another related mechanism to control electronic transport and therefore considering surfaces and molecules as active compound in these process.

We have been developing our code to study finite systems under pressure and in particular considering carbon nanotubes to examine the mechanical response of these systems under an external hydrostatic pressure.

1.3 Objectives

The main goal of this doctoral project is to develop and apply theoretical tools to study electronic transport through molecular systems. In order to accomplish this goal, it is necessary to achieve some previous steps. Some of these steps are:

- Understanding the theoretical tools in electronic transport processes. In particular, we are interested in describing these phenomena using the non-equilibrium Green's functions technique (NEGF) as well as a classical method to determine the flux of electrons at high temperatures.
- Describe and calculate properties such as resistance, charge density variations, current as a function of applied voltages, etc. of 1-D and 2-D systems. These properties can be evaluated both at equilibrium and non-equilibrium situations.
- Investigate the behavior of properties in isolated and coupled systems, specially the interaction between clusters and surfaces. At the beginning, we focus the study of surfaces such as semiconductors and non-organic molecules.
- Introducing organic molecules, between electrodes in order to see the behavior of the conductivity associated with them.
- Examine the effect produced by distortion in molecules on the transport properties due to the natural molecular vibrations.
- Investigate nanostructures, such as single walled carbon nanotubes, under hydrostatic pressure and temperature in order to search for structural transitions, and compare the results with published data.

Bibliography

- [1] G. E. Moore. Cramming more components onto integrated circuits. *Electronics*, 38:8, 1965.
- [2] G. E. Moore. Moore's law, 2007.
- [3] N. Agrait, A. L. Yeyati, and J. M. Ruitenbeek. *Phys. Rep.*, 377:81, 2002.
- [4] R. N. Barnett and U. Landman. Cluster-derived structures and conductance fluctuations in nanowires. *Nature*, 387:788, 1997.
- [5] M. L. Roukes, A. Scherer, Jr. S. J. Allen, H. G. Craighead, R. M. Ruthen, E. D. Beebe, and J. P. Harbison. Quenching of the Hall effect in a one-dimensional wire. *Phys. Rev. Lett.*, 59:3011, 1987.
- [6] M. De Menech, U. Saalman, and M. E. Garcia. Calculation of conductance spectra of Silver clusters on Graphite. *Appl. Phys. A*, 2005. DOI: 10.1007/s00339-005-3346-6.
- [7] M. De Menech, U. Saalman, and M. E. Garcia. Energy-resolved stm mapping of c-60 on metal surfaces: A theoretical study. *Phys. Rev. B*, 73:155407, 2006.
- [8] V. Meunier and Ph. Lambin. *Phys. Rev. Lett.*, 81:5588, 1998.
- [9] R. Wiesendanger. *Scanning probe microscopy and spectroscopy*. Cambridge University Press, 1994.
- [10] S. Datta, W. Tian, S. Hong, R. Reifenberger, J. I. Henderson, and C. P. Ku-biak. Current-voltage characteristics of self-assembled monolayers by scanning tunneling microscopy. *Phys. Rev. B*, 79:2530, 1997.

-
- [11] H. F. Fink and C. Schonenberger. Electrical conduction through DNA molecules. *Nature*, 398:407, 1999.
- [12] A. Yu., Kasumov, M. Kociak, S. Guéron, B. Reulet, V. T. Volkov, D. V. Klinov, and H. Bouchiat. Proximity induced superconductivity in DNA. *Science*, 291:280, 2001.
- [13] R. Landauer. *J. Res. Dev.*, 1:233, 1957.
- [14] Y. Meir and N.S. Wintergreen. Landauer formula for the current through an interacting electron region. *Phys. Rev. Lett.*, 68:2512, 1992.
- [15] H. Haug and A. P. Jauho. *Quantum Kinetics in Transport and Optics of Semiconductors*. Springer–Verlag, 1996.
- [16] A. Jauho, N. S. wingreen, and Y. Meir. Time-dependent transport in interacting and non-interacting resonant-tunneling systems. *Phys. Rev. B*, 50:5528, 1994.
- [17] Y. Ko, M. Shin, J. S. Ha, and K. W. Park. Green-function calculations of coherent electron transport in a gated Si nanowire. *ETR Journal*, 22:19, 2000.
- [18] T. N. Todorov. Tight-binding simulation of current-carrying nanostructures. *J. Phys.:Condens. Mater.*, 14:3049, 2002.
- [19] D. S. Kosov. Khon-Sham equations for nanowires with direct current. *J. Chem. Phys.*, 119:1, 2003.
- [20] M. Buongiorno Nardelli. Electronic transport in extended systems: Application to carbon nanotubes. *Phys. Rev. B*, 60:7828, 1999.
- [21] M. Buongiorno N. and J. Bernholc. Mechanical deformation and coherent transport in nanotubes. *Phys. Rev. B*, 60:R16338, 1999.
- [22] A. Tikhonov, R. D. Coalson, and Y. Dahnovsky. Calculating electron transport in a tight-binding model of a field driven molecular wire: Floquet theory approach. *J. Chem. Phys.*, 116:10909, 2002.

-
- [23] P. S. Damle, A. W. Ghosh, and S. Datta. Unified description of molecular conduction: from molecules to metallic wires. *Phys. Rev. B*, 64:201403, 2001.
- [24] A. Haque and A. N Khondker. Quantum transport in mesoscopic devices: current conduction in quantum wire structures. *J. Appl. Phys.*, 87:2553, 2000.
- [25] S. A. Crooker, J. A. Hollingsworth, S. Tretiak, and V. I. Klimov. *Phys. Rev. Lett.*, 89:186802, 2002.
- [26] M. A. Reed, C. Zhou, C. J. Muller, T. P. Burgin, and J. M. Tour. Driving current through single organic molecules. 278:252, 1997.
- [27] J. Chen, M. Reed, A. M. Rawlett, and J. M. Tour. Large on-off ratios and negative differential resistance in a molecular electronic device. *Science*, 286:1550, 1999.
- [28] S. Ranganathan, I. Steidel, F. Anariba, and R. L. McCreery. Covalently bonded monolayers on a carbon substrate: a new paradigm for molecular electronics. *Nano Letters*, 1:491, 2001.

Chapter 2

Theoretical background

2.1 Introduction

Since the middle of the 20th century, the scientific literature in the area of electronic transport has been growing at steady pace. One of the main difficulties was how to obtain the experimental measures of the transport properties. In 1982, the appearance of the scanning tunneling microscopy allowed the possibility to obtain images at atomic scale of both surfaces and molecules. Since then, the equipment has been developed to measure not only the atomic configuration of the systems but also to get the local electronic properties in a spectroscopical approach.

In this chapter, we are going to present the theoretical tools that are necessary to understand the quantum transport and calculate transport properties in molecular systems. The first part is a review of the different approaches that have been developed during the last decades. One important tool is the Green's function which have been extensively used in this topic to study systems and to individualize properties related to some specific components of a given system.

2.2 Historical remarks

Mechanical and electronic properties at macroscopic scale have been described and supported by several classical laws. For example, conduction phenomenon can be

described based on the Ohm's law

$$G = \frac{\sigma S}{L} ,$$

where σ corresponds to the electronic conductivity of a sample. It is a general fact that the conductance G depends on parameters such as the cross section S and the length L of the sample. However, some limitations are found at small scales, where quantum phenomena become more important. In this case, a more appropriated description is given by the Landauer formula:

$$G = \frac{2e^2}{h} MT ,$$

where M is the number of transversal modes and T is the probability that the electron can flow through out a conductor. In Fig. 2.1, we can see a schematic system (electronic reservoirs, leads and a central region). By using this definition, it is possible to find a finite resistance for small conductors that is quite different from the macroscopic concept.

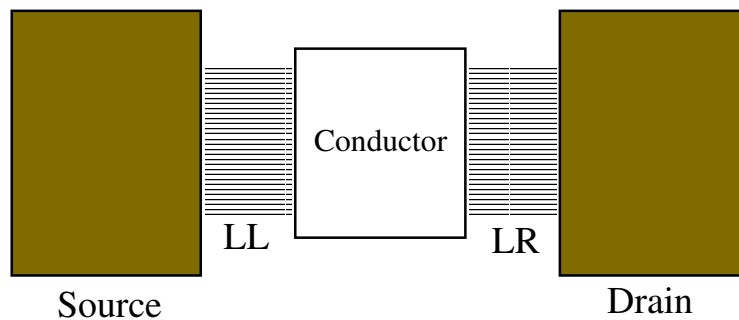


Figure 2.1: Schematic diagram for a mesoscopic system. LL and LR represent the left and right contacts and the Source and Drain are the electronic reservoirs at different chemical potential μ_1 and μ_2 .

2.3 Green's functions

A different approximation to study transport properties can be developed by considering Green's functions. These functions have been previously considered in classical

physics, to solve inhomogeneous differential equations (like Poisson's equation), but in our study, they are useful in the many body theory because it is possible to use them like solutions of a wave equation with an (inhomogeneous) singularity. Moreover, Green's functions are a strong tool to evaluate physical properties in many body systems at equilibrium as well as non-equilibrium conditions [1–3]. As an example, in the case of a system with non-interacting electrons, important excitations come from the leads that connect electronic reservoirs with the conductor. However, the power of these functions becomes more evident when electron-electron or electron-phonon interactions are taken into account.

At equilibrium, in principle only one function is needed, for example, the time-ordered Green's function for single particle at zero temperature

$$G(x, t; x', t') = -\frac{i}{\hbar} \frac{\langle \Psi_o | T \{ \Psi_H(x, t) \Psi_H^\dagger(x', t') \} | \Psi_o \rangle}{\langle \Psi_o | \Psi_o \rangle} .$$

In this case, Ψ_o are eigenfunctions (which are obtained, for example, by tight-binding calculations). Furthermore, we can generalize this expression for finite temperatures as follows:

$$G(x, t; x', t') = -\frac{i}{\hbar} Tr \{ \rho T \Psi_H(x, t) \Psi_H^\dagger(x', t') \} ,$$

where ρ is the density matrix operator and T is the time-ordered operator. Besides this function, other ones can be defined: *advanced* (G^a), *retarded* (G^r), *lesser* ($G^<$) and *greater* ($G^>$). These functions are recommended to calculate the physical response of a system or to calculate observable and kinetic properties. If we want to consider a mesoscopic device in a non-equilibrium case, for example when a large voltage is applied, or when the device is under a non-uniform electric field, an extension of these Green's functions is necessary. Nevertheless, non-equilibrium Green's functions theory (NEGF) has a structure similar to the $T = 0$ case at equilibrium [4–6]. NEGF are defined as expectation values of creation and annihilation operators of particles (quasiparticles) and describe the state and time evolution of a system. Interactions between subsystems can be represented by Σ terms, which include: carrier-impurity dispersion, phonon dispersion, carrier-carrier dispersion, etc. In general, Green's functions are determined by solving a set of Dyson's equations; which are integral or differential forms of the Schrodinger equation. The integral

representation of the Schrödinger equation

$$\begin{aligned} & \left\{ i \frac{\partial}{\partial \tau_1} - \left[-\frac{1}{2} \nabla_{x_1}^2 + U(x_1, \tau_1) \right] \right\} G(x_1, \tau_1, x_{1'}, \tau_{1'}) \\ & = \delta(1 - 1') + \int_C d\sigma \int d^3y \Sigma(x_1, \tau_1, y, \sigma) G(y, \sigma, x, \tau_1) \end{aligned} \quad (2.1)$$

is convenient to apply for a perturbative expansion of the solutions.

If we consider the integral form (Keldysh method) [4], motion equations of Green's functions, like *lesser* function $G^<$ are solved like

$$G^< = (1 + G^r \Sigma^r) G_o^< (1 + \Sigma^a G^a) + G^r \Sigma^< G^a \quad ,$$

where the advanced and retarded functions are given by

$$G^{r,a} = G_o^{r,a} + G_o^{r,a} \Sigma^{r,a} G^{r,a} \quad .$$

2.4 Molecule-reservoir interactions

Here we describe the applied electronic transport method that has been followed, which is very close to that one given by Datta [7]. In order to describe the entire system (substrate-molecule-electrode) we have considered that all compounds remain fixed after the adsorption of the molecule on the surface. Transport properties at equilibrium and non-equilibrium conditions were calculated using a Green's functions approach, and describing the electronic properties by means of a semiempirical extended Hückel theory (EHT), where the parameters are obtained from first principle calculations.

From the Hamiltonian of a molecule H_{mol} and a contact H_C , a coupled system (contact C - molecule) can be described by the composite Schrödinger equation: In the case of isolated systems (Fig. 2.2a), we can write the Schrödinger equation for the molecule:

$$E\{\psi\} = [H_{mol}]\{\psi\} \quad ,$$

where the electrons are associated to eigenfunctions ψ , and the contact part

$$E\{\Phi\} = [H_C]\{\Phi\}$$

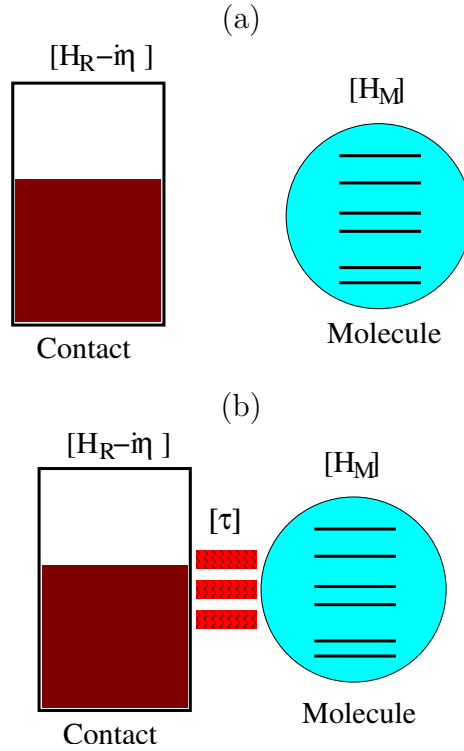


Figure 2.2: Diagram of the (a) isolated and (b) coupled molecule-contact system with corresponding eigenfunctions $\{\Phi\}$. We can rewrite the last equation adding the infinitesimal term $[\eta]$,

$$[EI_C - H_C + i\eta]\{\Phi\} = \{S_C\}$$

coming from the contact equation ($[EI_C - H_C]\{\Phi_R\} = \{S_R\}$), that estimates the quantity of electrons going out from the contact. In the same way, S_R takes into account the entrance of electrons to the contact.

From the Hamiltonians of the molecule H_{mol} and the contact H_C , a coupled system (contact C - molecule) can be described by the composite Schrödinger equation

$$[(E + i\eta)S - H]G(E) = 1, \quad \eta \rightarrow 0^+ \quad (2.2)$$

where S is the normalization matrix and G is the Green function approach of the total system. By using the function G , the spectral function (density of states per unit energy) can be written as

$$A(E) = -\frac{2}{\pi} \text{Im}[G(E)] \quad (2.3)$$

for the spin unpolarized case. Following this description, the local density of states can be written as

$$\rho(r, E) = \sum_{\mu\nu} A_{\mu\nu}(E) \psi_\mu \psi_\nu \quad , \quad (2.4)$$

where the ψ s are the molecular wavefunctions, giving rise to the electronic density as

$$n(r) = \int_{-\infty}^{E_F} dE \rho(r, E) \quad (2.5)$$

that considers the integration just until the Fermi energy level. Now, if we want to study the consequences on a specific part of the system due to the presence of the other parts, the Green function approach allows it by including the effect as perturbations on the original Green function. This approach has been described by Williams *et al.* [8] to study defects in crystals as perturbations. They have shown that the problem can be described by a Dyson equation and have obtained the Green function of the perturbed system. In our case, the Dyson equation leads to the perturbed Green's function of the cluster due to the presence of the surface. The surface effects are included as

$$G(E) = G^0(E) + G^0(E) \Sigma G(E) \quad (2.6)$$

where G^0 and G are the Green functions associated with the isolated (unperturbed part) and the supported cluster (perturbed) respectively, and Σ is the self-energy matrix given by:

$$\Sigma = \tau G_s^0(E) \tau^\dagger \quad . \quad (2.7)$$

The previous equation takes into account the effect of the surface, which could come as broadening and shifting of molecular energy levels (the size of G , G^0 and Σ are defined mainly from the molecular orbitals values). The term $G_s^0(E)$ corresponds to the Green function of the isolated surface and τ is the coupling matrix between the cluster and the surface. The non-equilibrium regime is considered when another electrode is added to the system and an external voltage is applied between the surface and the electrode. In this case, the representation for the supported cluster is changed by using the correlation function $G^< = G \Sigma^< G^<$ to determine the charge density at a specific bias V . The term $\Sigma^< = i(f(E - \mu_s) \Gamma^s + f(E - \mu_e) \Gamma^e)$ is the lesser

self-energy that depends on the chemical potential μ and the broadening matrix Γ of the surface and the metallic electrode.

Now, generalizing for the total system (surface+molecule+electrode), the interactions of the molecule with the surface and the electrode are given by their self-energies matrices Σ_i , so the molecule Green function can be written as:

$$G = [(E + i0^+)I - H - \Sigma_s - \Sigma_e]^{-1} \quad , \quad \text{where} \quad \Sigma_{s,e} = \tau_{s,e} G_{s,e} \tau_{s,e}^\dagger \quad , \quad (2.8)$$

considering that surface and electrode are in equilibrium at different chemical potentials μ_1 and μ_2 . The correlation function G^n , the matrix version of the electron density per unit energy, can be obtained from the partial spectral functions A_i as

$$[G^n] = [A_s]f_s + [A_e]f_e, \quad (2.9)$$

where

$$A_s = G\Gamma_s G^\dagger \quad \text{and} \quad A_e = G\Gamma_e G^\dagger \quad (2.10)$$

are the components of the total spectral function $A = A_s + A_e$. Considering the imaginary part of the self-energy matrices, we can define the broadening of energy levels due to the contacts, such as:

$$\Gamma^{s,e} = i[\Sigma^{s,e} - \Sigma^{s,e\dagger}] . \quad (2.11)$$

The rate at which electrons goes from one contact to another through the molecule is the transmittance $T(E, V)$. By considering coherent transport (without scattering processes) $T(E, V)$ can be evaluated using the relation

$$T \equiv Tr[\Gamma^s G \Gamma^e G^\dagger]. \quad (2.12)$$

Finally, the expression used to calculate the current through a system like the one depicted in Fig. 2.3, where a molecule, with discrete energy levels, is located between a semiconductor surface and an electrode (with a uniform distribution of states), can be written as

$$I = \frac{2e}{h} \int_{-\infty}^{\infty} dE T(E) [f_1 - f_2]. \quad (2.13)$$

The transmittance $T(E)$ is integrated in the energy interval associated with each applied bias voltage and $f_i = f(E - \mu_i)$ is the Fermi function of the contact i for a

specific chemical potential. For both cases (surface and electrode) local equilibrium is assumed and, in principle, the low temperature approximation is used, so the integration can be performed between μ_1 and μ_2 .

After this calculation of the transmittance and following the treatment given by

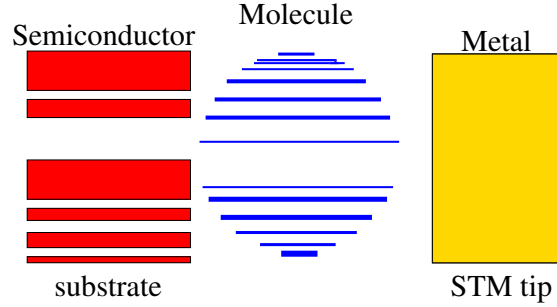


Figure 2.3: Schematic configuration of the system substrate-molecule-electrode system showing the characteristic distribution of electronic states.

Tian *et al.* [9], the differential conductance can be obtained, for low temperatures, as a function of the calculated transmittance at a specific voltage bias

$$\frac{dI}{dV} \approx G_0 T(E_f + eV), \quad (2.14)$$

where $G_0 = 2e^2/h$ is the maximum conductance parameter and assuming that the electrostatic potential mainly modifies the chemical potential of the metallic electrode.

2.5 Hamiltonian

Two different approaches have been considered to describe the system (contacts+molecule). The first one corresponds to a tight-binding approach where the parameters were fixed from first principle calculations, and the second one considers a quantum description of the system where electron-phonon interactions are considered.

For the first case, the Hamiltonian has been defined using the extended Hückel method (EHT), where the Hamiltonian matrix elements $H_{\alpha i, \beta j}$ between two atomic orbitals α and β of atoms i and j respectively were approximated to be proportional to the overlap $O_{\alpha i, \beta j}$ and such that $H_{\alpha i, \beta j} = K_{\alpha i, \beta j} \cdot O_{\alpha i, \beta j}$. According to Cerda *et al.*,

the parameter $K_{\alpha i, \beta j}$ can be defined using the form: $K_{\alpha i, \beta j} = K_{EHT} \cdot (E_{\alpha i} + E_{\beta j})/2$. The atomic orbitals have been defined from Slater-type functions (STF) and spherical harmonics:

$$X_{nlm}(r, \theta, \phi) = s_{n\zeta}(r)Y_{lm}(\theta, \phi) \quad (2.15)$$

where

$$s_{n\zeta}(r) = \frac{(2\zeta)^{n+1/2}}{\sqrt{(2n)!}} r^{n-1} e^{-\zeta r} \quad (2.16)$$

and the spherical harmonic is given by

$$Y_{\theta, \phi} = \sqrt{\frac{2l+1}{4\pi} \frac{(l-m)!}{(l+m)!}} e^{im\phi} (1-\theta^2)^{m/2} \theta^{l-m} \\ \times \sum_{p=0,2,\dots}^{l-m} \frac{(2l-1-p)!! (-1)^{p/2}}{(l-m-p)! p!!} \theta^{-p} .$$

The parameter K_{EHT} , the exponents and the coefficients of the Slater-type functions are summarized in table 2.1 for the case of Si and H atoms that have been considered in the first part of the project, where the parameters have been setted comparing energy levels with other theories like local density approximation (LDA) and gradient generalized approximation (GGA).

For the second part, the Hamiltonian can be also described for the entire system (see figure 2.1), where the tunneling is explicitly described like $H = H_c + H_t + H_{cen}$:

$$H = \sum_{k, \alpha \in L/R} \epsilon_{k, \alpha} a_{\alpha, k}^\dagger a_{\alpha, k} \\ + \sum_{\alpha \in L/R; k, \sigma, i=1, d_g} \left[t_{i, k, \alpha} \{ \hat{x} \} a_{\alpha, k}^\dagger d_{i, \sigma} + H.c. \right] + H_{cen}[\{d_i\}, \{d_i^\dagger\}] ,$$

where $a_{k, \alpha}^\dagger$ ($a_{k, \alpha}$) is the creation (annihilator) operator. In this case also there could be a degeneration d_g when the entire system is coupled. As an example, in the central region, we can consider the non-interacting case where

$$H_{cen} = \epsilon \sum_{i=1, d_g; \sigma} d_{i, \sigma}^\dagger d_{i, \sigma} , \quad (2.17)$$

or with the electron-phonon interaction

$$H_{cent} = \epsilon n_d + \frac{U}{2} n_d (n_d - 1) + \lambda \omega_0 (b^\dagger + b) n_d + \frac{p_x^2}{2M} + \frac{1}{2} K x^2 + \omega_0 b^\dagger b \quad (2.18)$$

where $n_d = \sum_{i=1, d_g; \sigma} d_{i, \sigma}^\dagger d_{i, \sigma}$ is the electron number in the central region (molecule).

Table 2.1: EHT parameters of atomic orbitals (AO) basis sets for H, C, N, Si and Au (Slater-type).

Element	K_{EHT}	AO	E_{onsite}	ζ_1	c_1	ζ_2	c_2
H	1.75	1s	-13.600	1.3000	1.0	1.0	0.0
C	2.8	2s	-21.39592	2.00290	0.71927	0.00000	0.00000
		2p	-15.22713	1.63935	0.55108	3.48317	0.53135
		3d	-4.06791	0.86366	0.88307	0.0	0.0
N	2.3	2s	-27.12699	2.74251	1.0	1.0	0.0
		2p	-17.52764	2.26145	1.0	1.0	0.0
		3d	-5.60857	0.62169	0.37978	1.0	0.0
Si	2.3	3s	-18.10264	1.83611	0.70366	1.0	0.0
		3p	-11.25298	0.78901	0.02770	1.70988	0.98313
		3d	-5.34706	0.68292	0.68383	1.72102	0.46957
Au	2.3	6s	-12.13418	2.31605	0.60326	1.0	0.0
		6p	-6.73967	1.74458	0.62661	1.0	0.0
		5d	-14.02565	2.32731	0.37598	5.44496	0.79437

2.6 Electron-phonon case

If we want to consider a generic Hamiltonian of a coupled system (contacts + tunneling couplings + molecule), it can be separated as: $H = H_C + H_t + H_{mol}$

$$\begin{aligned}
H = & \sum_{k,\alpha \in L/R} \epsilon_{k,\alpha} a_{\alpha,k}^\dagger a_{\alpha,k} \\
& + \sum_{\alpha \in L/R; k,\sigma,i=1,d_g} \left[t_{i,k,\alpha} \{\hat{x}\} a_{\alpha,k}^\dagger d_{i,\sigma} + H.c. \right] + H_{cen}[\{d_i\}, \{d_i^\dagger\}]
\end{aligned}$$

where the central region or molecule is defined, when electron-phonon interaction is considered, like,

$$H_{mol} = \epsilon n_d + \frac{U}{2} n_d (n_d - 1) + \lambda \omega_0 (b^\dagger + b) n_d + \frac{p_x^2}{2M} + \frac{1}{2} K x^2 + \omega_0 b^\dagger b,$$

where $n_d = \sum_\sigma d_\sigma^\dagger d_\sigma$, λ , is a coupling factor, ω is the fundamental frequency of the vibrational phonon, and U is the charge energy.

Electrons can be couple to two kinds of phonons: i) internal vibrational mode with frequency w_0 that couples to the electric field in the molecule and where phonons are created (annihilated) by operator $b(b^\dagger)$, ii) phonon mode that takes into account molecule oscillations when it is under a confinement potential, for instance, parabolic with parameter K . This mode does not couple directly to the charge but it depends on de displacement x in the tunneling amplitude terms $t_{i,k,\alpha}\{x\}$.

According to Koch *et al.* [10], we can assume an exponential decay of t with the distance between electrodes and the molecule. Considering that the distance between electrodes is $2d$ and the molecule length is $2l$, then:

$$t_{L,R}(x) = t_0 \exp(-(d - l \pm z)/x_0) ,$$

where x_0 is a parameter used to adjust the extension of wavefunctions out of the contacts and molecule.

In the high temperatures approximation developed by Mitra *et al.* [11], a coupling between vibrational phonon mode and one electron is considered. In this case it is possible to use a procedure to eliminate the coupling term using a canonical transformation in the Hamiltonian with the operator:

$$\hat{X} = \exp(-\lambda(\tilde{b}^\dagger - \tilde{b})) ,$$

where $\tilde{b} = b - \lambda \sum_{i,\sigma} d_\sigma^\dagger d_\sigma$. The operator transforms using the definition $S = \lambda(\sum_\sigma d_\sigma^\dagger d_\sigma)(b^\dagger - b)$ so $O \rightarrow e^S O e^{-S}$ and the Hamiltonian can be rewritten as $H' = H'_{mol} + H_c + H'_t$ and:

$$H'_{mol} = \epsilon' n_d + \frac{\tilde{U}}{2} n_d (n_d - 1) + \omega_0 \tilde{b}^\dagger \tilde{b} ,$$

where $\epsilon' = \epsilon - \lambda^2 \omega_0$ (energy shift due to the addition of an electron into the molecule),

$$H'_t = \sum_{\alpha \in L/R; k, \sigma, i=1, d_g} \left[t_{i,k,\alpha}\{\hat{x}\} \hat{X} a_{\alpha,k}^\dagger d_{i,\sigma} + H.c. \right] .$$

Now, we can find an expression to determine the reduced density matrix variation in the molecule ρ_{mol} when it is coupled to the contacts and if initially the contacts are supposed to be uncoupled to the molecule, $\rho = \rho_D \otimes \rho_{leads}$. The expression of

the density matrix variation ρ_{mol} allows to find a set of coupled equations for the occupation probabilities in the molecule defining:

$$P_m^n = \langle n, m | \rho_D | n, m \rangle$$

as the probability to have a state with n electrons and m phonons, and the equations can be written as:

$$\begin{aligned} \dot{P}_q^n &= \sum_{a,q'} f_a((q - q')\omega_0 + U(n - 1))\Gamma_{q,q'}^a P_{q'}^{n-1} \\ &+ [1 - f_a((q' - q)\omega_0 + Un)\Gamma_{q,q'}^a P_{q'}^{n+1}] \\ &- [1 - f_a((q - q')\omega_0 + U(n - 1))\Gamma_{q',q}^a P_q^n] \\ &- f_a((q' - q)\omega_0 + Un)\Gamma_{q',q}^a P_q^n, \end{aligned}$$

where $f_a(x) \equiv f(x + \epsilon' - \mu_a)$ and μ_a is the chemical potential of contact a . The variation for going from a state with n electrons and q phonons in the molecule to a state with $n - 1$ electrons and q' phonons is $R_{q \rightarrow q'}^{n \rightarrow n-1} = \sum_{a=L/R} f_a((q - q')\omega_0 + U(n - 1))\Gamma_{q,q'}^a$ where $\Gamma_{q,q'}^a$ is the transition rate to transfer an electron from the molecule to the contact a changing the phonon state from q to q' , equivalent to the transition rate of an electron from contact a to the molecule changing the phonon state from q to q' and then

$$\Gamma_{q',q}^a = \Gamma_a |\langle q' | X | q \rangle|^2.$$

These terms are calculated according to the method given by Mahan (ref.), where the absolute value ($|\langle q' | X | q \rangle|^2 \equiv X_{q,q'}^2$) is given by:

$$X_{q < q'}^2 = \left| \sum_{k=0,q} \frac{(-\lambda^2)^k (q!q')^{1/2} \lambda^{|q-q'|} e^{-\lambda^2/2}}{k!(q-k)!(k+|q'-q|)!} \right|^2$$

which is symmetric under the change q to q' .

To obtain the current through the system, Mitra *et al.* used the following expression for the current through the contact a as a function of probabilities

$$\begin{aligned} I_a &= \sum_{n,q,q'} (2d_g - n) P_q^n f_a((q' - q)\omega + Un)\Gamma_{q,q'}^a \\ &- (n + 1) P_q^{n+1} [1 - f_a((q - q')\omega + Un)] \Gamma_{q',q}^a \end{aligned} \tag{2.19}$$

2.7 Semiclassical approximation (WKB)

Considering the Schrodinger equation

$$\sum_a \frac{\hbar}{2m_a} \Delta_a \psi + (E - V)\psi = 0 . \quad (2.20)$$

If the wavefunction is approximated by $\psi = e^{(i/\hbar)\sigma}$, the equation can be written as

$$\sum_a \frac{1}{2m_a} (\nabla_a \sigma)^2 - \sum_a \frac{i\hbar}{2m_a} \Delta_a \sigma = E - V \quad (2.21)$$

and expanding the term σ into a series in powers of \hbar ; $\sigma = \sigma_0 + (\hbar/i)\sigma_1 + (\hbar/i)^2\sigma_2 + \dots$

and taking the one dimensional case for a single particle, the equation reduces to

$$\sigma'^2/2m - i\hbar\sigma''/2m = E - V(x) , \quad \text{where } \sigma' = d\sigma/dx \quad \text{and} \quad \sigma'' = d^2\sigma/dx^2 . \quad (2.22)$$

If we now consider only the first approximation $\sigma = \sigma_0$ and neglect the second term, the equation is $\sigma_0'^2/2m = E - V(x)$ with the solution

$$\sigma_0 = \pm \int \sqrt{2m(E - V(x))} dx . \quad (2.23)$$

The integrand can be recognized as the classical momentum $p(x) = \sqrt{2m(E - V)}$ of the particle. The term neglected is small when $\hbar|\sigma''/\sigma'^2| \ll 1$. If we consider $\sigma' = p$, then $|d(\lambda/2\pi)/dx| \ll 1$, which means that the wavelength of the particle has small changes with the distance x . In other words, the approximation is not applicable when the momentum is small, i.e, when $E = V(x)$.

Now, the second term in the expanded series in \hbar is evaluated from the reduced Schrödinger equation, leading to

$$\sigma_0'\sigma_1' + \frac{1}{2}\sigma_0'' = 0 .$$

It follows that $\sigma_1' = -\sigma_0''/2\sigma_0' = -p'/2p$, which upon the integration gives $\sigma_1 = -\frac{1}{2} \log p$. Replacing this expression in the expanded series and in the wavefunction one gets

$$\psi = C_1 p^{-1/2} e^{(i/\hbar) \int p dx} + C_2 p^{-1/2} e^{-(i/\hbar) \int p dx} .$$

2.8 Potential I

In order to consider oscillations of the molecules there are some potential that were previously reported [12,13]. The Figure 2.4 shows the potential that we are considering as an external confining potential that we want to use. Using the semiclassical (WKB) approximation, the eigenfunctions have been obtained considering five regions separated by the limits where the energy E is equal to the potential $V(x)$.

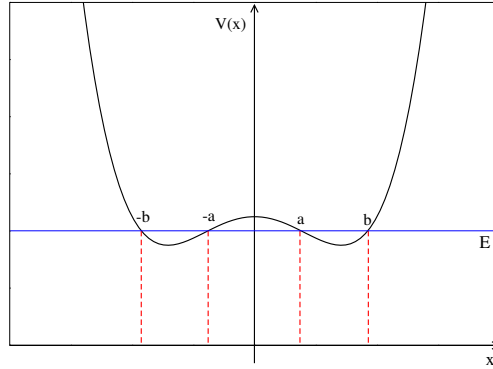


Figure 2.4: Symmetrical potential $V(x) = x^4 - x^2 + h$.

For this case, the WKB solutions are:

- $x < -b$

$$\psi_I = \frac{c}{\sqrt{|p|}} \exp\left(-\frac{1}{\hbar} \int_x^{-b} |p| dx\right), \quad (2.24)$$

- $-b < x < -a$

$$\psi_{II} = \frac{c}{\sqrt{p}} \exp\left(-i\frac{\pi}{4} + \frac{i}{\hbar} \int_{-b}^{-a} p dx - \frac{i}{\hbar} \int_x^{-a} p dx\right) + \frac{c}{\sqrt{p}} \exp\left(i\frac{\pi}{4} - \frac{i}{\hbar} \int_{-b}^{-a} p dx + \frac{i}{\hbar} \int_x^{-a} p dx\right),$$

- $-a < x < a$

$$\begin{aligned} \psi_{III} = & \frac{c}{\sqrt{p}} \sin\left(\frac{1}{\hbar} \int_{-b}^{-a} p dx\right) \exp\left(-\frac{1}{\hbar} \int_{-a}^a |p| dx + \frac{1}{\hbar} \int_x^a |p| dx\right) \\ & + \frac{2c}{\sqrt{|p|}} \cos\left(\frac{1}{\hbar} \int_{-b}^{-a} p dx\right) \exp\left(\frac{1}{\hbar} \int_{-a}^a |p| dx - \frac{1}{\hbar} \int_x^a |p| dx\right) \end{aligned} \quad (2.25)$$

- $a < x < b$

$$\begin{aligned}
\psi_{IV} = & \frac{c}{2\sqrt{p}} \sin\left(\frac{1}{\hbar} \int_{-b}^{-a} p dx\right) \exp\left(-\frac{1}{\hbar} \int_{-a}^a |p| dx - i\frac{\pi}{4}\right) \exp\left(-\frac{i}{\hbar} \int_a^b p dx + \frac{i}{\hbar} \int_x^b p dx\right) \\
& + \frac{2c}{\sqrt{p}} \cos\left(\frac{1}{\hbar} \int_{-a}^a p dx\right) \exp\left(\frac{1}{\hbar} \int_{-a}^a |p| dx + i\frac{\pi}{4}\right) \exp\left(-\frac{i}{\hbar} \int_a^b p dx + \frac{i}{\hbar} \int_x^b p dx\right) \\
& \frac{c}{2\sqrt{p}} \sin\left(\frac{1}{\hbar} \int_{-b}^{-a} p dx\right) \exp\left(-\frac{1}{\hbar} \int_{-a}^a |p| dx + i\frac{\pi}{4}\right) \exp\left(\frac{i}{\hbar} \int_a^b p dx - \frac{i}{\hbar} \int_x^b p dx\right) \\
& + \frac{2c}{\sqrt{p}} \cos\left(\frac{1}{\hbar} \int_{-a}^a p dx\right) \exp\left(\frac{1}{\hbar} \int_{-a}^a |p| dx - i\frac{\pi}{4}\right) \exp\left(\frac{i}{\hbar} \int_a^b p dx - \frac{i}{\hbar} \int_x^b p dx\right)
\end{aligned} \tag{2.26}$$

- $x > b$

$$\begin{aligned}
\psi_V = & \frac{c}{2\sqrt{p}} \sin\left(\frac{1}{\hbar} \int_a^b p dx\right) \cos\left(\frac{1}{\hbar} \int_a^b p dx\right) \exp\left(-\frac{1}{\hbar} \int_{-a}^a |p| dx\right) \exp\left(-\frac{1}{\hbar} \int_b^x |p| dx\right) \\
& + \frac{2c}{\sqrt{p}} \cos\left(\frac{1}{\hbar} \int_a^b p dx\right) \sin\left(\frac{1}{\hbar} \int_a^b p dx\right) \exp\left(\frac{1}{\hbar} \int_{-a}^a |p| dx\right) \exp\left(-\frac{1}{\hbar} \int_b^x |p| dx\right)
\end{aligned} \tag{2.27}$$

where $p = \sqrt{2m(E - V(x))}$ and c is a parameter that is defined according to the conditions in each interval. We have also considered a generalized potential form $V(x) = v_a x^4 - v_b x^2 + E_0$ and we have parameters of energy (E, E_0) , mass m , potential (v_a, V_b) and positions that can be associated and fixed with each particular case.

2.8.1 Density Matrix

One of the common assumptions about nanoelectronic devices, is that electronic reservoirs are in equilibrium at a certain chemical potential. To implement the dynamic variation of the density inside the system, we can define the projected matrix density ρ_s

$$\rho_s = Tr_c\{\rho(t)\} \otimes \rho_{leads}$$

where ρ_C is the density matrix of the contact (left or right), that is at equilibrium at some chemical potential (μ_L or μ_R). For the molecule, its density matrix (reduced with respect to the total density) is:

$$\rho_{cen} = Tr_c \rho_s .$$

If we also define a complementary density matrix ρ_t , so $\rho_t = \rho - \rho_s$ and considering $Tr_C \rho_t = 0$, it is possible to express some properties in terms of ρ_{cen} . Using these definitions, an expression for the density matrix variation can be written as:

$$\frac{d\rho_{cen,I}(t)}{dt} = -Tr_c \int_{-\infty}^{\infty} dt' [H_{tI}(t), K_I(t, t') [H_{tI}(t'), \rho_{sI}(t')]] .$$

This expression corresponds to a generalization of the master equation. For this case, the description of operators is used in the interaction representation and then, stationary conditions can be rewritten as:

$$0 = \sum_j P^j R_{j \rightarrow i} \quad \text{where} \quad P^j = \langle j | \rho_{cen} | j \rangle$$

and $R_{j \rightarrow i}$ terms are in-scattering and out-scattering rates. Conservation of the probability assumes that $\sum_i R_{j \rightarrow i} = 0$ and provides the condition

$$0 = \sum_{j \neq i} P^j R_{j \rightarrow i} - P^i \sum_{i \neq j} R_{i \rightarrow j} ,$$

so it is possible to calculate the current coming from a contact α to the molecule using the density of the system ($\langle I_\alpha(t) \rangle = Tr \hat{\rho}(t) \hat{I}_\alpha$) obtaining

$$\langle I \rangle = -i Tr \int_{-\infty}^{\infty} dt' [I_I(t) K_I(t, t'), H_{tI}(t')] \rho_{cen,I}(t') \otimes \rho_c ,$$

where the current operator, used to calculate the current from contact α to the molecule, is expressed as a function of the variation of occupation number operator for the contact α :

$$I_\alpha = -e \dot{N}_\alpha = -\frac{ie}{\hbar} [H, N_\alpha] .$$

We can also obtain the current (a physical observable) considering the expected value of current operator, for example current coming from the left contact ($\alpha = L$):

$$\begin{aligned} \langle I_L \rangle = J_L(t) = & -\frac{2e}{\hbar} \int_{-\infty}^t dt_1 \int \frac{d\epsilon}{2\pi} Im Tr \left(e^{-i\epsilon(t_1-t)} \mathbf{\Gamma}^L(\epsilon, t_1, t) \right) \\ & \times [\mathbf{G}^<(t, t_1) + f_L^0(\epsilon) \mathbf{G}^r(t, t_1)] , \end{aligned} \quad (2.28)$$

where $\mathbf{\Gamma}$ and \mathbf{G} are matrices and $f_L^0(\epsilon)$ is the distribution function for the contact.

Each one of these Γ_{mn} terms is a coupling term between the region and the contacts.

Besides, an analogous formula can be obtained for $J_R(t)$.

This important equation, allows to calculate the current in terms of local quantities (Green's functions of the central region).

Bibliography

- [1] H. Haug and A. P. Jauho. *Quantum Kinetics in Transport and Optics of Semiconductors*. Springer–Verlag, 1996.
- [2] S. Datta, W. Tian, S. Hong, R. Reifenberger, J. I. Henderson, and C. P. Kubiak. Current–voltage characteristics of self–assembled monolayers by scanning tunneling microscopy. *Phys. Rev. B*, 79:2530, 1997.
- [3] G. D. Mahan. *Many particle physics, 2nd ed.* Plenum Press, 1990.
- [4] A. Jauho, N. S. Wingreen, and Y. Meir. Time-dependent transport in interacting and non-interacting resonant-tunneling systems. *Phys. Rev. B*, 50:5528, 1994.
- [5] R. Lake and S. Datta. Non-equilibrium Green function method applied to double barrier resonant-tunneling diodes. *Phys. Rev. B*, 45:6670, 1992.
- [6] R. Lake, G. Klimeck, R. C. Bowen, and D. Jovanovic. Single and multi-band modeling of quantum electron transport through layered semiconductor devices. *J. Appl. Phys.*, 81:7845, 1997.
- [7] S. Datta. *Quantum transport. Atom to transistor*. Cambridge University Press, 2005.
- [8] A. R. Williams, P. J. Feibelman, and N. D. Lang. Green’s–function methods for electronic–structure calculations. *Phys. Rev. B*, 26:5433, 1982.
- [9] W. Tian, S. Datta, S. Hong, R. Reifenberger, J. I. Henderson, and C. P. Kubiak. Conductance spectra of molecular wires. *J. Chem. Phys.*, 109:2874, 1998.

-
- [10] J. Koch, F. von Oppen, Y. Oreg, and E. Sela. Thermopower of single-molecule devices. *Phys. Rev. B*, 70:1951107, 2004.
- [11] A. Mitra, I. Aleiner, and A. J Millis. Phonon effects in molecular transistors: Quantal and classical treatment. *Phys. Rev. B*, 69:245302, 2004.
- [12] A. Donarini, M. Grifoni, and K. Richter. Dynamical symmetry breaking in transport through molecules. *Phys. Rev. Lett.*, 97:166801, 2006.
- [13] C. A. Balseiro, P. S. Cornaglia, and D. R. Grempel. Electron-phonon correlation effects in molecular transistors. *Phys. Rev. B*, 74:235409, 2006.

Chapter 3

Silicon cluster on semiconductor surfaces

3.1 Introduction

In the last years, a set of experiments have tried to understand the effect of molecules supported by semiconducting surfaces. In this setup, a STM probe is used as a second electrode and the applied potential controls the electronic transport. The use of surfaces with band gaps and active electronic states could provide the ingredients for new phenomena that are not observed in the case of metallic surfaces. Therefore, the STM equipment is not only used to obtain images at an atomic scale [1], but also to get local electronic properties of surfaces and molecules.

Similarly to surfaces, clusters have been also characterized theoretically and experimentally. For example, Belomoin *et al.* have reported the dependence of the optical response of silicon cluster with different terminations (C, N, H) and as a function of size (1-3 nm). They have discussed the application of these clusters in biological imaging due to the light emission of these particles [2]. Usually clusters are different from the bulk-like structure mainly because of surface effects such as reconstruction (surface- volume ratio becomes an important control parameter). On the other hand, from the transport properties point of view, linking electrodes through macromolecules such as metallic nanocrystals or organic molecules have provided a diode-like behavior originating in their dependence of the tunneling con-

ductance [3, 4]. These results support the idea of developing nanoelectronic devices by using silicon clusters as active structures. Along this research line, the deposition of small silicon clusters on silicon surfaces has been reported by Watanabe *et al.* [5]. Scanning tunneling spectroscopy (STS) measurements were performed on these samples and they were able to show resonant tunneling on those devices, due to electronic states of the cluster [6].

In this chapter, we are going to present and discuss transport properties associated to molecular levels and the electronic states associated to the molecule-surface interaction. We start by identifying the properties of every part of the system without interactions with the rest of components. As a first case, we present surfaces usually employed as substrates in experiments. Silicon and gold surfaces with different orientations are considered in order to differentiate surface effects when a molecule is supported by them. After that, isolated clusters are studied using several theory levels in order to check the accuracy of our results. Once the isolated components are studied, the coupled system is considered focusing our attention on determining the way in which the molecule changes its electronic properties, such as density of states (DOS), and testing the influence of different surfaces like Si[111] and Au[111]. Electronic properties are evaluated at equilibrium, and afterwards, a STM probe is included in the system to simulate the spectroscopic calculations following the idea of Tersoff *et al.* [7], who has not just obtained atomic scale images, but also studied conductivity of molecules. To consider non-equilibrium conditions, both surface and metallic electrodes respectively, are kept at local equilibrium adjusting the chemical potentials μ_1 and μ_2 . The self-consistent calculation that we perform for the potential and the electronic density assures the evaluation not only of the current, but also of the conductance and charge transfer between the molecule and the substrate and/or the metallic electrode.

3.2 Surfaces

The interest of this work is to study non-metallic surfaces like the first one showed in Fig. 3.1-a, which is a semiconductor silicon with orientation [111] and without

reconstruction [8]. In this case, the presence of dangling bonds on the surface is associated with non broad energy levels observed in band structure of fig. 3.1-b. This band structure has been calculated using 24 layers (7 nm of depth) and is in good agreement with the theoretical results of Ivanov *et al.* [9] that used an empirical tight binding method. Reconstructed and passivated surfaces are mainly observed in experiments [5,6], but it is also possible to work with ideal surfaces in order to better understand its electronic properties that are important for the mechanism of reconstruction.

3.2.1 Si[111] surface

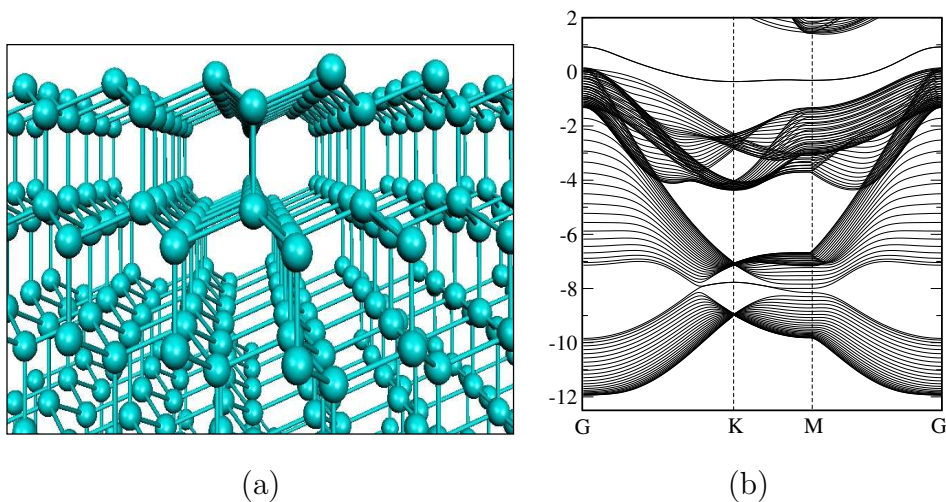


Figure 3.1: (a) Lateral view of Si[111] surface without reconstruction. (b) The calculated band structure.

Absorption of silicon clusters has been both theoretically [10] and experimentally reported [5,11].

Figure 3.1 shows the first case using an ideal silicon surface with [111] orientation. In general, surfaces are reconstructed to minimize its energy, however it is possible to experimentally produced unreconstructed surfaces and the study of their electronic properties are important to understand the reconstruction processes. The system possesses a diamond-like structure with a lattice parameter $a = 5.43$ ang. Besides this, band structure has been calculated from geometric considerations and follow-

ing a hexagonal path of k points. Considering a larger number of layers, a better resolution of allowed energy levels can be achieved. Therefore we have considered surfaces with a depth of 24 layers from the surface (7 nm approx.). Also, for the tight binding model, the interaction between layers is considered until third neighbors. The Fermi energy for silicon has been established between the gap given by the ionization energy and the electronic affinity. The chemical potential has been then fixed at -4.8 eV. From these results, we have obtained an associated indirect gap of 1.2 eV.

3.2.2 Si[111] surface saturated with H atoms

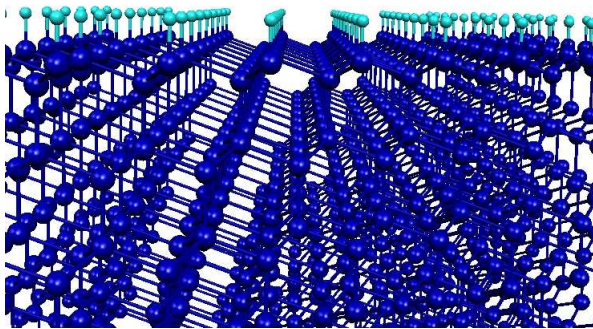


Figure 3.2: Configuration and band structure for Si[111] surface terminated with H according to the theoretical and experimental results [12]. The Si-H distance is 1.5 angsts.

In order to avoid a possible reconstruction of surface we can consider the inclusion of atoms to saturate the system. In particular, the inclusion of Hydrogen atoms on the surface changes the electronic and optical properties [13]. We can see that there are some new states associated with the new Hydrogen layer, which saturate the dangling bonds on the ideal surface (in this [111] direction there is one dangling bond per unit cell).

The new states created by the silicon-hydrogen interaction promote a change in the initial energy gap considered for the ideal case.

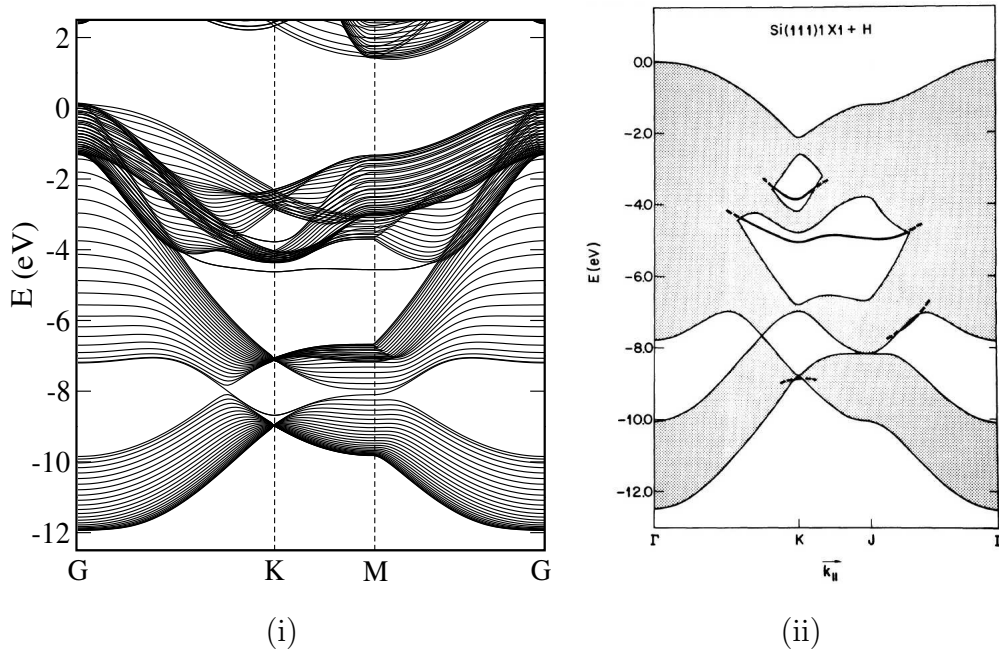


Figure 3.3: Band Structure for Si[111]-H. (i) Calculated result, (ii) Reported result: Pandey, Phys. Rev. B 14, 1557 (1976).

3.2.3 Si[100] surface

For this surface, we have considered an orientation [100] from the bulk. In this direction, there are two dangling bonds per unit cell on the ideal surface. Figure 3.4 shows a lateral view of the surface where the number of layers considered are

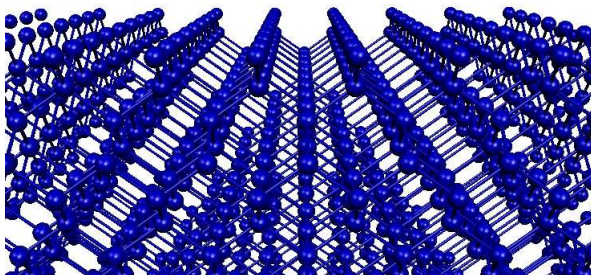


Figure 3.4: Si[100] without reconstruction.

32 that corresponds to 16 cells of depthness. The importance of the number of layers is related to the accuracy that we want to consider to evaluate the electronic properties.

The Figure 3.5 shows the comparison between the calculated band structure using

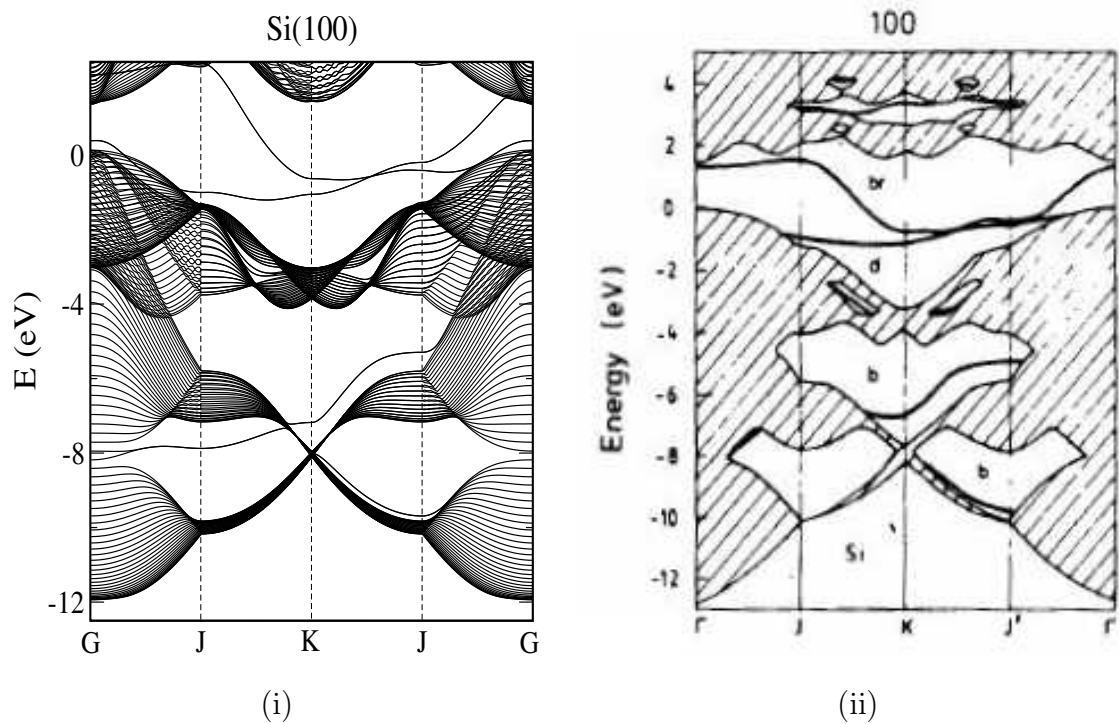


Figure 3.5: Band structure: (i)calculated result, (ii) from a tight-binding model reported by Ivanov *et al.* [9]

the EHT approach and the previously reported result by Ivanov *et al.*, where a tight-binding model was considered to describe the Hamiltonian of the system.

As for the Si[111] surface, we have considered the hydrogenate surface Si[100] where the distance between silicon atoms on the surface and the hydrogens is fixed at 1.35 angstroms. Again we have calculated the band structure associated with the surface and compared with the results previously reported.

3.2.4 Si[100] surface saturated with H atoms.

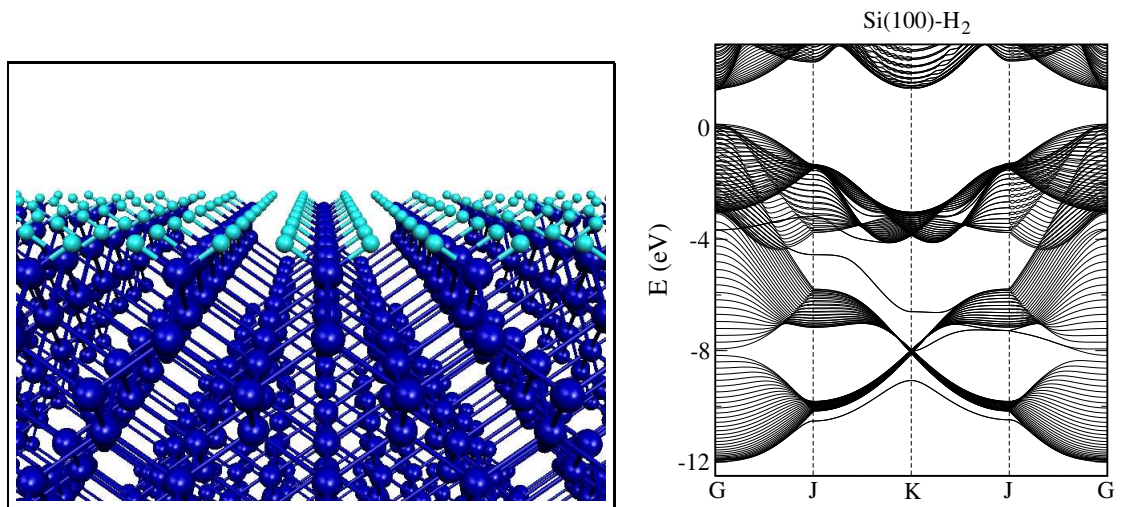


Figure 3.6: Band structure calculated. Distance Si-H: 1.35 angstroms.

3.3 Atomic clusters

The study of charge transport in molecules has important applications in electronics. In particular, silicon clusters have shown interesting optical and electronic properties according to the size, structure and terminations [2, 14]. These clusters possess properties that could be sensitive to the size and geometry

The model considered to define the Hamiltonian is based on the EHT. Parameters for this model were established after a comparison of electronic structure of EHT with other theoretical levels (as given by LDA and GGA). In order to estimate the effect of the clusters on the surface, we have considered two kind of molecules: an inorganic molecule $\text{Si}_{29}\text{H}_{24}$ and an organic molecule that in this case corresponds to the Styrene which has been previously studied [15].

3.3.1 $\text{Si}_{29}\text{H}_{24}$ cluster

As a first stage, a structural optimization has been performed by using the computational software Gaussian 98 and following a local density approximation (LDA) where the correlation functional VWN is combined with the exchange term of Slater with the basis set 6-311G.

Optimized geometry:

Si-H : 1.501 ang.

Si-Si: 2.320 ang. (external rings)

Si-Si: 2.384 ang. (core)

For the optimized geometry, electronic structure of the cluster was calculated with different approximations. Besides the EHT model parameterized for silicon and hydrogen, we have also used LDA and GGA approximations. Energy levels obtained are listed in the next table:

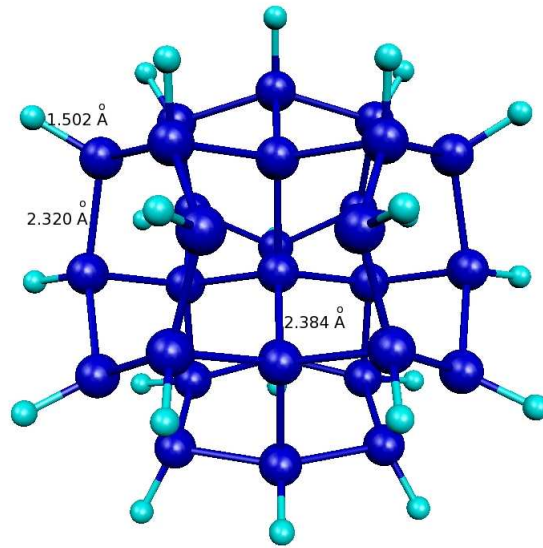


Figure 3.7: Silicon cluster $Si_{29}H_{24}$. Optimization has been obtained from a LDA approximation and using a Gaussian basis set.

Level	EHT (deg.)	LDA (deg.)	B3LYP/6-311G (deg.)
LUMO+2	-3.255(3)	-2.406(1)	-1.254(1)
LUMO+1	-3.463(3)	-2.488(3)	-1.303(3)
LUMO	-4.428(3)	-3.407(3)	-2.297(3)
HOMO	-7.512(3)	-6.417(3)	-6.529 (3)
HOMO-1	-7.617(2)	-6.421(2)	-6.547(2)
HOMO-2	-7.755(3)	-6.423(3)	-6.585(3)
Gap (EHT): 3.08 eV		Gap(LDA): 3.01 eV	Gap(CGA): 4.2 eV

According to Belomoin *et al.* (Appl. Phys. Lett., Vol. 80, 841-843), the gap (difference between HOMO and LUMO levels) for silicon clusters is 3.5 and 2.67 eV for 1.0 nm ($Si_{29}H_{24}$) and 1.6 nm ($Si_{123}H_{xx}$)

Previously, Allan *et al.* found that silicon clusters with diameters of 1.03 nm and 1.67 nm were stable with gaps of 3.4 and 2.63 eV.

As we can see, the distribution of states is similar in all energy levels except for the highest unoccupied levels.

3.3.2 Molecular Orbitals and charge density

In order to study the reactivity of a molecule and the electronic configuration of the molecule, we can consider molecular orbitals around the HOMO level. Within this approach, another possibility is to calculate the charge density associated with states which are close to the HOMO level.

In order to compare charge densities between EHT and LDA, we calculated the

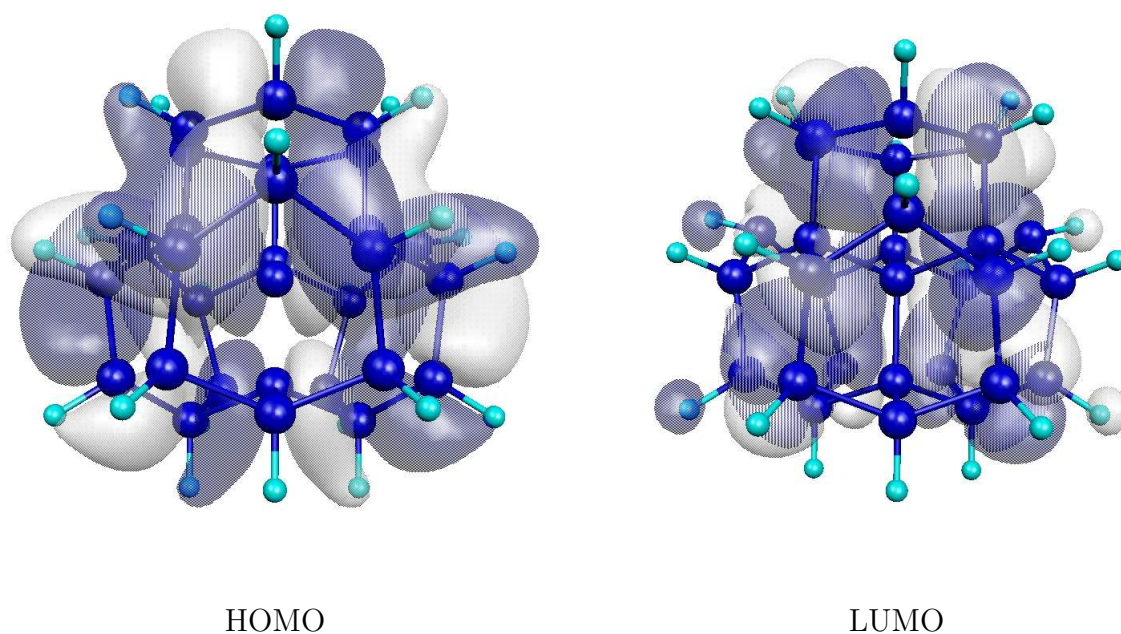


Figure 3.8: Molecular orbitals calculated using a LDA approximation [16].

charge density for the highest occupied molecular orbital (with triple degeneracy), as depicted in Figure 3.9 (the charge isosurfaces have the same cutoff). By using the LDA approximation when can compare in a qualitative way the description of the molecular levels with another model (EHT for example), specially if we are referring to non excited states, because this theory is inprinciple defined to study the ground state of the system.

The next case (fig. 3.10) corresponds to the evaluation of the total charge density in all occupied states from the HOMO level until 3 eV below the Fermi level (35 states).

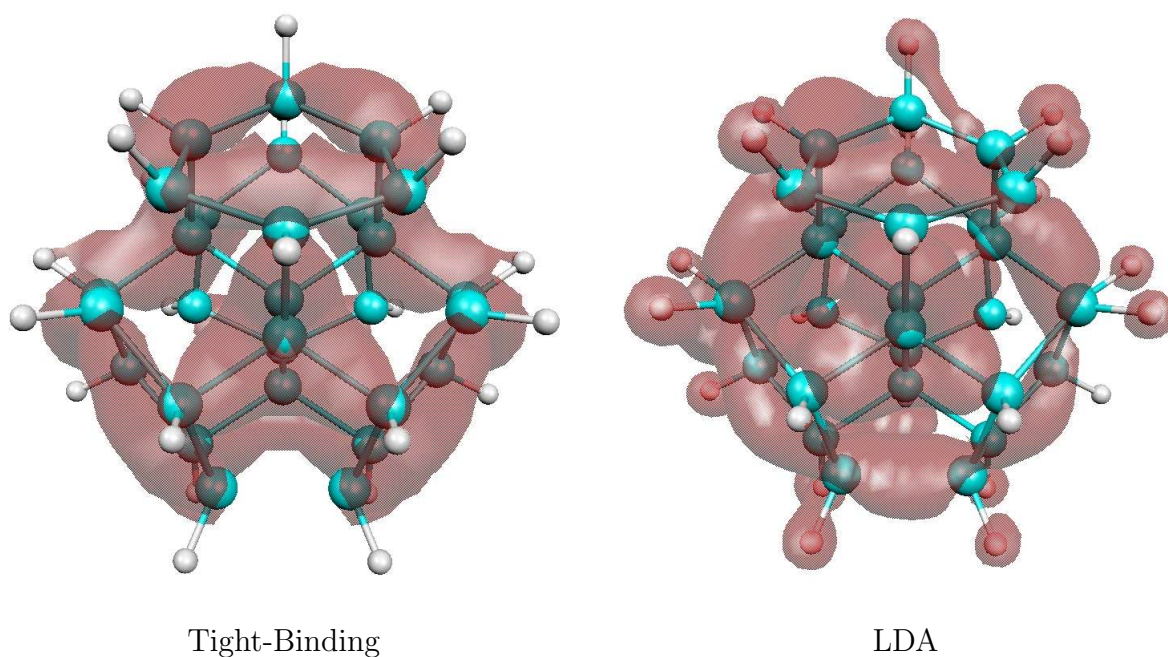


Figure 3.9: Charge density of HOMO level with tight binding and LDA models.

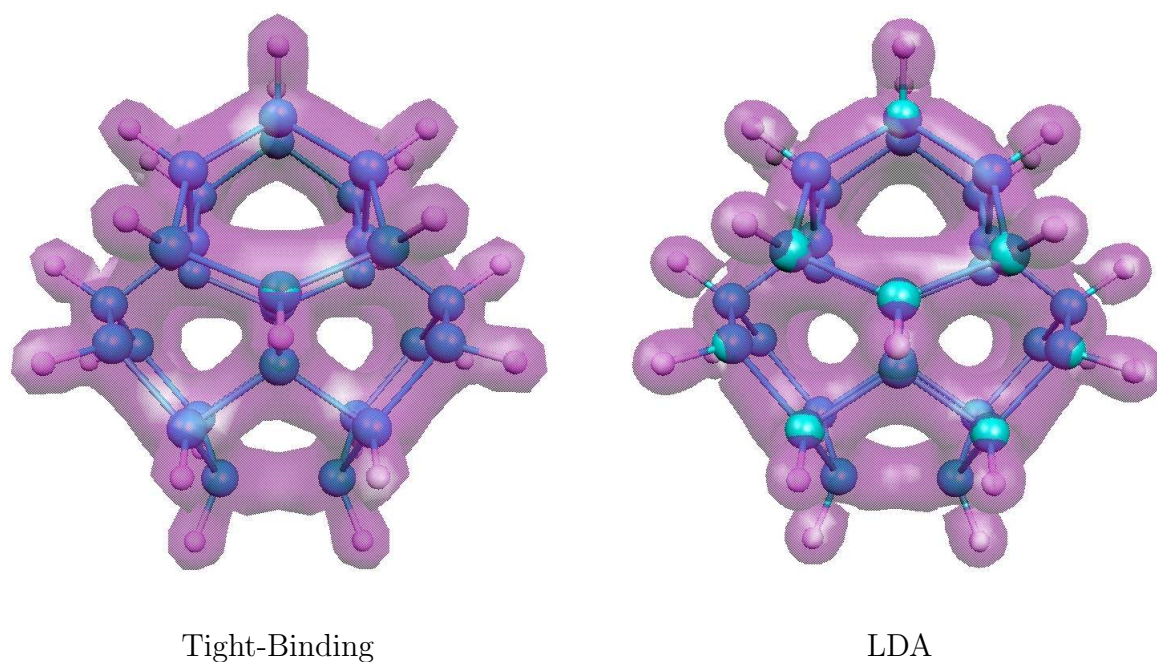


Figure 3.10: Charge density considering occupied states from HOMO level until 3 eV below the Fermi level.

Besides the original geometric configuration, we have obtained another stable structure for the silicon cluster $Si_{29}H_{24}$ interacting with the Si[111] surface following a molecular dynamic simulation with a tight binding model.

Next, we have optimized the second configuration by using a LDA method provided

by the computational software CPMD. The energy levels associated with the mod-

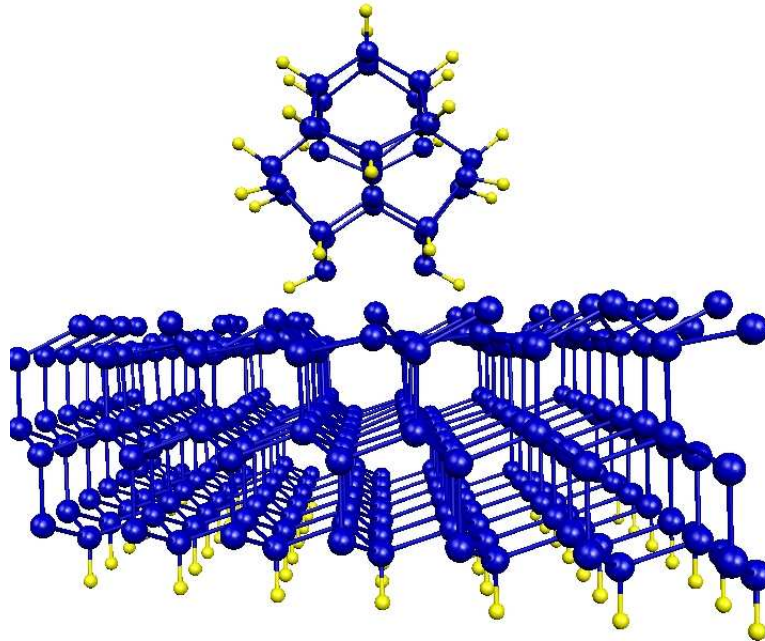


Figure 3.11: Second configuration for the cluster interacting with the Si[111] surface.

ified cluster are given by the following table:

Level	EHT (deg.)	LDA (deg.)
LUMO+2	-4.16(1)	-3.235(1)
LUMO+1	-4.405(1)	-3.402(1)
LUMO	-6.032(1)	-5.06(1)
HOMO	-6.871(1)	-5.914(1)
HOMO-1	-7.5(1)	-6.421(2)
HOMO-2	-7.56(1)	-6.438(1)

The new associated gap corresponds to 0.839 eV with the EHT model and to 0.854 eV with the LDA approach (considering free cluster calculations). In this configuration, there is no degeneracy at HOMO and LUMO levels, so we can compare directly the eigenstates (fig. 3.12).

As we have proceeded before for the first cluster, the total charge density (24 states

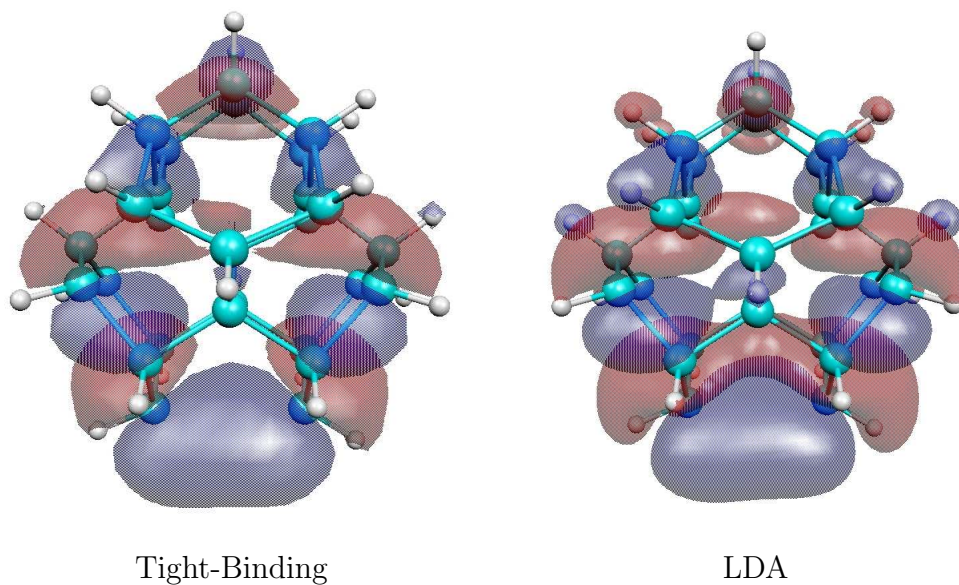


Figure 3.12: HOMO with a tight binding model and a LDA theory (there is no degeneracy at this level).

from HOMO until 3 eV below Fermi level) is shown in fig. 3.13:

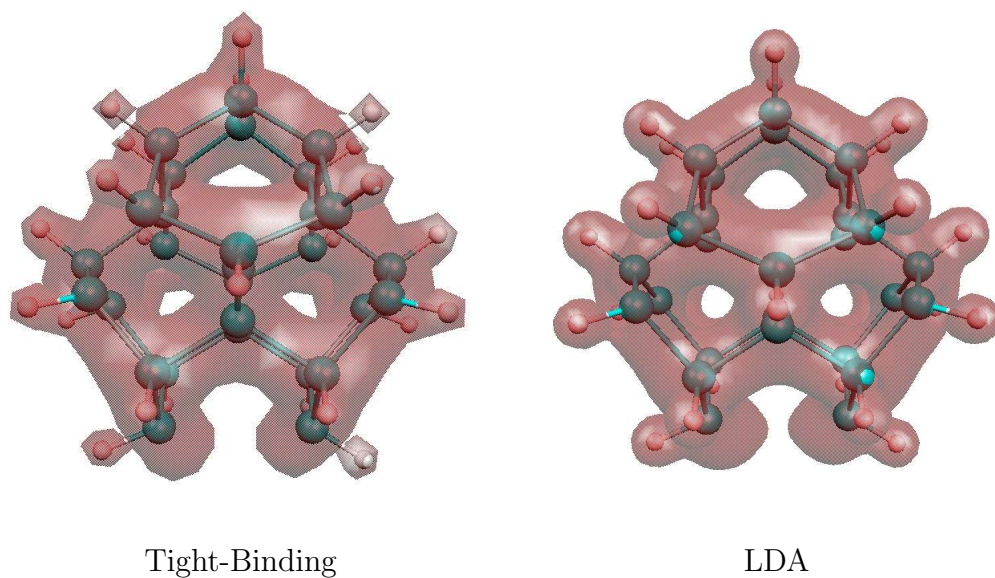


Figure 3.13: Charge density considering occupied states from HOMO until 3 eV below the Fermi level.

3.4 Cluster-surface interaction

We can find in the literature that the inclusion of organic molecules [3] and metallic nanocrystals [4] between two electrodes present a diode-like behavior or changes the tunneling conductance.

In this work, we want to study inclusion effects of silicon clusters on the several surfaces.

We have tested different parameterizations for extended Huckel theory (EHT) in several clusters Si_nH_m . Also we have included results obtained by first principles at several levels (LDA, CGA). The best match between EHT and DFT corresponds to the LDA case.

The next step is to examine the DOS of the cluster in contact with the surface. We have considered three different cases: Au[111], Si[111] and [Si100].

The Figure 3.14 shows the behavior of the DOS of $Si_{29}H_{24}$ as a function of the

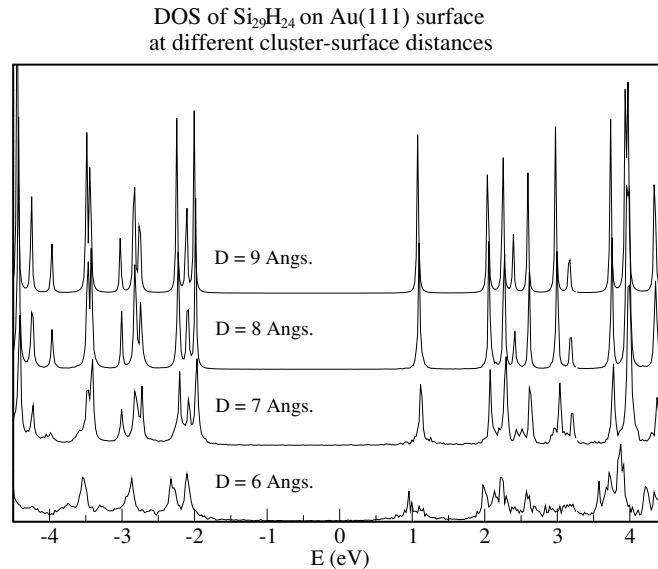


Figure 3.14: DOS of $Si_{29}H_{24}$ on Au[111]. Parameter D is the distance between surface and the center of mass of the cluster.

distance D between the cluster and the metallic surface Au[111]. At large D s, the energy levels seem similar to the energy levels of the free cluster. As soon as the D is diminished, the molecular levels are broadened due to the interaction between the molecule and the metallic Au[111].

The same procedure is applied to the molecule when it is deposited on the silicon surface Si[100]. We can see here the same broadening effect, considering also that there is a shift compared to the metallic surface that is due to the different assigned chemical potential (-5.26 eV for Au and -4.8 for Si).

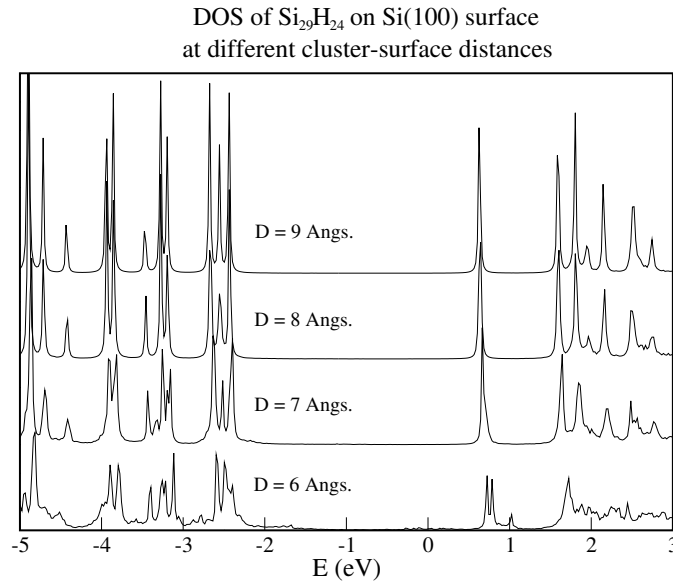


Figure 3.15: DOS of $Si_{29}H_{24}$ on Si[100]

For the free case, DOS of cluster has sharp energy levels. When the molecule is in contact with the surface (which has a continuous density of states), intensities are diminished and there is also a broadening of the states due to the interaction with surface states.

Now for the coupled system, Figure 3.16, shows electronic configurations of the bare components and the coupled case. The up figure corresponds to the discrete energy levels associated with the free cluster $Si_{29}H_{24}$. The middle figure is the e-DOS of a Si[111] surface where a energy gap of 0.4 eV is observed. This figure in good agreement with the reported by Pandey and Schlüter [17, 18], where calculations have been obtained using a semiempirical tight-binding method and a self-consistent pseudopotential respectively. The presence of dangling bonds is observed in these cases but at different positions compared with our results. When the molecule is on the surface (down figure), a shift and broadening of molecule levels is found and the appearance of a new peak around 0.7 eV above the Fermi level is obtained. There is

also a small projection of the energy states coming from the surface associated with dangling bonds around 0.5 and 1.0 eV below the Fermi level. In our calculations, we shift the energy levels according with the chemical potential of -4.8 eV previously reported for silicon surfaces [19].

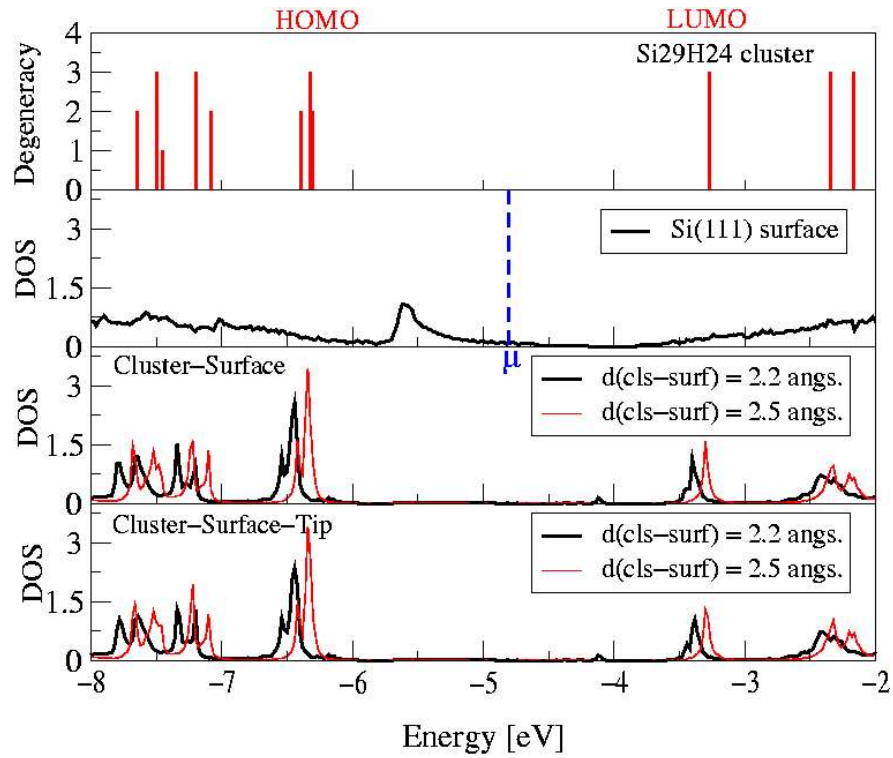


Figure 3.16: DOS of new $Si_{29}H_{24}$ cluster on Si[111] at $d = 2.2$ angstroms and $d = 2.5$ angstroms.

3.4.1 Displacement effect

Even considering the most suitable configuration of the molecule supported by the surface, it is interesting to see what happens when the molecule is translated to other positions on the surface. In order to consider this, we have evaluated the DOS of the cluster at different parallel positions to the surface (X-Y plane). In fig. 3.17a we can see the surface with the path followed in both directions (enhanced atoms are equivalent due to translational symmetry).

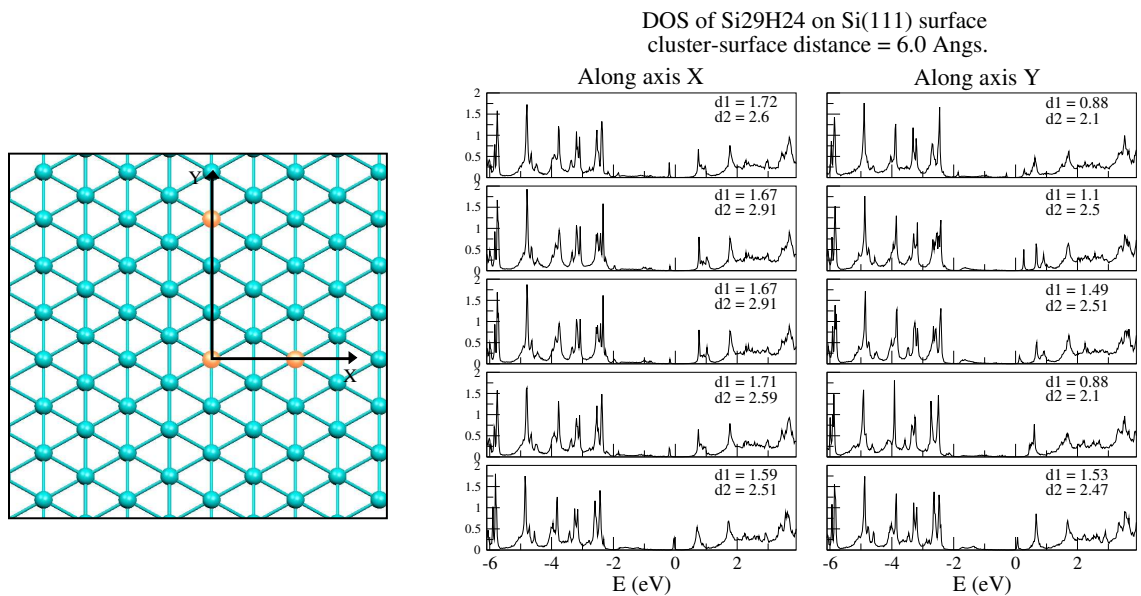


Figure 3.17: a) Displacement along the x and y axis, and b) DOS of $Si_{29}H_{24}$ on Si[111] for $D = 6$ angstroms. (surface-center mass distance)

Energy levels have been adjusted to set the Fermi level at the origin. We can see that the new peak obtained is found at several cases. The next figure 3.18 shows the variations of the DOS at a cluster surface distance $D = 6.5$ angstroms.

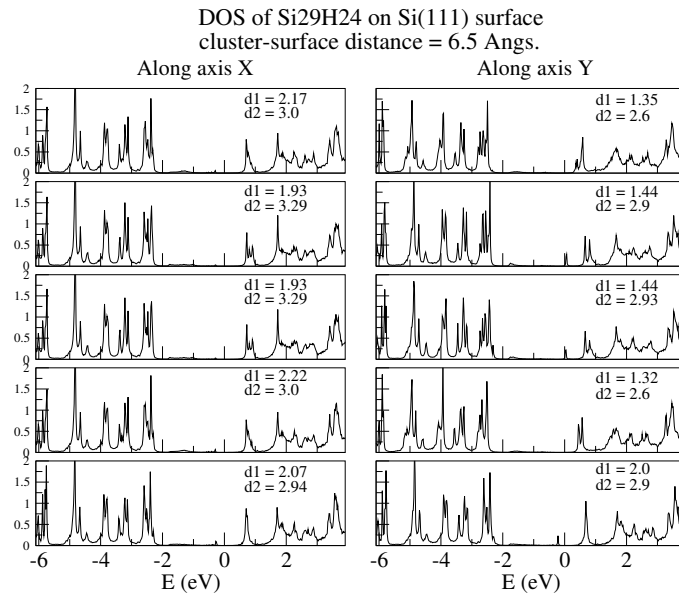


Figure 3.18: DOS of $Si_{29}H_{24}$ on Si[111] at $D = 6.5$ angstroms and displacements along x and y axis.

3.4.2 Modified cluster on Si[111]

As we have seen in section 3.3.2, there is also another possible configuration for the silicon like the one depicted in fig. 3.11 For the modified structure, we can calculate the DOS in a same way that for the original case. In the figure 3.19 we can see the DOS of the modified cluster where there are new states coming from the surface between -2 eV and -1 eV.

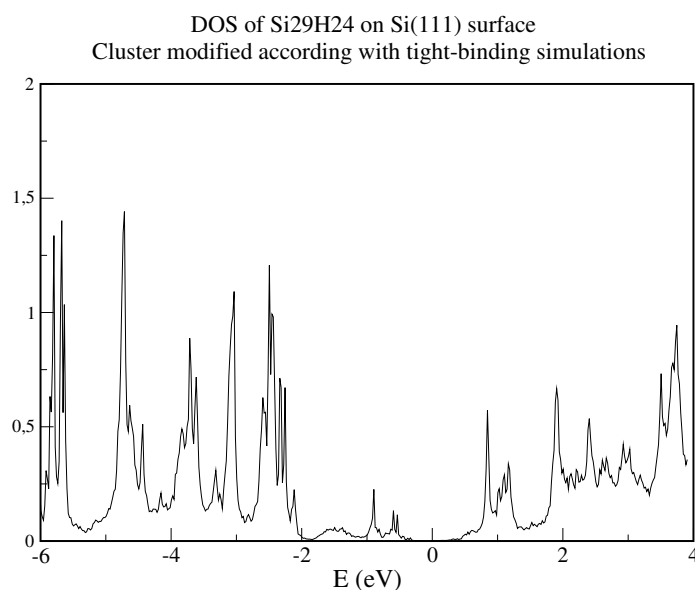


Figure 3.19: DOS of modified Si₂₉H₂₄ cluster on Si[111] at $D = 6.0$ angstroms and displacement along the x and y axis.

3.4.3 Local density

In order to understand the influence of the surface on the molecule, we can see and compare how the electronic structure has changed respect to the free cluster. By getting the local charge density associated to specific energy levels we can see the contribution of each molecular state.

For the first configuration of the silicon cluster Si₂₉H₂₄, we have obtained the charge density that has been depicted in figure 3.20. In this case we have considered four energy intervals. It is important to note that the third energy interval (-4.2,-4.0) eV, is related to the new peak found in the DOS. For this case, the charge density is concentrated at the bottom of the molecule showing that there is a new bond between the surface and the silicon cluster.

For the new configuration of the silicon cluster Si₂₉H₂₄, we have obtained the charge density that has been depicted in figure 3.21.

From the charge analysis, we can see that the net charge for the supported molecules is 0.70596 and 0.8944 for original and modified cluster respectively.

Also, we can see here the charge density associated to the new states found in the DOS of figure 3.19, where (i), (ii) and (iii) are concentrated again at the bottom of

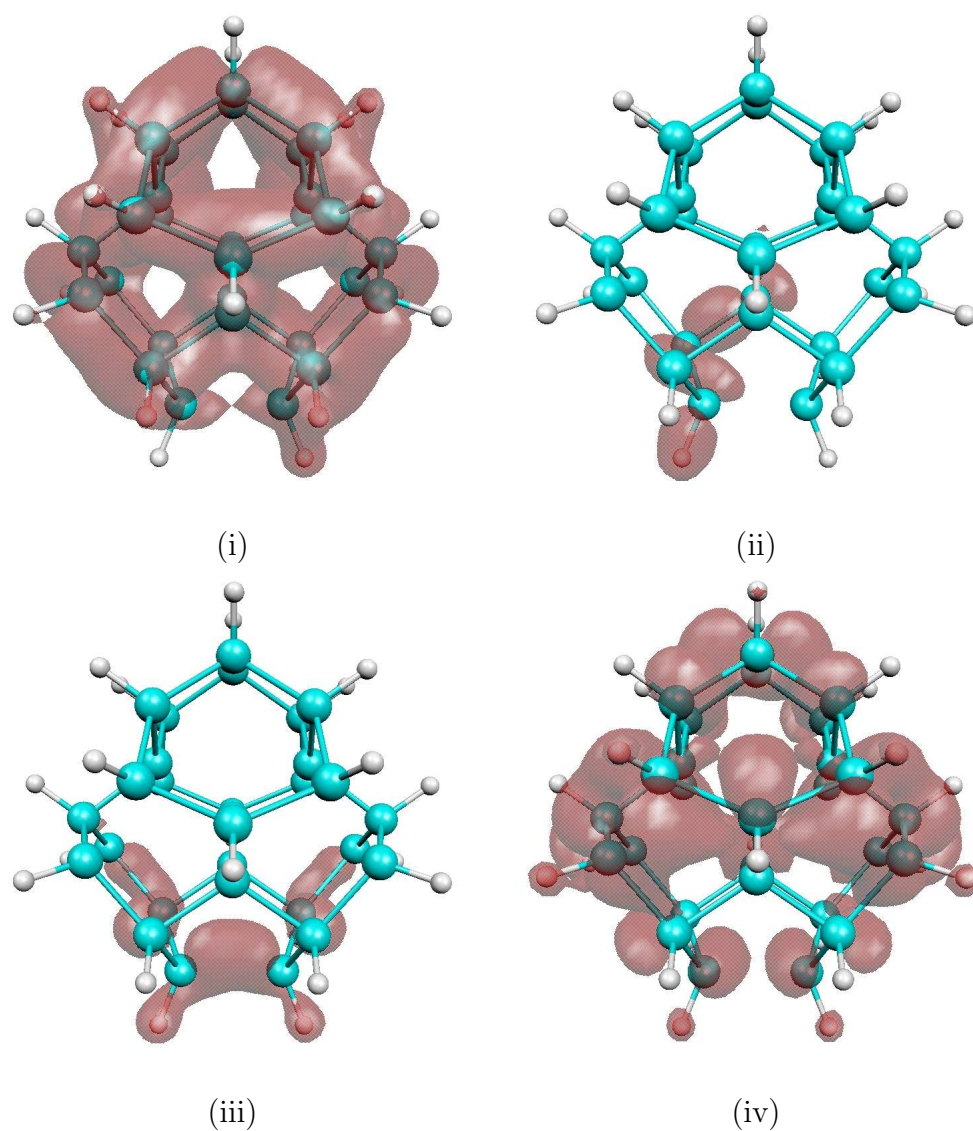


Figure 3.20: Local densities for the $Si_{29}H_{24}$ cluster on Si[111] and associated with specific energy intervals (in eV): (i) (-6.35,-6.15), (ii) (-5.8,-5.7), (iii) (-4.2,-4.0), and (iv) (-3.2,3.0)

the molecule.

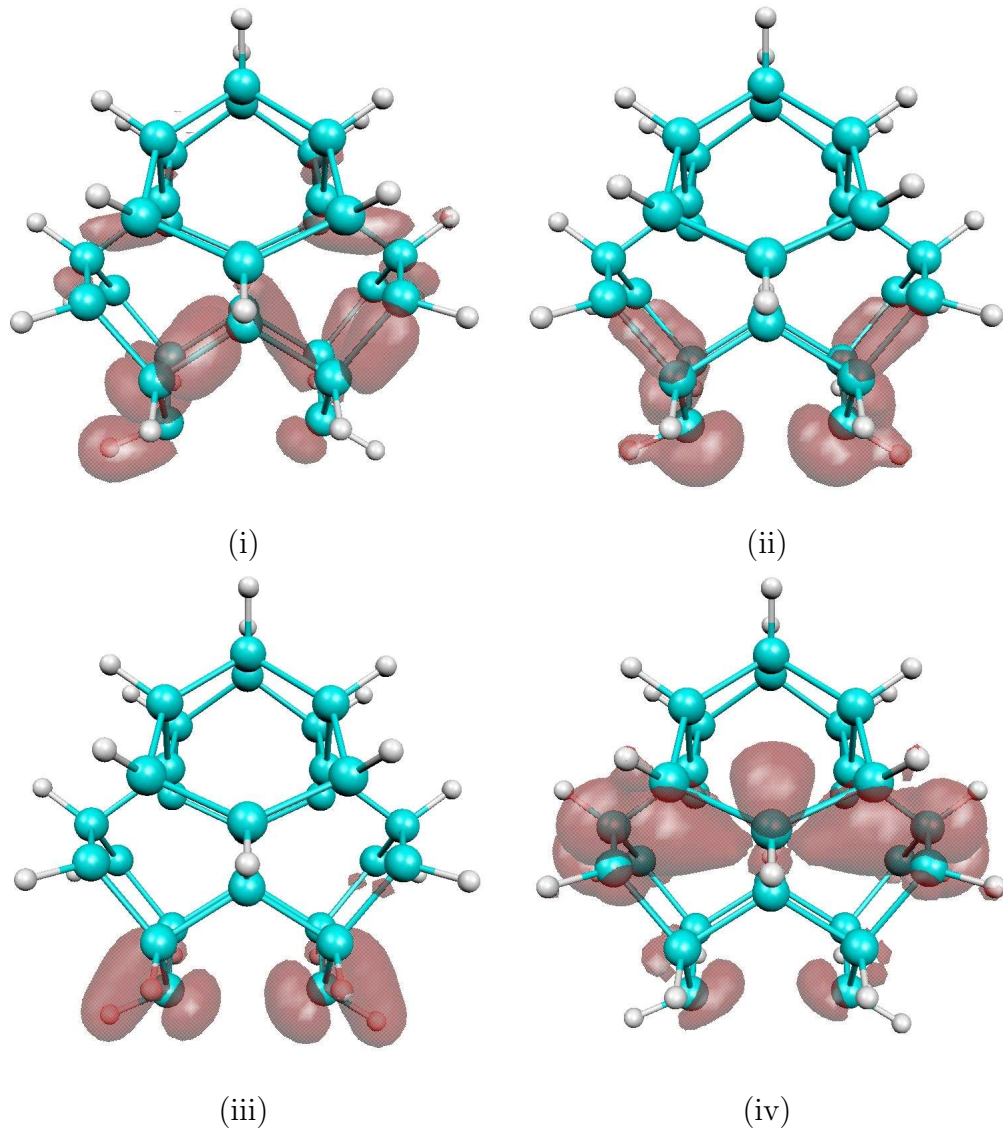


Figure 3.21: Local charge densities for the modified cluster $Si_{29}H_{24}$ on Si[111] and associated with specific energy intervals (in eV): (i) (-6.1,-5.9), (ii) (-4.9,-4.7), (iii) (-4.6,-4.4), and (iv) (-3.2,3.0)

3.4.4 Doped surfaces

We can consider also doped surfaces, where instead of the inclusion of new atoms such as boron and arsenic, the chemical potential was modified to obtain n-type and p-type conditions. In the figure 3.22 we can see the displacement given by the different doping and we have found also a charge transfer between the cluster and the surface that is reported in the next table:

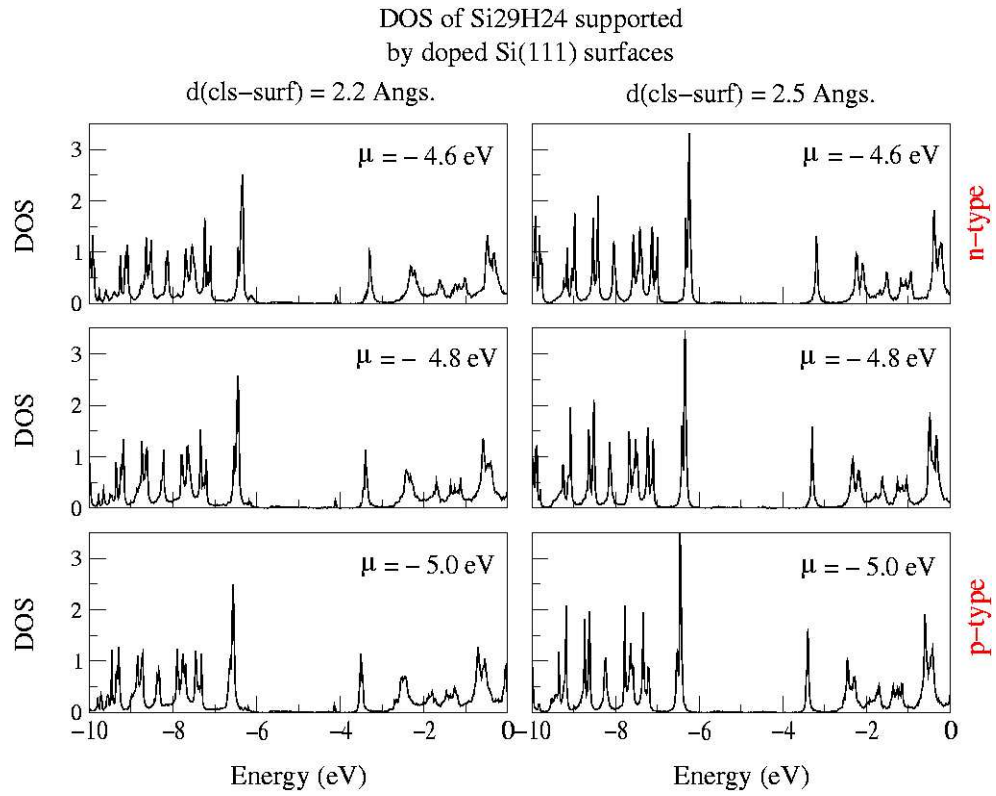


Figure 3.22: DOS calculated for the cluster when is interacting with different doped surfaces.

d(cls-surf)	$\mu_1=-4.6$	$\mu_2=-4.7$	$\mu_3=-4.8$	$\mu_4=-4.9$	$\mu_5=-5.0$	Net
Angs.	charge	charge	charge	charge	charge	
2.2	0.1004028	0.1325684	0.1654968	0.1995544	0.2350616	
2.5	-0.01924367	0.0098188	0.04019987	0.0720236	0.1053664	

charges take into account the presence of different doping and the next step is to evaluate the variation of the I vs V curve that is expected because of the different number of states around the Fermi level which determine the charge transport.

3.5 Part III: Transport properties

The conduction through a silicon cluster is considered in this section where a cluster is supported first by a semiconductor and later by a metallic surface. These two surfaces will help us to consider different regimes for the electronic transport. Also, the cluster-metallic electrode distance has to be long enough to consider only a current given by the tunneling phenomena.

3.5.1 $\text{Si}_{29}\text{H}_{24}$ on Si[111]

In this section, we have considered a flat tip using a Au[111] surface to measure the transmittance and the current through the system (see Fig. 3.23). This has been done because we want to consider a linear variation of the external field applied and also because of the convenience to work with surfaces instead of non periodic cells.

In order to study the coupled system (substrate-molecule), we start considering the electronic properties of the different components disconnected from each other. The silicon cluster is deposited in a silicon semiconductor surface grown along the [111] direction and without reconstruction. Experimentally the surface can exhibit a 2x1, 7x7 reconstruction according to the applied temperature [5,6], but it is also possible to obtain a Si[111]-1x1 structure [20]. The understanding of the transport without reconstruction could also help to differentiate different mechanisms in the case of reconstruction. In this particular case, there are dangling bonds on the unreconstructed surface which are associated with dispersion less energy levels calculated at the band structure of Si[111]. The band structure has been obtained using 24 layers (7 nm of depth) and we find that the electronic and structural properties are in good agreement with theoretical results obtained by Ivanov *et al.* [9]. For the molecule, a H-passivated $\text{Si}_{29}\text{H}_{24}$ silicon cluster has been selected, where the atomic configuration of the cluster in contact with the silicon surface has been geometrically optimized following the LSDA theory, to find the atomic structure with the lowest energy. The optimal distance between the silicon cluster and the surface was found at 2.2 angstroms. (distance between silicon atoms on the surface and hydrogen atoms of the silicon cluster). Once the relaxed structure has been obtained, the electronic

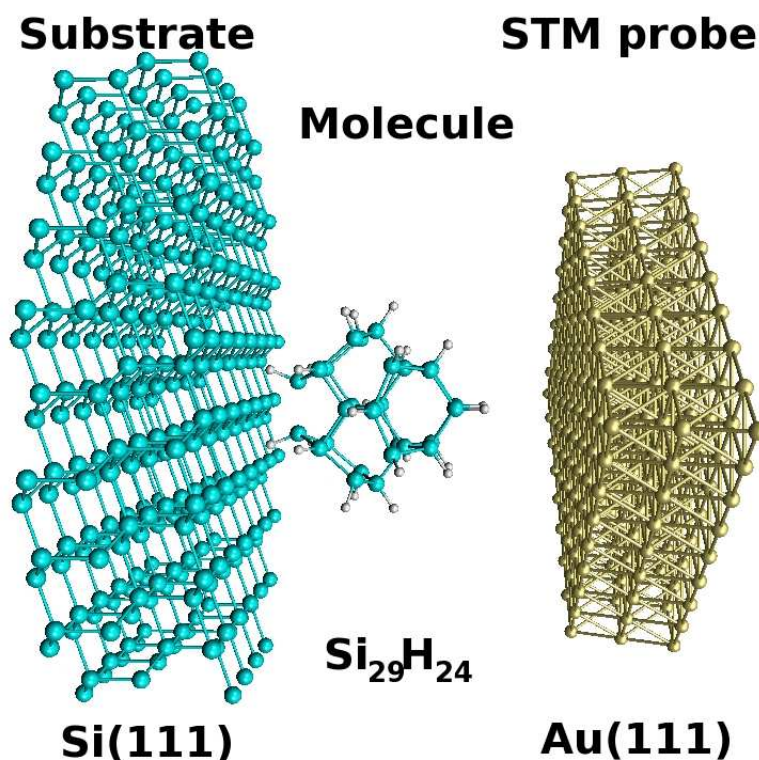


Figure 3.23: Atomic configuration of the silicon cluster interacting, at a given optimal distance, with a semiconducting surface Si[111] and a metallic electrode Au[111] used as a STM probe.

structure (energy levels in the cluster) is calculated using the EHT approach, where the parameter K_{EHT} was fixed at 1.75 and 2.1 for H and Si respectively [21]. The distribution of calculated molecular energy levels, close to the Fermi level, are in good agreement with the results obtained with a LSDA approach and the HOMO-LUMO difference of 3.04 eV (3.01 eV in the case of LSDA) is also in good agreement with other studies previously reported and based on first principle calculations [2, 22].

Figure 4.5 shows the electronic configurations of the isolated components and the coupled case that has been calculated following the EHT approach. Figure 4.5-(A) corresponds to the discrete energy levels associated with the free cluster $\text{Si}_{29}\text{H}_{24}$. Figure 4.5-(B) is the e-DOS of a Si[111] surface where a energy gap of 0.45 eV is observed and the contribution of dangling bonds are present mainly at 0.75 eV below the Fermi level. This description is in good agreement with the results reported by Pandey [17] and Schlüter [18], obtained using a semiempirical tight-binding method

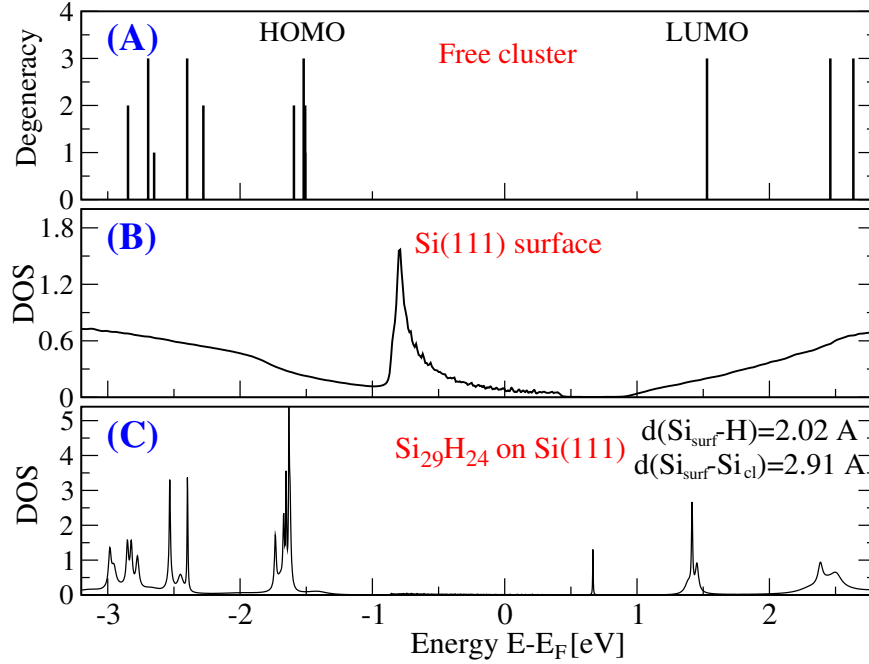


Figure 3.24:]

Electronic structure of the system. Graph A shows the energy levels of $\text{Si}_{29}\text{H}_{24}$ for the isolated case, whereas B shows the DOS of Si[111] and finally C corresponds to the DOS of $\text{Si}_{29}\text{H}_{24}$ cluster on ideal Si[111].

and a self-consistent pseudopotential respectively. The presence of the dangling bonds is observed in these cases with a general shift of the states compared with our results. After the molecule is absorbed on the surface, a total shift and broadening of molecular levels are found in the e-DOS, as observed in fig. 4.5-(A). A new peak is also found around 0.7 eV above the Fermi level. A similar behavior in the DOS has been found when we have considered different positions for the molecule on the surface keeping fixed the same cluster-surface distance. After the equilibrium, and for the calculation of transmittance, current and conductance, a second electrode is considered as a STM probe that can be assume to be a metal slab compared to the molecular diameter. This electrode is a planar and ideal Au[111] surface, which happens to be numerically convenient to obtain the Green's functions of the surface based on a periodic cell. Both electrode and surface are initially at local equilibrium and with chemical potentials $\mu_e = -5.26$ eV and $\mu_s = -4.8$ eV respectively [19]. We follow changing the chemical potential of the metallic electrode forcing it to be at

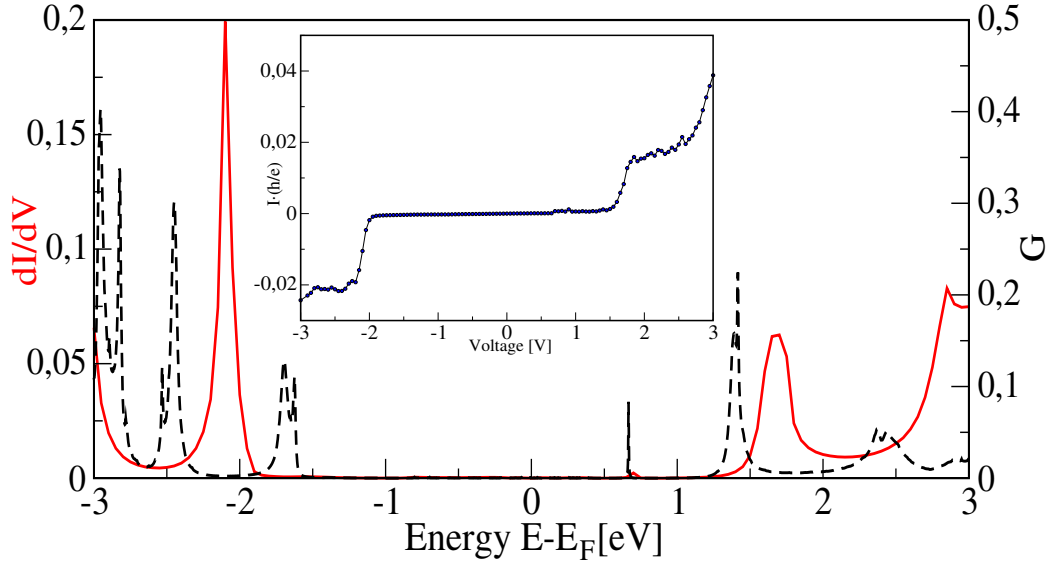


Figure 3.25: dI/dV (solid line) and conductance (dashed line) as a function of the applied bias. The inset shows the current for the Si[111]- Si₂₉H₂₄ - Au[111] system as a function of voltage. The optimal cluster-surface distance considered is 2.2 ang.

equilibrium with the surface. Then, an external voltage bias V is applied when μ_e is changed, and the molecule is embedded in an electric field created by the contacts. By changing the applied bias V , the molecule is then embedded in an electric field created by the contacts. In this situation, the transmittance $T(E, V)$ is calculated, and the current at the applied voltage can be obtained by integrating the transmittance function in the specific energy interval associated to each bias V .

We have also considered doped surfaces, prepared to modify the availability of electrons in the surface. This effect allows to change the number of states close to the Fermi level that are important in transport processes. A simple approach to characterize this effect considers the variation of the chemical potential leading to three regimes: undoped, p-doped and n-doped cases. Another factor is the electrode(tip)-cluster distance, which has been studied by considering $d(\text{cls-tip}) = 4, 5$ and 6 ang. In this case, the current shows only a change in the intensity in agreement with the exponential decay of current as a function of the distance.

Figure 4.6 presents the differential conductance dI/dV , conductance G and in the inset the I-V characteristic for Si₂₉H₂₄ cluster on the surface considering 2.2 ang. as the optimal cluster-surface distance. The dI/dV curve shows the peaks distribu-

tion as a function of applied voltage. It is important to notice that the peak initially located around 0.7 eV (see G in fig. 4.6) is reported in the conductance but its contribution in the dI/dV and the I-V characteristic is barely noticed compared to the next peak located around 1.5 eV above Fermi level and that increase the current at voltages bigger than 1.5 V.

The figure 4.8 shows the evolution of the states in the DOS when an external bias

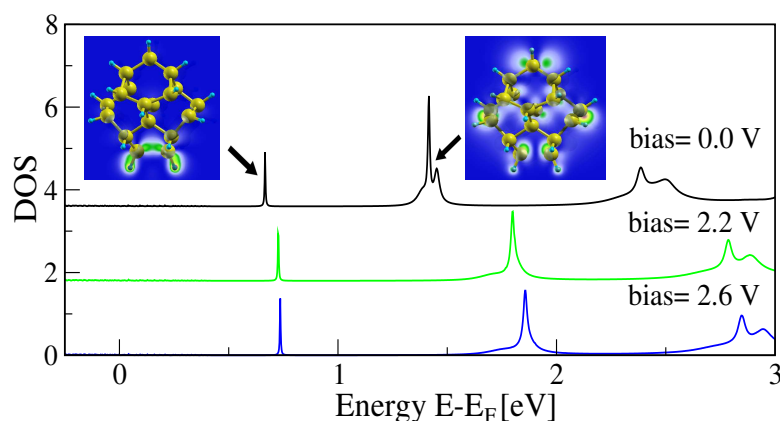


Figure 3.26: DOS as a function of the applied voltage. Also, charge distribution of the new peak is depicted as an inset.

is applied. In this case, we can see that the small new peak at 0.7 eV (charge density of the peak is depicted in the DOS in Fig. 4.8), obtained from the cluster-surface interaction, does not shift its position, compared to the other states. This behavior can be also observed in fig. 4.6, where the differential conductance dI/dV shows the peak in the same position respect to the conductance G (evaluated at equilibrium). After this, we examine the effect of applying a negative bias to see the evolution of the states when the potential profile is given in the opposite direction. In this case, we have considered the last occupied state (located at -1.65 eV) and showed the voltage effect on the DOS of $\text{Si}_{29}\text{H}_{24}$ (see fig. 4.10). Charge distribution of the last occupied state (A) is depicted in Fig. 4.10 within the case when voltage bias of -3.0 V is applied (B). As soon as the voltage is more negative, peaks are shifted to the left, respect to the surface Fermi level, and the labeled peak in the DOS of the molecule is splitted in two separated states.

This evolution is confirmed when we observe the charge distribution associated with

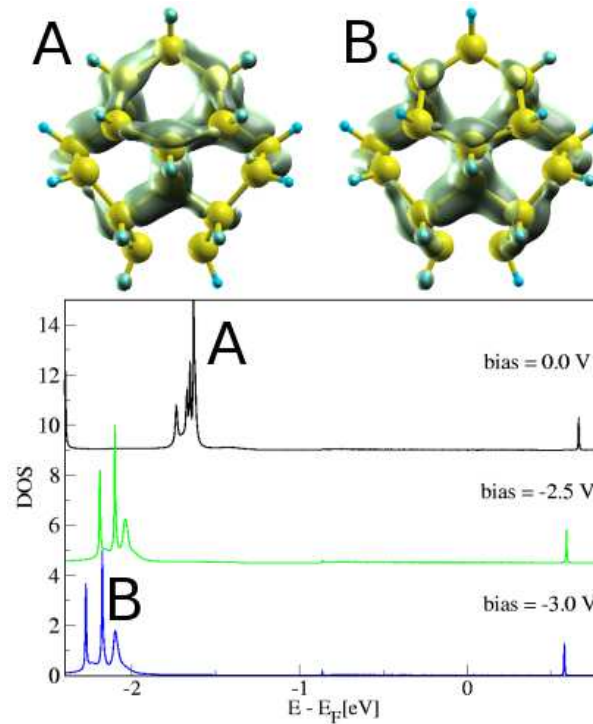


Figure 3.27: The up figure shows the distribution of the charge density of Si₂₉H₂₄ associated with a specific peak in DOS at 0.0 (A) and -3.0 V (B). The figure below shows the calculated DOS at different applied voltages.

this peak (upper figures in fig.4.10). A polarization of the electronic charge in Si₂₉H₂₄ cluster, along the direction perpendicular to the surface, is observed. The initial charge distribution (A in figure 4.10), at 0 V, shows a non-symmetrical distribution whereas when the applied bias is -3.0 V a symmetrical distribution is obtained.

We have also considered doped surface following a simple approximation based in an artificial shift of the Fermi level in order to simulate the inclusion of dopant atoms, such as P or S, on the surface. Considering the initial chemical potential ($\mu_s = -4.8$ eV), a n-type surface was defined for $\mu_s = -4.3$ eV, whereas for the p-doped case, the chemical potential was fixed at $\mu_s = -5.3$ eV. For both cases, an energy shift of the DOS is obtained respect to the initial condition and the I-V characteristics shows a similar displacement, depicted in Fig.4.11. The influence of the new found peak is still neglected in these cases, because it is still localized in the energy gap of the surface. Also, the shift of the new peak is smaller compared to the other peaks (see DOS in Fig.4.8), because this state is associated to the cluster-surface

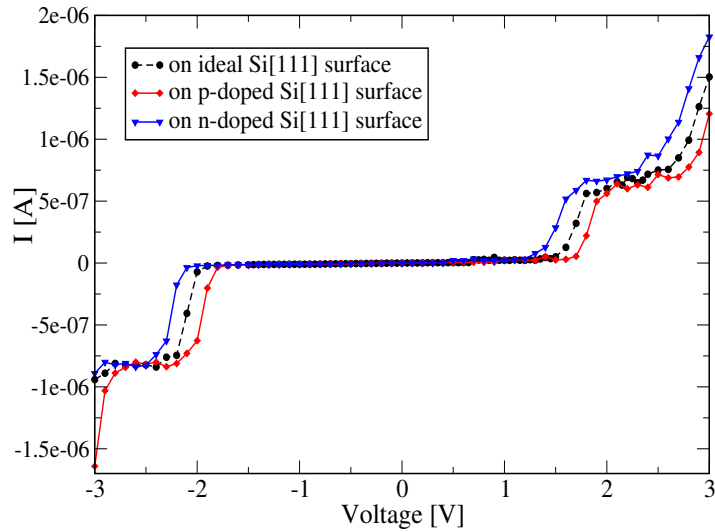


Figure 3.28: Calculated current through the surface-molecule-electrode system considering doped surfaces (n-type and p-type).

interaction.

3.5.2 Discussion

Here, we have reported a set of electronic transport calculations for the semiconductor-cluster-metal system. In order to understand the transport mechanism, we consider three cases; i) equilibrium case ($V=0$) where $\mu_1 = \mu_2$, there is no current flowing from one electrode to another. ii) For negative bias, the relation $\mu_2 - \mu_1 = -qV$ shows that a flow of electrons goes from the silicon surface to the STM probe throughout the molecular energy levels. Notice that the molecular levels are shifted to the left respect to the surface chemical potential μ_1 , because of the potential created between the electrodes. iii) For a positive bias, we can see that molecular levels are shifted to the right respect to the surface chemical potential, so we can consider electronic transport due to the presence of unoccupied molecular orbitals and available states in the surface.

At equilibrium, as is depicted in fig. 4.5, the cluster-surface interaction has established a new peak in DOS, which can be observed with the charge distribution depicted in fig. 4.8. The net charge of the cluster shows that the cluster has transferred electronic charge to the surface, due to the interaction and this distribution

is modulated by the applied bias under non-equilibrium conditions. The influence of the new peak is also diminished in the fig. 4.6 where the conductance G shows the peak around 0.7 eV and in contrast, the dI/dV and I-V curve show the same peak with almost no perturbation compared to the contribution of the next peak starting at 1.5 eV. This can be explained considering that the new peak (at 0.7 eV) is located inside the region associated to the band gap of Si[111]. Also, the cluster-surface interaction is barely affected by the voltage in the range we have applied it, showing that this is a localized state (charge density depicted in fig.4.8) compared to the rest of the molecular states. In the case of negative bias, we can see that the effect of the electrical field promotes a splitting of the peak A in fig. 4.10. The charge density for this peak (going from A to B) in fig. 4.10, have also redistribution when the bias is increased, leading to a symmetrical distribution (at -3.0 V).

3.5.3 $\text{Si}_{29}\text{H}_{24}$ on Au[111]

In order to see the difference between metallic and non-metallic surfaces, we have considered the same cluster $\text{Si}_{29}\text{H}_{24}$ supported by a metallic surface Au[111]. This case is important because of the nature of the DOS associated to the surface that does not present energy gap. The chemical potential is -5.26 eV, which is the same value used before for the STM probe. The DOS for Au[111] surface has been compared with a reported calculation and is in relatively good agreement. The figure 3.29 shows the electronic configuration of the system, considering the isolated cluster, the DOS of the surface and the coupled case. In this case, we do not find a new peak as in the previous example with the semiconductor . We can find again a similar broadening of the molecular energy levels.

The next step is to evaluate the molecular orbitals for the coupled molecule and this is shown in fig.3.30. We have chosen peaks A and B, initially associated with HOMO and LUMO levels to compare with the states obtained when $\text{Si}_{29}\text{H}_{24}$ is supported by Si[111] surface. Whereas the peak B is similar to the peak B found in fig.4.8, the peak A is rather different compared to the peak A found in fig.4.10. In order to consider a non equilibrium situation we have included another metallic electrode as a STM

probe. The calculated current as a function of the applied bias is shown in fig.3.31 where a ohmic behavior is found. This effect can be understood because of the DOS

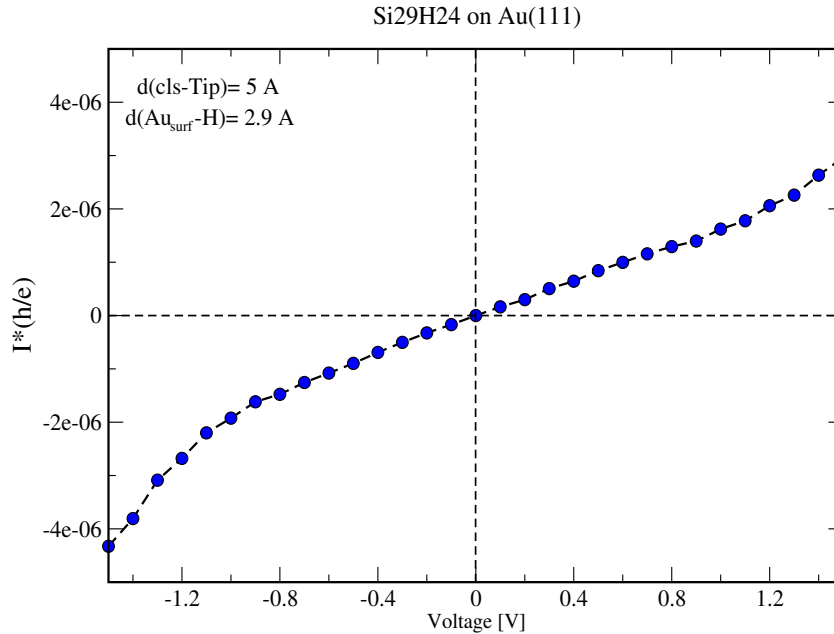


Figure 3.31: Current as a function of the applied bias.

of Au[111], where there is no energy gap, and for low voltages, the most important influence comes from the surface states that are transferred to the molecule. Notice, that for low voltages and due to the energy difference between the HOMO and LUMO levels in the molecule, the initial molecular states (see free cluster in fig. 3.29) are not considered at this point. Also, we have included the redistribution of the charge related to the peak B in the figure 3.32 as a function of the applied voltage. This redistribution is obtained mainly in the direction perpendicular to the surface (which corresponds here to the up-down direction) and due to the potential energy that is created between the metallic electrodes when a external bias is applied. Finally, we have evaluated the DOS and transmittance at different voltages in fig.3.33. In this case we have seen that the peaks are shifted according to the applied bias and that the transmittance calculated for some peaks are smaller than other peaks (see for example the peak located at 1 V respect to the peak located at 2 V).This can be understood because of the natural distribution of the charge density associated to each peak. According to this case we have obtained a description of the charge density that is given only by the molecular orbitals. From

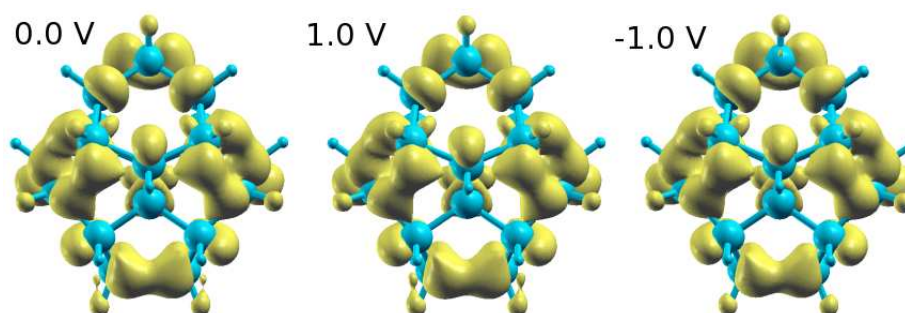


Figure 3.32: Charge distribution of the peak B of fig.3.30 as a function of the applied voltage.

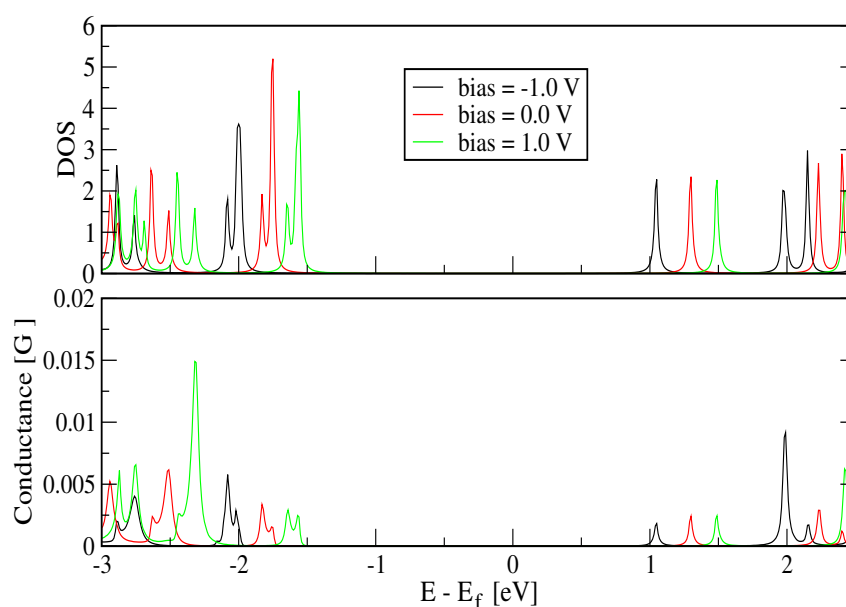


Figure 3.33: DOS and transmittance for the supported $\text{Si}_{29}\text{H}_{24}\text{t}$ different applied voltages.

the DOS we can see (Fig. 3.30) that there is no new peak found due to the interaction produced between $\text{Si}_{29}\text{H}_{24}$ and $\text{Au}[111]$, that is different respect to the previous case with the semiconductor surface previously considered. Also, the absence of an energy gap in the case of $\text{Au}[111]$ has promoted a monotonous increasing current when a low external bias is applied in both directions (Fig. 3.31). This behavior is observed until the bias is high enough (bias \neq 1.7 V) to consider a new conduction channel given by a molecular level.

3.6 Conclusions

We have employed a Hamiltonian based in a extended Huckel model that takes into account only the contribution of the valence electrons. Considering this description, we have obtained the electronic properties associated with several surfaces and molecules, comparing our results with others already published in the literature. The good agreement of calculated DOS, band structures and charge densities, with results obtained with tight-binding methods or *ab initio* calculations, has allowed us to define a suitable parameterization for the system under study. Transport properties have been evaluated considering a system modeled with an extended Hückel model, used to describe the electronic properties in the system. The electronic properties such as DOS and charge density are in good agreement when they are compared with tight-binding and *ab initio* calculations. In particular, for Si₂₉H₂₄ on Si[111], a new peak created by the cluster-surface interaction, was found in the energy gap of the silicon surface. This gap diminishes the effect of the new peak in the I-V characteristic as well as in the dI/dV case. The new state has a charge distribution close to the surface and its position is unaffected by the external applied bias. On the ranges we study, our results show that the position of molecular levels, respect to the surface, is important in order to understand molecular electronic transport. A non-metallic surface has interesting properties respect to metallic ones, allowing to control transport with the appropriate conditions. In our case, we have non-conducting behavior of the system at low voltage (positive and negative cases). Also, we have considered a metallic surface to support the silicon cluster, when the electronic structure and the I-V characteristics have been evaluated. Here we have obtained that the continuous distribution of states observed for the surface promotes an Ohmic behavior of the calculated current when an external bias is applied. Also, These results strength the idea to use silicon clusters as possible components in large voltages valves or diodes in electronic devices.

Bibliography

- [1] G. Binning, H. Rohrer, Ch. Gerber, and E. Weibel. *Phys. Rev. Lett.*, 49:57, 1982.
- [2] G. Belomoin, J. Therrien, A-Smith, S. Rao, R. Twesten, S. Chaieb, N. H. Nayfeh, L. Wagner, and L. Mitas. Observation of a magic discrete family of ultrabright si nanoparticles. *Appl. Phys. Lett.*, 80:841, 2002.
- [3] M. A. Reed, C. Zhou, C. J. Muller, T. P. Burgin, and J. M. Tour. Driving current through single organic molecules. 278:252, 1997.
- [4] D. L. Klein, P. L. McEuen, J. E. B. Katari, R. Roth, and A. P. Alivisatos. *Appl. Phys. Lett.*, 68:2574, 1996.
- [5] M. O. Watanabe, T. Miyazaki, and T. Kanayama. *Phys. Rev. Lett.*, 81:5362, 1998.
- [6] L. Bolotov, N. Uchida, and T. Kanayama. *Eur. Phys. J. D*, 16:271, 2001.
- [7] J. Tersoff and D. R. Hamann. Theory of the scanning tunneling microscope. *Phys. Rev. B*, 31:805, 1985.
- [8] S. E. Baltazar, M. De Menech, U. Saalman, A. H. Romero, and M. E. García. Quantum electronic transport through supported $\text{si}_{29}\text{h}_{24}$ clusters on an ideal si(111) surface. *To be published*, 2007.
- [9] I. Ivanov, A Mazur, and J. Pollmann. The ideal(111), (110) and (100) surfaces of si, ge and gaas; a comparison of their electronic structure. *Surface Science*, 92:365, 1980.

-
- [10] K. C. Pandey. *Phys. Rev. B*, 14:1557, 1976.
- [11] T. Kanayama. *Jpn. J. Appl. Phys.*, 33:L1792, 1994.
- [12] Gallego et al. Electronic structure of the ideally h-terminated si(111)-(11) surface. *Phys. Rev. B*, 61:12628, 2000.
- [13] W. C. W. Chan and S. Nie. *Science*, 281:2016, 1998.
- [14] G. Belomoin, E. Rogozhina, J. Therrien, P. V. Braun, L. Abuhassan, and M. H. Nayfeh. *Phys. Rev. B*, 65:193406, 2002.
- [15] N. P. Guisinger, M. E. Greene, R. Basu, A. S. Baluch, and M. C. Hersam. Room temperature negative differential resistance through individual organic molecules on silicon surfaces. *Nano Letters*, 4:55, 2004.
- [16] M. J. Frisch et al. *Gaussian 98, Revision A.9*. Gaussian Inc., Pittsburgh PA, 1998.
- [17] K. C. Pandey and J. C. Phillips. Atomic densities of states near si(111) surfaces. *Phys. Rev. B*, 13:750, 1976.
- [18] M. Schlüter, J. R. Chelikowsky, S. G. Louie, and M. L. Cohen. Self-consistent pseudopotential calculations for si(111) surfaces: Unreconstructed (1x1) and reconstructed (2x1) model surfaces. *Phys. Rev. B*, 12:4200, 1975.
- [19] F. G. Allen and G. W. Gobeli. *Phys. Rev.*, 127:150, 1962.
- [20] A. Khan. *Surf. Sci. Rep.*, 3:193, 1983.
- [21] J. Cerda and F. Soria. *Phys. Rev. B*, 61:7965, 2000.
- [22] G. Allan, C. Delerue, and M. Lannoo. *Phys. Rev. Lett.*, 76:2961, 1996.

Chapter 4

Transport properties in organic molecules

4.1 Introduction

Electronic transport through supported organic molecules on substrates has interesting applications in several fields such as electronics medicine, engineering. This idea has been extensively studied in the last years, because of the possibility of create new electronic dispositives at atomic scale. One of the major goals in this area is related to the control of the transport properties, where a metallic or semiconductor surface is interacting with some molecules. In this situation, channels responsible of the electronic flow depend not only of the molecular levels, but also of the position of the Fermi level associated with the surface. The interaction between molecules and substrates can give the opportunity to design electronic components such as diodes, information storage devices, nanowires, molecular switches, rectifiers, etc. Recently, negative differential resistance effect (NDR) of organic molecules on heavily doped Si substrates has been predicted theoretically [1] and experimentally [2]. In this case, a styrene molecule has been deposited on a Si[100] surface, considering the doping in both conditions, n-type and p-type surface. After this a metallic tip of a STM device is introduced in the system. The authors have found that the energy shift of the molecular levels, in particular, the crossing of the HOMO or LUMO levels of the band edge of the underlying semiconductor is the main responsible for

the diminished current when a bias voltage is applied .

About transport properties, inclusion of other molecules such as metallic nanocrystals or organic molecules between two electrodes have shown a diode-like behavior or a change in the tunneling conductance [3,4]. These results have reinforced the idea to use molecular systems as active structures in electronic components at nano scale. Experimentally, the inclusion of an organic system (liquid crystal) has reported the evidence of a Coulomb charging [5] effect.

In this chapter, we want to consider the electronic transport throughout of organic molecules on a semiconductor surface where non-ohmic behavior can be observed due to interaction between both systems [6]. The case of styrene molecule has been previously reported in the literature, but in this case we have performed a relaxation of this molecule not just for the isolated case, but also considering the interaction with a surface and following a LDA approximation to obtain an optimized geometry. The coupled system (molecule-surface) is studied focusing our interest in to determine how the molecular structure is changing, within with its electronic properties such as DOS. Initially, properties are evaluated at equilibrium, and after that a STM probe is included in the system to simulate the spectroscopic calculations following the idea of Tersoff *et al.* to study conductivity of molecules. To consider non-equilibrium conditions, both electrodes, are kept in local equilibrium but with different chemical potentials μ_1 and μ_2 . Due to the self-consistent calculation of the potential field and the electronic density, we have evaluated not just current, but also conductance and charge transfer between the molecule, the substrate and the metallic electrode.

We have also considered the effect given by the internal structural change in molecules on the electronic transport. To achieve this goal, we have selected a biphenyl molecule where a twist in the rings can provide a new behavior in the electronic transport. The study of the I-V characteristics and DOS is used to describe the difference in transport properties as a function of the angle between the aromatic rings. Finally some conclusions about the results are given comparing our results with other reports and possible new directions for this work are considered.

4.2 Components

The interest of this work is to study non-metallic surfaces like the first one showed in the previous chapter (fig. 3.1-a), which is again a semiconductor silicon with orientation [111] and without reconstruction.

4.2.1 Surface

Reconstructed and passivated surfaces are mainly observed in experiments [7,8], but it is also possible to work with ideal surfaces and the study of its electronic properties are important to understand mechanism of reconstruction.

Absorption of silicon clusters has been studied at both theoretical [9,10] and experimentally [7,11].

Figure 3.1 shows the first case using an ideal silicon surface with [111] orientation. In general, surfaces are reconstructed to minimize its energy, however it is possible to experimentally produced unreconstructed surfaces and the study of its electronic Al properties are important to understand the reconstruction processes. The system posses a diamond-like structure with a lattice parameter $a = 5.43$ ang. Besides this, band structure has been calculated from geometric considerations and following a hexagonal path of k points. Considering a larger number of layers, a better resolution of allowed energy levels can be achieved, so then we have taken surfaces with a depth of 24 layers from the surface (7 nm approx.). Also, for the tight binding model, interaction between layers is considered until third neighbors. Fermi energy for silicon has been established between the gap given by the ionization energy and the electronic affinity. The chemical potential was also fixed at -4.8 eV, and from the results, we have obtained an associated gap (indirect) of 1.2 eV.

4.2.2 Styrene molecule

Within the silicon cluster, it is important to see the effect in quantum transport when an organic molecule like a styrene $C_6H_5CH = CH_2$ or C_8H_8 r others like vinyl

benzene is deposited on a semiconducting surface. The first molecule is obtained in the nature from plants and in the industry from benzene and was initially used to obtain synthetic rubber, food containers, etc .

For this molecule we have studied two possible configurations. Both cases were obtained after an optimization of this molecule interacting with the surface. One of this (labeled as case A) has been previously studied by Datta *et al.* finding a negative differential resistance effect for doped surfaces.

The figure 4.1 shows the first configuration where the hydrogen atoms close to the surface modify their positions respect to the isolated case. The HOMO-LUMO difference calculated with the EHT approach is 0.95 eV.

The next figure (4.2) shows the molecular orbitals associated with the first config-

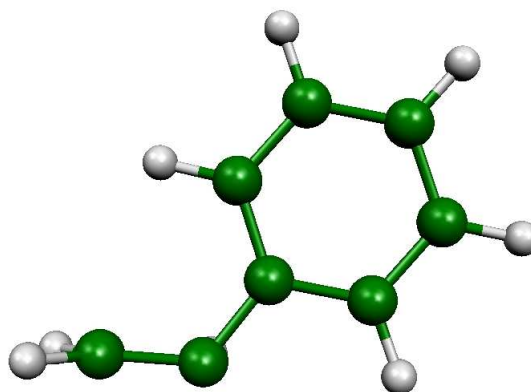


Figure 4.1: First styrene configuration interacting with the silicon surface.

uration of styrene ($C_8H_8^A$). To calculate this, we have isolated the molecule and evaluated the HOMO and LUMO levels. The LUMO level shows that the molecule is able to accept electrons at the bottom of the molecule. The other configuration ($C_8H_8^B$) for the styrene molecule is the one depicted in the figure 4.3. In this case, hydrogen atoms are located with a different orientation respect to the isolated case. HOMO-LUMO difference in this case, was obtained at 3.2 eV and the distribution of the states has a similar description respect to the energetic minimization with a LSDA theory. Also, we can see molecular orbitals in fig.4.4, that indicate that the molecule is less suitable to accept electrons in the first unoccupied level (LUMO). To consider that different colors (white and blue) denote different signs for the wave-

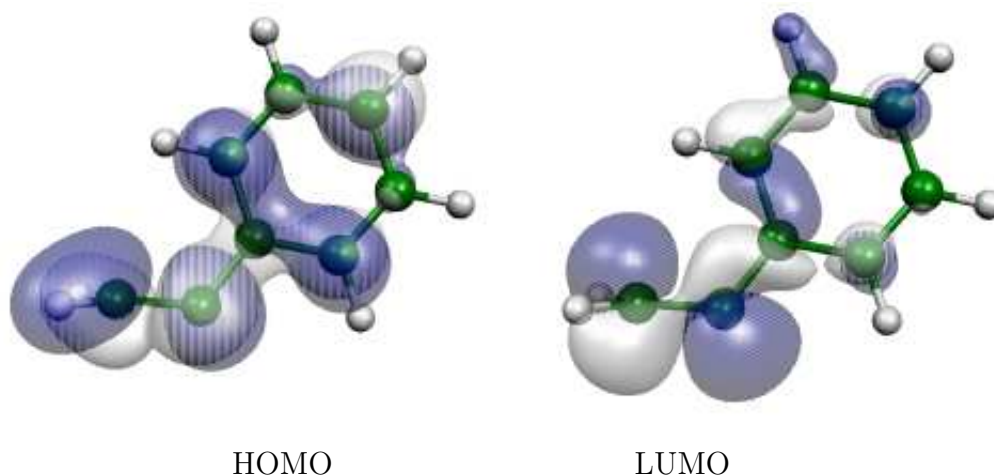


Figure 4.2: Molecular orbitals for the first styrene configuration interacting with the silicon surface.

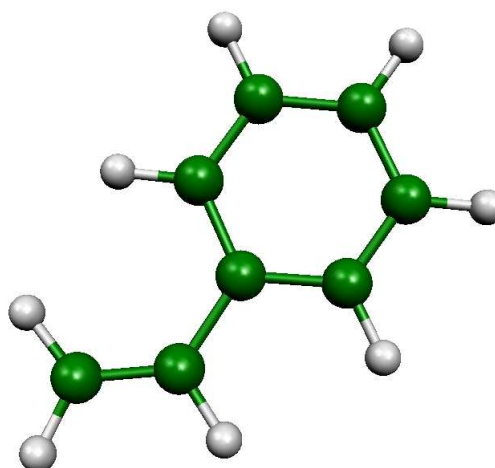


Figure 4.3: Second styrene configuration interacting with the silicon surface.

function associated to the orbital. In this case, we can see that the LUMO is not oriented towards the bottom of the molecule, in contrast to the first case, but it is more spread around the molecule. It is important to notice that for the isolated case, the case B is energetically more stable than case A (result obtained with the EHT and the LSDA theories).

using EHT model (with the parameters defined in chapter II for C, H, Si and Au) and compared with ab-initio calculations finding a good agreement between them.

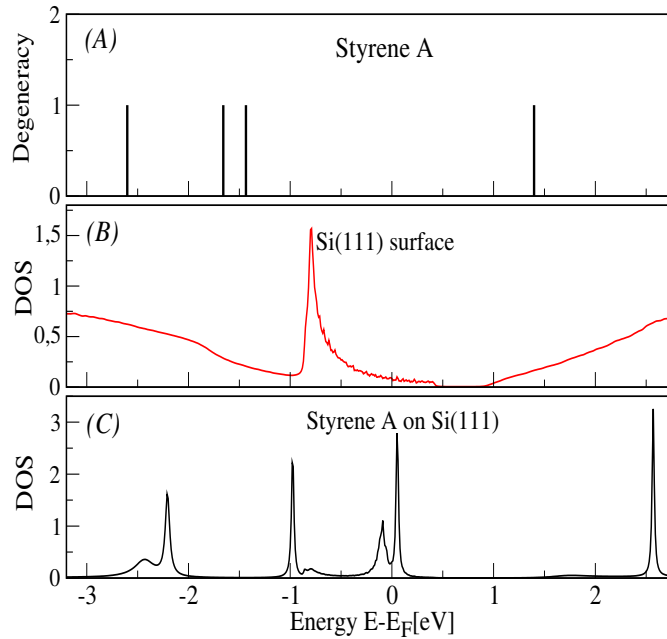


Figure 4.5: Electronic structure of the $C_8H_8^A$ -Si[111] system. Graph A shows the energy levels of $C_8H_8^A$ or the isolated case, whereas B shows the DOS of Si[111] and finally C corresponds to the DOS of $C_8H_8^A$ on ideal Si[111].

In order to evaluate equilibrium and non equilibrium conditions we have considered a periodic and ideal surface where the molecule-surface distance is taken from the previous energy optimization of the coupled system. Figure 4.5 shows the electronic structure of the system. In Fig. 4.5-A the electronic levels of the free molecule is presented. Below this, the DOS of the Si[111] surface is calculated where a gap of 0.45 has been obtained and dangling bonds are located around 0.7 eV below the Fermi level. Finally, in Fig. 4.5-C the DOS of the molecule interacting with the surface is shown. The energy levels of the free cluster are broadened and shifted to the right in the coupled case due to the cluster-surface interaction. As a consequence, there are states close to the Fermi level and the gap of the surface.

4.3.2 Transport properties

After the equilibrium conditions, we have included a metallic electrode to evaluate transport properties. As a first approach, an ideal Au[111] surface is considered as an electrode. Initially, Both electrode and surface are imposed to be at local equilibrium and with chemical potentials $\mu_e = -5.26$ eV and $\mu_s = -4.8$ eV respectively [13]. Under non-equilibrium conditions, an external bias V is imposed by changing the chemical potential of the metallic electrode. Then the transmittance $T(E, V)$ is calculated and the current can be obtained integrating the transmittance in the energy range associated to each bias. Here we are assuming the low temperatures regime where the Fermi function defines a energy window where the transmittance contributes to the electronic transport. I-V curve is shown in Fig. 4.6 where the applied bias goes from -3.0 to 3.0 V. We can observe that a NDR effect for a positive applied bias is observed. The intensity of the current starts to decrease at 0.5 V, finding a minimum around 1.5 V where the current starts to increase again. This effect has been also experimentally reported for styrene supported by Si(100) [2]. In order to

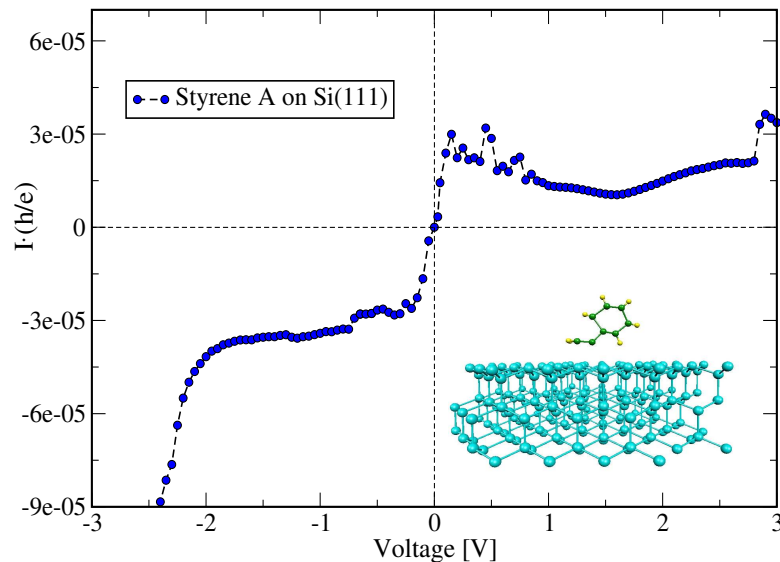


Figure 4.6: I-V characteristics of the system as a function of voltage and considering an interval of -3.0 and 3.0 V.

evaluate the conditions of the system to obtain the NDR effect, Fig. 4.7 describes the behavior of the molecular states close to the Fermi level. We can see the shifting effect as a function of the applied voltage. In particular, the molecular level at

0.2 above the Fermi level has a drop in the calculated transmittance after a bias of 1.6 V is applied. This peak provides an important contribution to the current at low voltages and its charge distribution, depicted also in Fig. 4.7 and close to the surface (no depicted), shows a direct relation to the surface located below the molecule. The behavior of this peak will be crucial when we have to explain the

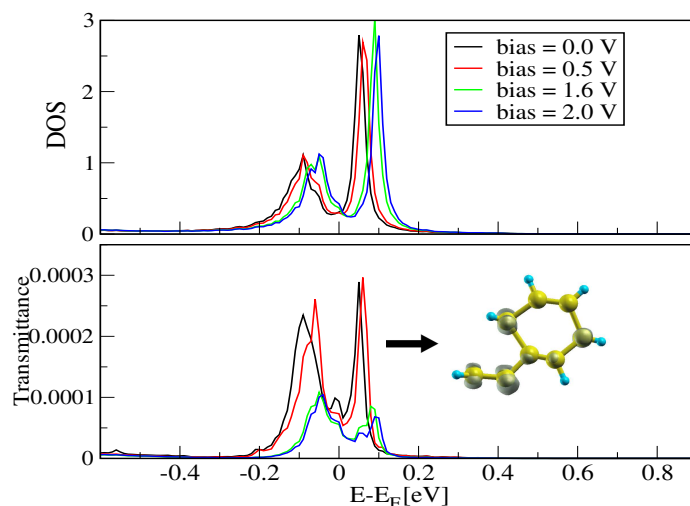


Figure 4.7: Calculated DOS and Transmittance close to the Fermi level. Also, the charge density associated to the peak located around 0.3 V above the Fermi level is depicted as an inset.

major contribution to the NDR effect, because is the main peak located in the right part of the DOS respect to the Fermi level (that in this case was considered at -4.8 eV). In fig. 4.8 the DOS of the styrene molecule is compared with the differential conductance dI/dV as a function of the energy. In order to calculate the differential conductance we have used the approximation given by Tian *et al.*, where dI/dV is proportional to the transmittance T . In the case of dI/dV , we can see not just a shift of the levels respect to the DOS but also the magnitude of some peaks clearly decrease, compared to other peaks that were observed from the DOS. This result shows the molecular states that indeed contributes to the electronic transport in the system. The next step has been to evaluate the doping effect in the surface. To consider doped surfaces, we have used a simple approach without the inclusion of new atoms in the system and only modifying the Fermi level of the substrate. We have considered three cases where the chemical potential of the surface is evaluated

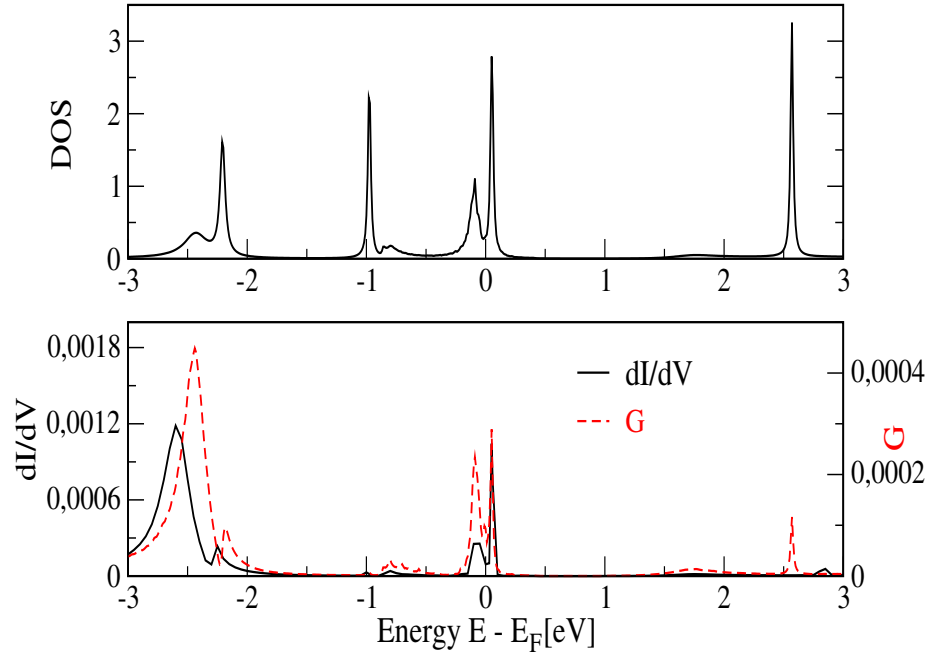


Figure 4.8: Calculated DOS and differential conductance dI/dV for the C_8H_8 molecule.

at $\mu_s = -4.8$ eV (initial case), -4.3 eV (n-type) and -5.3 eV (p-type). For each case we will have different equilibrium conditions, according to the chemical potential μ_s . Considering the metallic electrode in the system, we have calculated the transmittance in the system and then the current $I(V)$. This result has been depicted in Fig. 4.9 using voltage range from -3 to 3 V. In this figure we can see that the n-type surface shows a similar behavior compared to the original case ($\mu_s = -4.8$ eV), where the NDR effect at positive bias is well described. In contrast, in the case of the p-type surface, the result is rather different. The NDR is not found at positive bias and even the behavior at negative V is also different from the previous cases. In order to understand the new conditions of the system, Fig. 4.10 presents the DOS and the differential conductance for doped surfaces. Even considering that the peaks of DOS are observable in each case, we can see that peaks are not only shifted but also the magnitude is changing. In the case of dI/dV , we have that the peaks are again shifted and also changed in magnitude. One of the important aspect of the doping, is that molecular states have been also shifted according to each case, and in particular, the n-type surface have moved the molecular states to the region

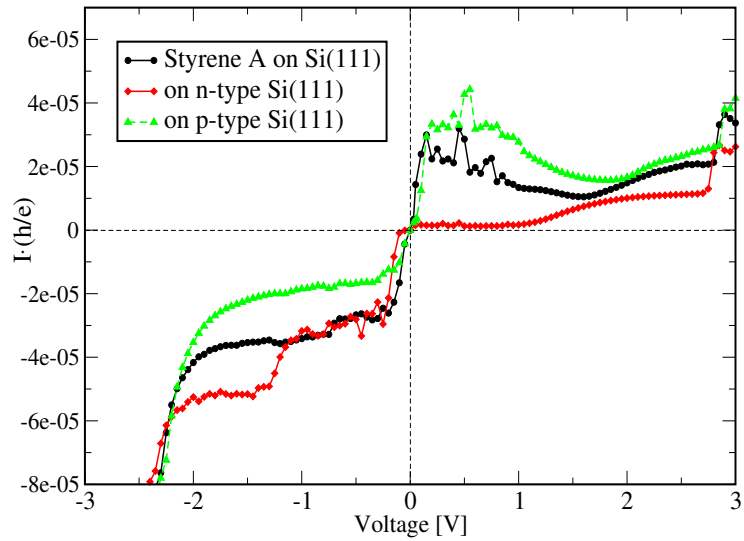


Figure 4.9: I-V characteristics for doped surfaces. To consider doped surfaces, the surface chemical potential μ_s is adjusted considering three cases.

of the calculated gap for the surface Si[111] (see Fig. 4.5) In the figure 4.10, we

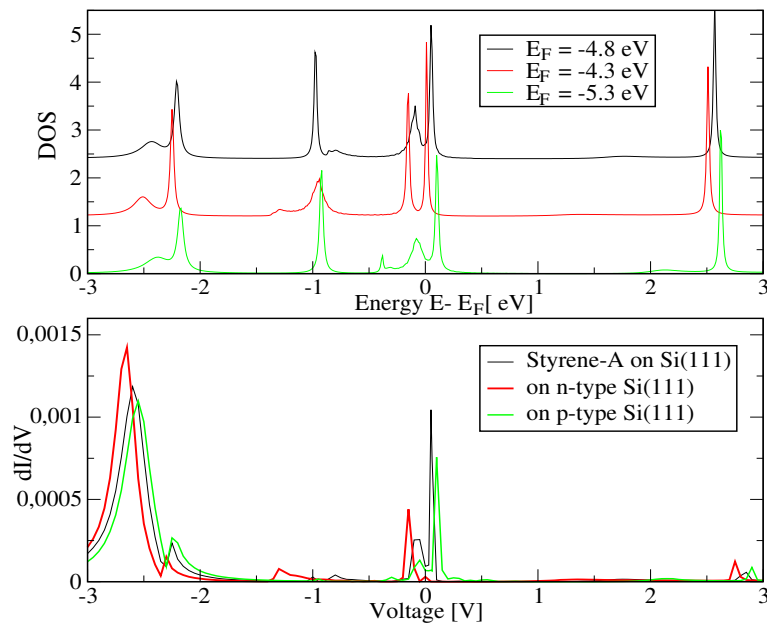


Figure 4.10: DOS and dI/dV characteristics for doped surfaces. To consider doped surfaces, the surface chemical potential μ_s is adjusted considering three cases.

can see the DOS is shifted respect to the Fermi level which is different in each case, and thus the zero energy position is also different for them. Finally, another case that we have considered is the inclusion of tips in the electrode. This has been

achieved considering two tips with similar pyramidal structure and different number of atoms (we have include only one case in fig. 4.11). The molecule-tip distance for the small tip is 4.4 ang. and 5.0 for the big tip. For the flat electrode, we have considered a distance of 5.2 ang. These distance are long enough to consider only tunneling current between the molecule and the tip/surface. Fig. 4.11 shows the

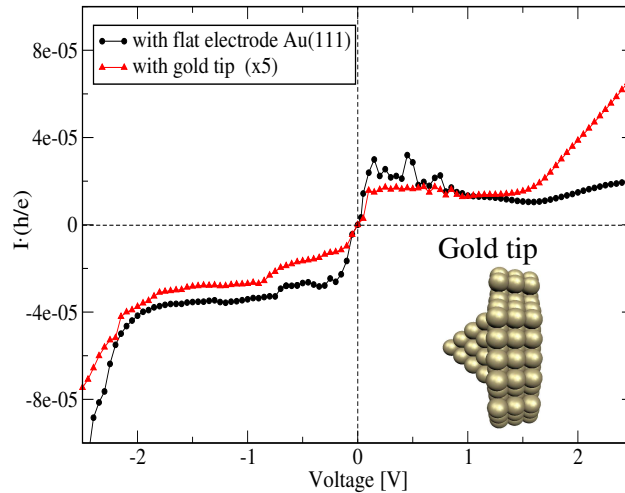


Figure 4.11: I-V characteristics considering different probes. Results using a flat electrode are compared two gold tips.

I-V characteristics for the different cases. In the case of the big tip, the current was multiply by 5 due to the bigger distance considered. We can see that at low voltages (positive and negative), the behavior is rather similar, but this description changes when the bias is higher in the positive direction. The description of the DOS and the dI/dV in fig. 4.12 shows different behavior in the distribution of the states and in the importance of the states located close to the Fermi level. This difference is mainly localized at lower energies and can be attributed to the considered tip.

4.3.3 Second configuration (case B)

The first configuration for the molecule that we have used has the same structure that the one reported in the literature when the styrene is in contact with the surface Si(100). Nevertheless, We have found a second configuration when the styrene molecule is interacting with the Si[111] without reconstruction. The second configu-

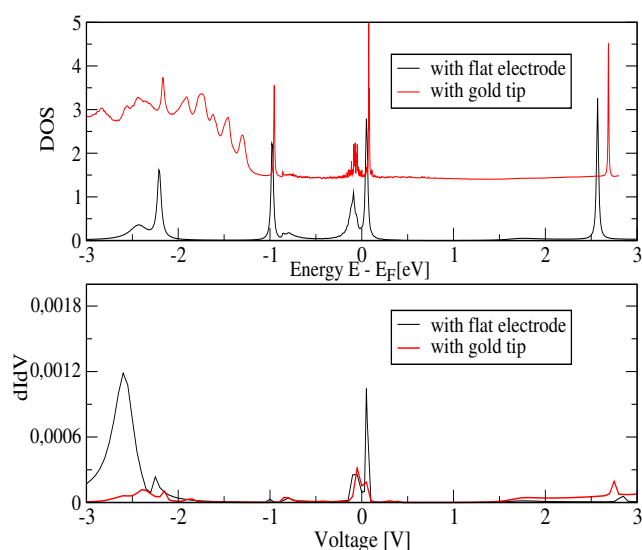


Figure 4.12: DOS and dI/dV characteristics considering different probes. Results using a flat electrode are compared two gold tips.

ration for the coupled system is labeled as case-B (or C_8H_8 -B), and has been depicted in fig. 4.3. This configuration was also obtained from first principles calculations and following a LSDA approach. It is important to notice that the energetic optimization shows that $E(\text{case B}) < E(\text{case A})$, which means that this configuration is more stable. Figure 4.13 shows that DOS of the supported molecule has molecular levels not just close, but also in the energy gap associated to the surface (central graph in fig. 4.13). The two molecular states localized around 0 and 0.7 are the original LUMO and LUMO-1 cases respectively and they will play an important role in the conduction phenomena. After the electronic configuration, I-V curve is shown in fig. 4.14 in the same voltage range as case A. Interestingly, the I-V characteristic does not seem to show a similar NDR effect when a positive bias is applied, like in the first case. Instead of this, there is no an important contribution obtained for the current at low positive voltages. If we want to know about the states that participate in the electronic transport, we can see the differential conductance and the conductance G in fig. 4.15. In this case the contribution of the first state, located initially at 0.7 eV above the Fermi level, is neglected in the dI/dV characteristic compared to other states. Even the conductance and the dI/dV of the state located at 0.2 eV below the Fermi level, is small in comparison to, for example, the states located at 2.3 eV

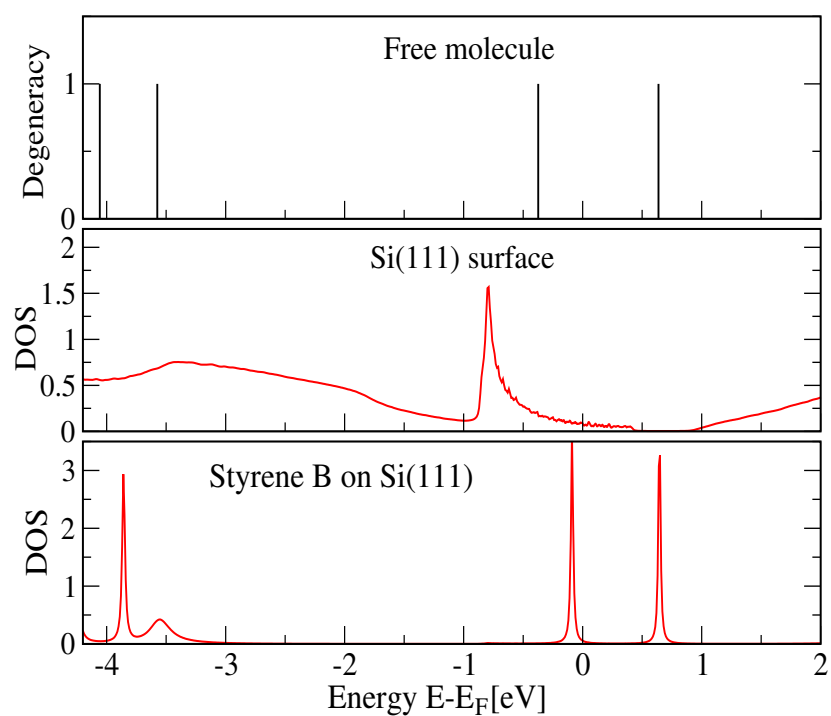


Figure 4.13: Electronic structure of the B-C₈H₈-Si[111] system. Graph A shows the energy levels of C₈H₈ for the isolated case, whereas B shows the DOS of Si[111] and finally C corresponds to the DOS of C₈H₈ on ideal Si[111].

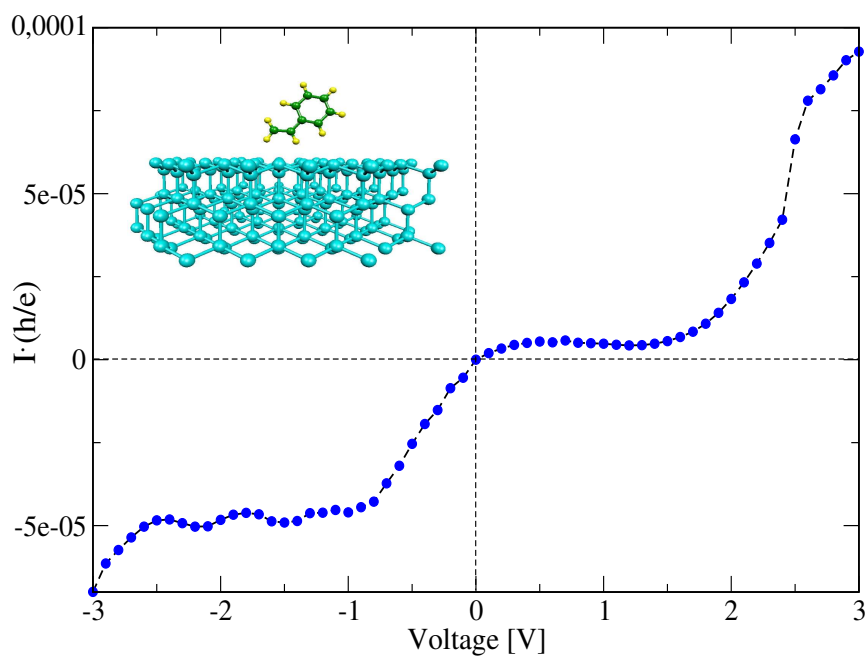


Figure 4.14: I-V characteristics of the system as a function of voltage.

above the Fermi level. There is also a spread distribution of the conductance for low negative values. In this case, there will be important to notice that the energy interval is the same associated to the dangling bonds of the surface. In the next

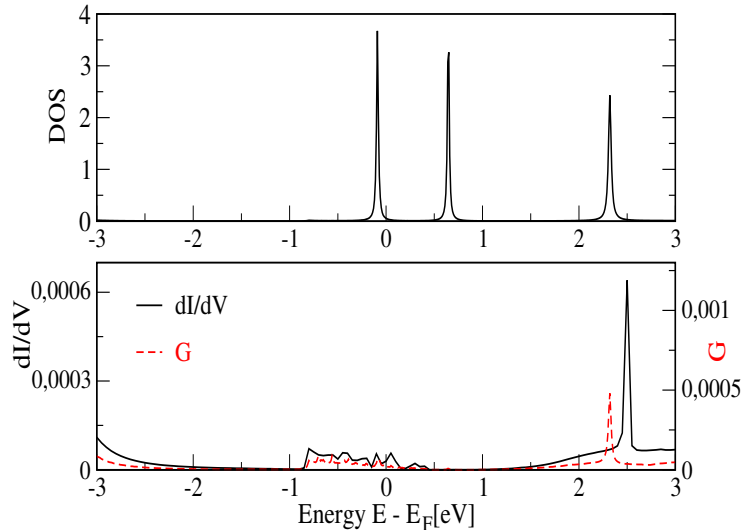


Figure 4.15: DOS and dI/dV characteristics of the system as a function of voltage.

step, the same study used for C_8H_8-A , is applied to consider doped surfaces. They will be characterized modifying the chemical potential and the results are shown in fig. 4.16. This figure shows clearly different results when the substrate is doped in one direction or another. In the first case, we have the same results obtained for C_8H_8-B on Si[111] with a chemical potential of -4.8 eV. When the surface is n-type doped (considering $\mu_s = -4.3eV$), there is no response in the current until 0.7 V, where the intensity starts to increase rapidly when the positive bias is applied. A completely different behavior is obtained when the surface is p-type (which means that $\mu_s = -5.3eV$). Here we can see that a NDR effect is obtained for the current around $1-2$ V, when the positive bias is applied. After 2 V, the current increases its value again in a similar way like the two other surfaces. The figure 4.15 shows the DOS and the dI/dV characteristic associated with each surface. Here we can see that the DOS has been adjusted to each different Fermi level, so the zero position is indeed different in each case. Is important to consider that even with a similar distribution of the states, the differential conductance looks rather different. For the undoped surface, there is no an important peak at low voltages and the main one is

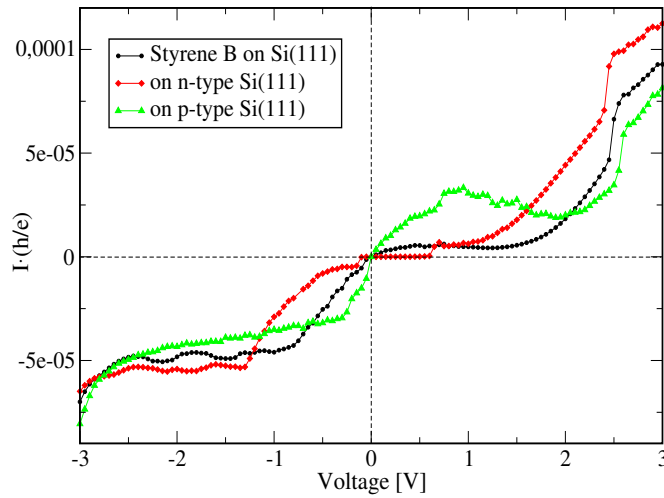


Figure 4.16: I-V characteristics for doped surfaces. To consider doped surfaces, the surface chemical potential μ_s is adjusted considering three cases.

located at 2.4 V, within with a spread contribution is obtained around 0 V. In the n-type Si[111], we can detect an important peak located around 0 V within with the same spread distribution. For the p-type surface, we can see 2 peaks, one located around 0 V and the other one at 0.7 V. For all cases, the same peak, locate around

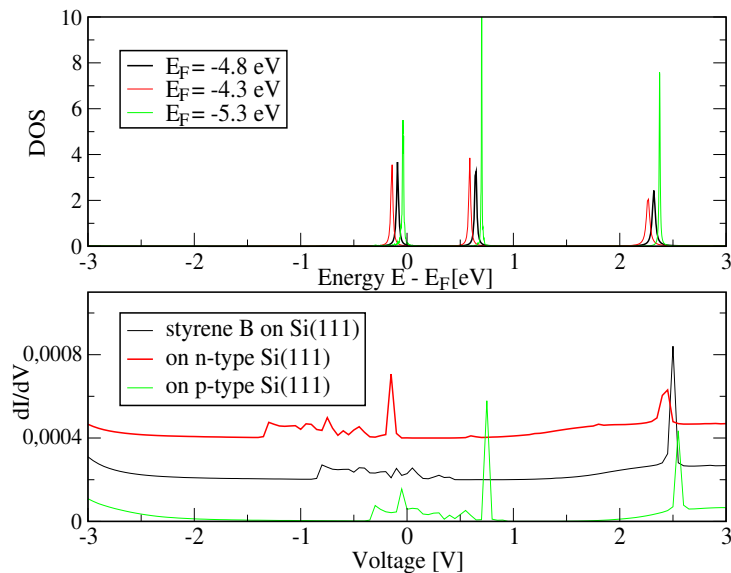


Figure 4.17: DOS and dI/dV characteristics for doped surfaces. To consider doped surfaces, the surface chemical potential μ_s is adjusted considering three cases.

2.5, is clearly depicted in all cases and is related to the state found at 2.4 eV above the Fermi level. Again, the states related to the peaks close to the Fermi level, are

4.4. Electronic transport in molecules as a function of the conformation 78

the most important when a low voltage regime is considered and we will focus our discussion in these cases. We have also evaluated the I-V characteristics when a

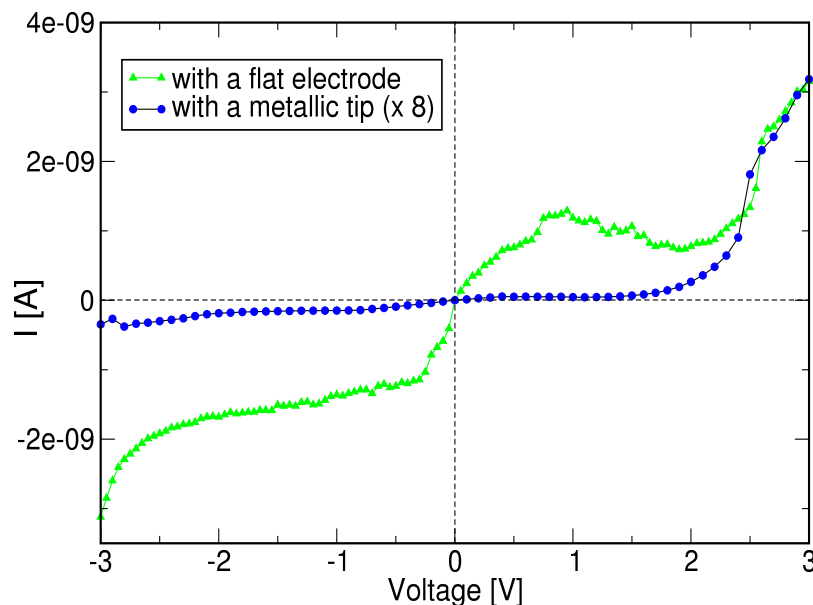


Figure 4.18: I-V characteristics of Styrene B considering different probes. Results using a flat electrode are compared two gold tips.

gold tip has been used and compared the result with the flat metallic electrode in Fig. 4.18. In this case we have focus our attention in the case when the surface has been p-type doped and a negative differential resistance effect has been found when a positive bias is applied. The current calculated when a tip is considered, has been amplified (8 times) for better comparison. From the figure, we can notice that the current has not been just diminished, but also the NDR effect has been suppressed when the tip is used.

4.4 Electronic transport in molecules as a function of the conformation

In this section we have considered the use a biphenyl molecule as an organic molecule to study the effect of conformational changes in the conductivity. The study of conductivity in these kind of molecules can give us a better idea about how suitable are these structures to be used as active electronic components. Experimentally

4.4. Electronic transport in molecules as a function of the conformation 79

there are some reports about how the conductance in single molecule junctions is modified when a finite temperature is considered and then a change in the structural conformation is obtained. Venkataraman *et al.* have observed that it is possible to consider an angular dependence in the transport properties of biphenyl molecules that are suitable [14]. In order to couple the molecule to the Au point contacts, they have used amino groups (for example NH_2) instead of thiol or isonitril groups obtaining more reliable conductance values.

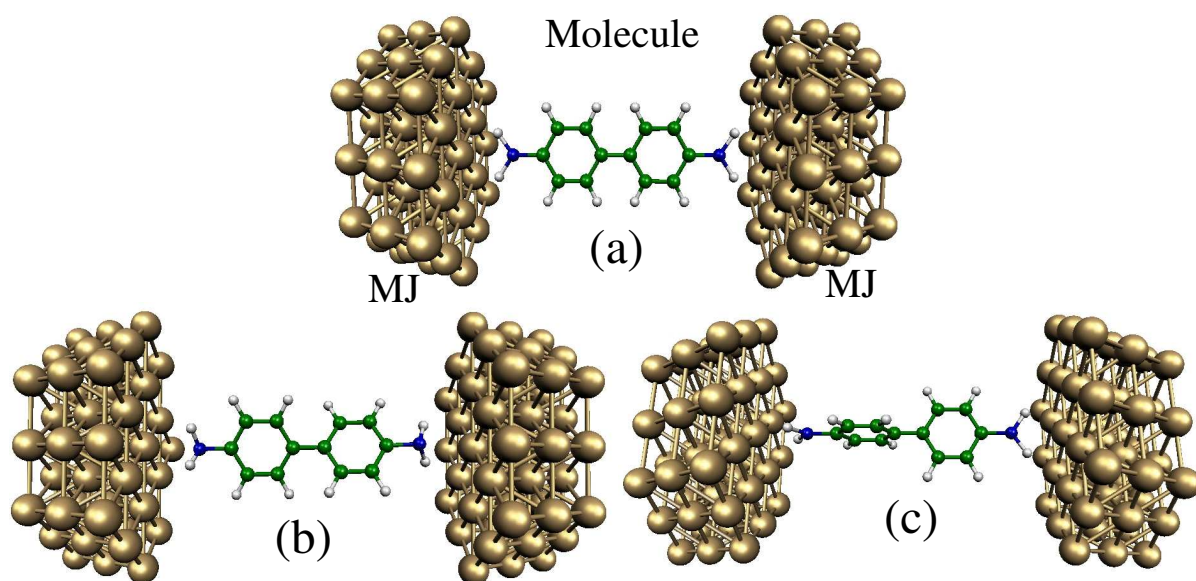


Figure 4.19: Configurations of the 4,4'-diaminobiphenyl molecule between two Au[111] surfaces used as metallic junctions (MJ). Three cases are defined according to the angles between carbon rings: (a) 0° , (b) 34° and (c) 90° .

Fig. 4.19 shows the configurations that we have chosen for the molecule. For these cases, the angle between both carbon rings (named as R-R angle) is defined. Initially we have considered that rings are: (a) R-R angle = 0, which means that both are in the same plane. Then we have selected two other R-R angles that will be compared with the first case. One of these corresponds to R-R = 90 degrees, where both rings are perpendicular to each other. The other case was obtained after the system has been optimized following a first principle calculations with a B3LYP approximation to find the lowest energy conformation, so $\text{Energy}(b) < \text{Energy}(a) < \text{Energy}(c)$. The electronic configuration that we have obtained with the EHT model

4.4. Electronic transport in molecules as a function of the conformation

provides a good agreement with the ab initio calculations and the main difference is located at the HOMO-LUMO difference which means that a better description of the parameters will be necessary.

The next step has been to locate these molecules between two metallic junctions, choosing Au[111] as a metallic surface. In order to join both molecule and electrodes, we have used amine like group (NH_2). The distance between surface and NH_2 groups has been fixed around 2.7 angstroms for each case. An external bias is applied

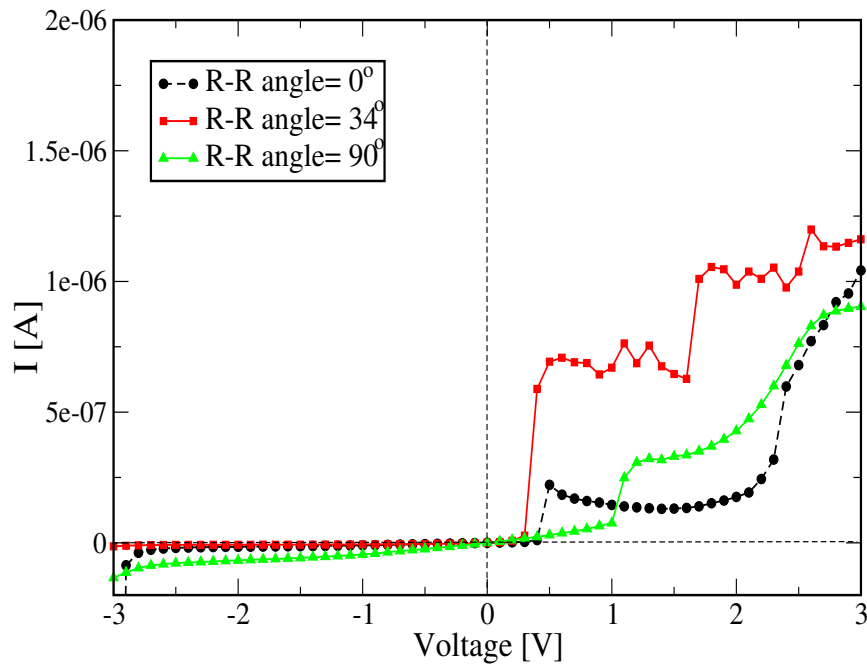


Figure 4.20: I-V characteristic for Biphenyl molecule as a function of the ring-ring angle. Current for 0° and 90° have been multiplied by 60 for better comparison.

between both electrodes, embedding the molecule in an external electric field. We have calculated the I-V characteristics for all cases and then shown in Fig. 4.20. Here the results for 0° and 90° have been amplified by 60 for better comparison. When a negative bias is applied, we can see a very small contribution to the current, but in contrast, when the bias is applied in the positive direction, an increase in the current is obtained at 0.4 V for R-R= 0° and 34° , and in the same way at 1.0 V we have an increase in the intensity for R-R= 90° . In order to evaluate the states that contribute to the electronic transport, we have calculated the differential conductance dI/dV . The main contribution to the conductance is given by the states located above the

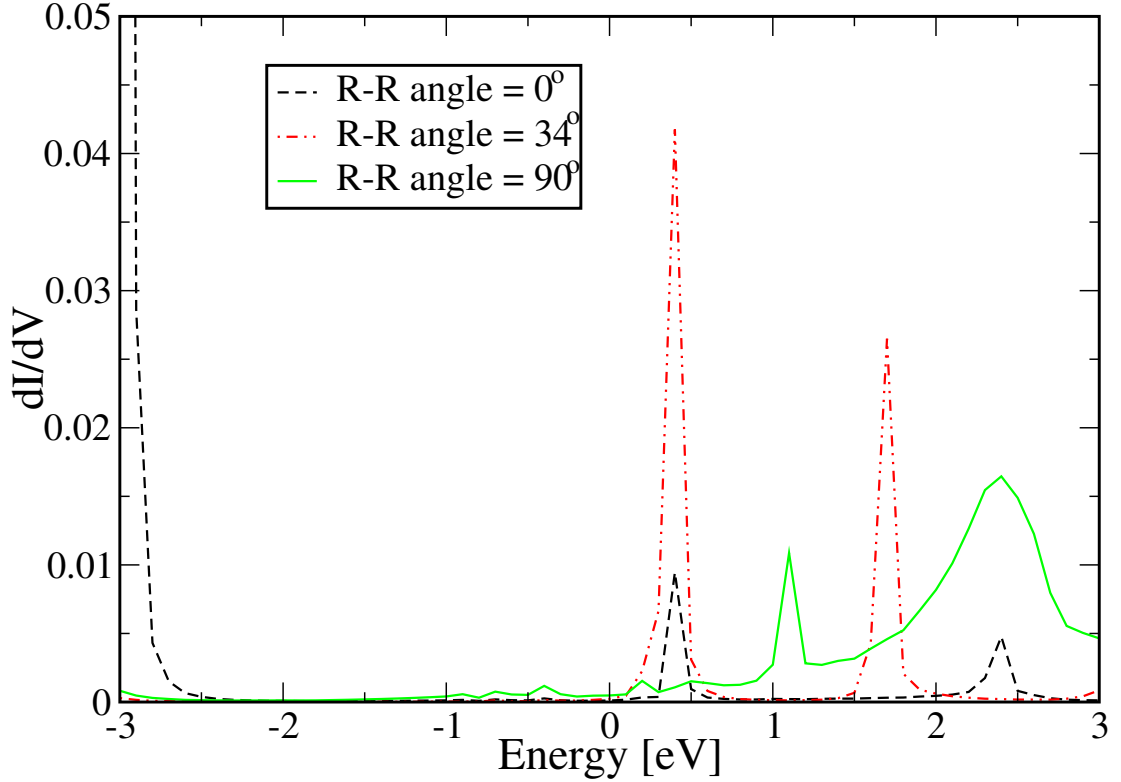


Figure 4.21: Differential conductance is calculated for different R-R angles.

Fermi level (zero position).

4.5 Discussion and Conclusions

Here, we have reported a set of electronic transport calculations for a semiconductor-cluster-electrode system. Initially we have obtained two possible configurations (A and B cases) for the styrene molecule given by the minimization of the energy associated to the surface-molecule system. The most stable configuration corresponds to the B case and the A case corresponds to the atomic configuration of the molecule used for Si[111] surface, as it is shown in Fig. 4.6. For the A case, we have obtained a NDR effect when a positive bias is applied. This can be understood based on the shifting of the molecular levels, close to the Fermi level, when the voltage is applied. This effect is modulated when the surface has been doped, which changes the chemical potential. This effect is more important for the case of a p-type surface, as it is observed in Fig. 4.6, when compared to the n-type surface, where the effect

is eliminated from the I-V characteristic. This difference is achieved because of the shift of the molecular levels according to each doped surface. For the n-type surface (with $\mu_s = -4.8$ eV), the electronic molecular levels are energetically located inside the energy gap of the silicon surface, so there is no channel available for the electronic transport at low positive bias (see dI/dV curve for n-type surface in Fig. 4.9). Another result, shows the influence of the tip in the electronic transport, where if the tip is changed, the NDR effect could be diminished with respect to the flat electrode. In order to compare both conditions, we have used a similar molecule-tip/electrode distance (5 angstroms). This can be understood from the potential created by the tip-surface, which is smaller than the potential created by the electrode-surface case. A smaller electric field created for a sharp tip promotes a very small shift of the energy levels of the molecule and then it is more difficult to move the states to the energy interval associated to the energy gap of Si[111]. For the second configuration (B case), the situation is rather different because there is no NDR when the undoped surface is considered. This can be concluded by observing that the main peak occurs at 0.7 eV above E_F and therefore can not be used as an electronic channel due to the energy gap of the Si[111]. Also, to control the NDR effect, we have considered doped surfaces, where it is possible to detect the NDR effect for the p-type surface but not for the n-type case. This difference is explained because the number of the channels available, and close to the Fermi level, is lesser for the undoped surface than for the p-type surface. Then the shifting of the states produced by the applied bias diminishes the contribution of the peak that is energetically displaced to the energy gap of the doped surface. In Fig. 4.16, we can see that the undoped surface and the n-type case do not show important peaks close to the Fermi level in the dI/dV characteristics and the most important contribution comes from the state located 2.3 eV above E_F . If we consider the p-type surface, we can see not only the contribution given by the states related to the dangling bonds of the surface around the Fermi level, but also one peak located at 0.7 eV above E_F and another one at 2.5 eV above E_F .

We have also evaluated the electronic transport in a biphenyl molecule when it is twisted respect to the carbon rings. The comparison between the different angles

shows that the bigger conductivity is given for the configuration with the lowest energy (b). In summary, the extended Hückel model, used to describe the electronic properties in the system, it is in good agreement when compared with *ab initio* calculations. We have found two stable configurations for the styrene molecule in contact with the surface and both of them can provide interesting properties like the NDR effect. This effect is modulated not only by the electronic molecular levels but also their positions respect to the energy gap of the silicon surface. A semiconductor surface has interesting properties respect to metallic ones, allowing to control transport with the appropriate conditions like doping. In our case, we have a NDR effect of the system at low positive voltage. This effect is also more important when a strong electric field has been considered to shift the molecular states (flat electrode produces a stronger electric field than a sharp tip). The comparison between flat and sharp electrodes has been performed for both configurations finding the same NDR suppression when a sharp metallic tip is considered. It is important also to notice that at a finite temperature the molecule can activate some vibrational modes or to be distorted and then to change the conductivity initially associated at low temperature. These results strength the idea to use organic molecules as possible components to storage information in electronic devices.

Bibliography

- [1] T. Rakshit, G.-C. Liang, A. W. Ghosh, and S. Datta. silicon—based molecular electronics. *Nano Letters*, 4:1803, 2004.
- [2] N. P. Guisinger, M. E. Greene, R. Basu, A. S. Baluch, and M. C. Hersam. Room temperature negative differential resistance through individual organic molecules on silicon surfaces. *Nano Letters*, 4:55, 2004.
- [3] M. A. Reed, C. Zhou, C. J. Muller, T. P. Burgin, and J. M. Tour. Driving current through single organic molecules. 278:252, 1997.
- [4] D. L. Klein, P. L. McEuen, J. E. B. Katari, R. Roth, and A. P. Alivisatos. *Appl. Phys. Lett.*, 68:2574, 1996.
- [5] H. Nejh. Incremental charging of a molecule at room temperature using the scanning tunnelling microscope. *Nature*, 353:640, 1991.
- [6] S. E. Baltazar, M. De Menech, U. Saalman, A. H. Romero, and M. E. García. Transport properties in styrene on an ideal si(111) surface: Negative differential resistance effect. *To be published*, 2007.
- [7] M. O. Watanabe, T. Miyazaki, and T. Kanayama. *Phys. Rev. Lett.*, 81:5362, 1998.
- [8] L. Bolotov, N. Uchida, and T. Kanayama. *Eur. Phys. J. D*, 16:271, 2001.
- [9] K. C. Pandey. *Phys. Rev. B*, 14:1557, 1976.
- [10] S. E. Baltazar, M. De Menech, U. Saalman, A. H. Romero, and M. E. García. Quantum electronic transport through supported $\text{si}_{29}\text{h}_{24}$ clusters on an ideal si(111) surface. *To be published*, 2007.

- [11] T. Kanayama. *Jpn. J. Appl. Phys.*, 33:L1792, 1994.
- [12] A. Khan. *Surf. Sci. Rep.*, 3:193, 1983.
- [13] F. G. Allen and G. W. Gobeli. *Phys. Rev.*, 127:150, 1962.
- [14] L. Venkataraman, J. E. Klare, C. Nuckolls, M. S. Hybertesen, and M. L. Steigerwald. Dependence of single molecule junction conductance on molecular conformation. *Nature*, 442:904, 2006.

Chapter 5

Nanostructures under hydrostatic pressure

5.1 Introduction

This chapter is mainly focused in the research started during the master's program about finite systems under an external pressure. The study of finite systems such as nanocrystals, fullerenes, clusters and molecular systems possesses important implications in biology [1], electronics [2], medicine [3], etc. It is well established nowadays that structural changes due to external forces, like tensile strain or hydrostatic pressure application, can change radically the electrical and mechanical properties of these structures. In particular, for carbon nanotubes, J. Cao and coworkers [4] have measured the electromechanical properties of suspended SWCNTs under stretching. From this study, they suggest that quasi-metallic SWNTs are potentially useful for highly sensitive electromechanical sensors (strain gauges, pressure sensors, etc). Also, exceptionally large reversible volume reduction upon high pressures in rope bundles of CNTs [5] reveals high storage of mechanical energy that future designs of energy-absorbing nanocomposite materials could take advantage of it. This observation on these type of materials can also be extrapolated to other finite systems, where external forces produce changes on some properties of the system, leading to a completely new behavior. This pursuing of new properties is one of the *leit-motifs* behind nanostructured materials science.

Considering systems under pressure, a large amount of studies at both classical and *ab initio* levels has been devoted to periodic systems since the introduction of molecular dynamics simulations in NPT ensembles [6, 7]. In these cases, the periodic cell volume is allowed to fluctuate in order to balance the applied pressure. In contrast, there have been just few studies of finite systems under pressure due to the lack of periodic boundary conditions. In this respect, there have been some approaches to simulate an applied external pressure on finite systems. For example, small to medium-size silicon nanocrystals have been studied by using a pressure-transmitting liquid [8–10]. Also, a finite hcp crystal was studied considering a spherical approximation of the volume [11]. Nanocrystals were also studied applying a volume definition based on atomic volumes [12] and a surface triangulation method was applied to study metallic clusters [13, 14]. In simulations of finite systems under external pressure, the volume of the structures becomes very important and so the most realistic calculation of volume is essential and an appropriate definition is necessary [15].

In this work, we focus on pressure applied to single wall carbon nanotubes. Since the first studies of carbon nanotubes [16], several theoretical and experimental studies about their mechanical [17–20], electrical [4, 21, 22], and optical properties [23, 24] have been reported. The possibility to use them in technological applications has inspired a large amount of studies characterizing their intriguing electronic behavior and their possible manipulation with external forces [4]. The success of these applications depends on several factors, like nanotube quality, chirality, and how an external force can affect its properties by changing its shape from the cylindrical configuration [17].

By following the recent literature on carbon nanotubes and their response to elastic deformations or application of pressure, one realizes that there is not yet an agreement on the elastic changes produced by pressure on crystalline single walled nanotubes. For example, Elliot *et al.* [25] and Tang *et al.* [19] have found that *bundle cross sections*, with a hexagonal structure, can achieve a polygonal phase when hydrostatic pressure is applied, while Chan *et al.* [26] find that the hexagonal microstructure is only metastable and the lowest energy should be an ellipsoid, similar

to the result found by Sluiter *et al.* for bundles of carbon nanotubes [27]. It is important to mention that elastic models predict for this case that the cross-section should be hexagonal [28]. This observation clearly contradicts the conclusion of Zang *et al.* [29], who reported agreement between atomistic models and elastic theories. Even though there are some publications indicating consensus [30], this is not a general outcome, which points to the need for further studies comparing and contrasting these two methods. The different results obtained from continuum mechanical theory and atomistic theory have been addressed by many authors [30,31], a point that is stressed out by Harik's quote: *The theory of shells may serve as a useful guide, but its relevance for a covalent-bonded system of only a few atoms in diameter is far from obvious* [31]. There is also a very recent discussion based on detailed atomistic calculations of some of the difficulties in applying continuum mechanics concepts to nanotubes [32].

The goal in this chapter is to simulate the action of external pressure on finite single-wall capped carbon nanotubes (SWCNTs). The simulation method used is aimed at modeling the effect of an average pressure on a finite nanostructure. The carbon-carbon interactions in the nanotubes are described by an empirical potential derived by Tersoff and Brenner from first principles calculations [33] and adapted by Maruyama [34]. We have considered finite SWCNTs with different chiralities and different lengths ranging from 4 up to 30 nm. Another parameter changed in this work is the temperature which affects the mechanical behavior of the nanotube. Our results are contrasted with those from Capaz *et al.* [35], that implemented the pressure reservoir method initially proposed by Martoňák, Molteni, and Parrinello [8] (MMP method), but using an extended Tersoff-Brenner interatomic potential. As a second check for our method, we did also implement the MMP method and calculated the pressure effects just in selected points with the same force field we used in our method. In general, the results presented below agree well with the Capaz implementation and our own.

In the next section we discuss briefly the basic ideas of our approach and how the pressure is applied, with some details about the simulations. In Sect. 3 we present the results. Finally, in Sect. 4 we present our discussion and conclusions.

5.2 Simulation method

The method presented in this paper is similar in spirit to the pressure reservoir method proposed by Martoňák, Molteni and Parrinello [8], where liquid particles interact mainly with surface atoms through short-ranged forces. In our case, the pressure acts only on particles on the surface but instead of a real pressure-transmitting medium, a suitably defined external force is used.

We start with a triangulated surface calculated on a capped carbon nanotube. The surface is obtained by following the quick-hull algorithm described in Ref. [36], where the minimal polyhedra enclosing a given structure can be obtained (see some applications for metallic clusters in Refs. [13,14]). Even though this algorithm is implemented on surfaces without any concavity, the method can be generalized by relaxing some of the searching parameters, introducing an error parameter which leads to a tighter triangulated surface, as in Ref. [37].

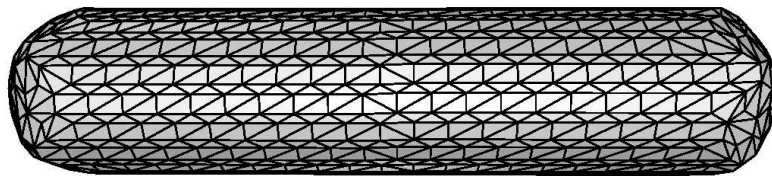


Figure 5.1: The surface of a (10,10) finite SWCNT (6 nm of length, 1020 carbon atoms) considering the triangulation surface method. The volume is calculated from the Gauss' theorem.

Since in our case all atoms are on the surface, the triangulation is performed only at the beginning of the simulation. In principle, it can be recalculated at any point during the simulation if necessary. An example of the output of the algorithm is presented in Fig. 5.1 for a capped single wall carbon nanotube. After the triangulation has been performed, the external pressure P is applied to the system as follows: taking a triangle (and its 3 vertices), the area A_m is calculated. The force applied on each plane is defined as $\vec{F}_m^{ext} = -PA_m\hat{n}$, where A_m and \hat{n} are the area and the normal vector associated to each triangular face. Subsequently, the force is proportionally distributed on the atoms (vertices) related to that triangle. Equations

of motion are obtained by adding this external force to the atomic interactions:

$$m_i \frac{\partial^2 r_{i,\alpha}}{\partial t^2} = F_{i,\alpha} + F_{i,\alpha}^{ext} \quad \alpha = x, y, z; \quad i = 1, \dots, N \quad (5.1)$$

where N is the number atoms on the surface, which is equal to the number of vertices of the triangulation and $F_{i,\alpha}^{ext}$ is the distributed force from the applied pressure.

In our simulations, the nanotubes were first thermalized at zero pressure and at a given temperature (usually 50 K), and then pressure was slowly increased up to 5 GPa in the case of (5,5) tube, and up to 2 GPa in the case of (10,10) tube. During the time where the pressure was kept constant, the temperature was maintained at the prefixed value by rescaling the velocity every 20 fs up to thermal equilibrium, where the rescaling was stopped. After the equilibrium is reached, the dynamical evolution was continued for 10/40 ps with a time step of 0.5 fs to perform the measurements. Other simulation parameters were exactly the same as the ones discussed in a previous publication [15].

5.3 Results

We applied the MD implementation discussed above to capped single wall carbon nanotubes. Since we are dealing with finite systems and we are interested in studying finite size effects, we considered throughout all our calculations two different nanotube lengths. According to the notation introduced by Harik [31], a nanotube is short or long if its aspect ratio, *Diameter* (D)/*Length* (L), is greater or less than 0.1, respectively. To study the case of long nanotubes (with aspect ratios much less than 0.1) we simulated tubes with length of 28.8 nm for (10,10) and 14.1 nm for (5,5) with aspect ratio of 0.047 and 0.048 respectively. For the short case, we have considered a length of 5.3 nm (0.256 for aspect ratio) for (10,10) and 4.5 nm (0.151) for (5,5) case. The change in nanotube length helps us to rationalize some of our observations and to see possible dependences on this physical parameter.

Molecular dynamics simulations were performed by using a classical semiempirical potential derived from first principles calculations, also known as the Tersoff and Brenner potential [33], with corrections introduced by Yamaguchi and Maruyama [34]. To check our findings, we compared some of our results with the

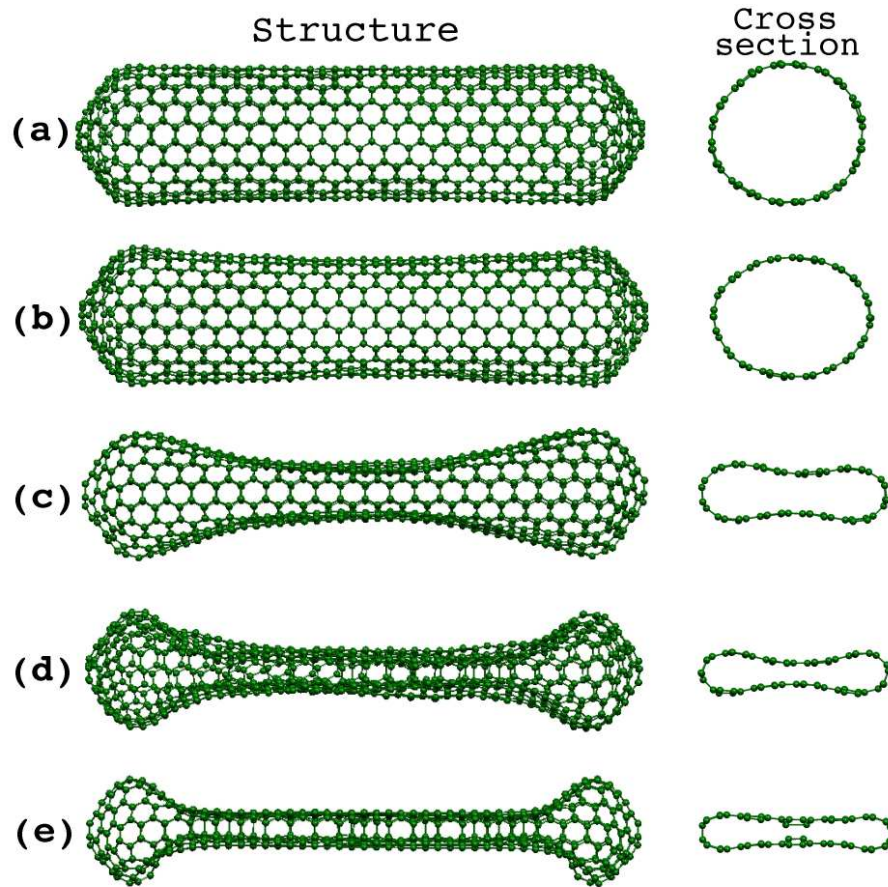


Figure 5.2: Snapshots at different pressures for a (10,10) armchair nanotube, 60 Å long, consisting of 1020 atoms and at a temperature of 50 K. In (a) we obtain a cylindrical structure applying 0.2 GPa, in (b) the shape is ellipsoidal at 1.1 GPa and for (c), (d) and (e) a peanut-shape structure is obtained for 1.2, 3.0 and 6.0 GPa respectively. Notice that as the pressure is increased, the nanotube have less freedom to vibrate along the radial direction and at some specific pressure, the system prefers to bend.

ones obtained from classical MD simulations using the MMP method, as reported by Capaz *et al.* [35] and a similar simulation implemented by ourselves. We start our discussion with the case of a short nanotube (10,10). Figure 5.2 presents several snapshots of the nanotube at different values of the applied pressure and at a very low temperature. Here, both the axial and the cross section are shown, in the order of increasing pressure from top to bottom. At 0.2 GPa, (a), the nanotube in average preserves a cylindrical structure, where the only change is a shortening of the C-C

bond distance as well as a reduction of the amplitude of radial vibrations such as the breathing mode. At 1.1 GPa, (b), the nanotube becomes elliptical and develops a large curvature along its axis. The caps remain rather rigid and there is only a small decrease of the C-C distance and a small change in curvature along the nanotube axis, mainly due to the difference of rigidity between the center and the caps, as well as at the transversal direction, where a small excentricity is obtained. In average, its principal structural shape remains similar to that at low pressures. At 1.2 GPa, (c), and 3.0 GPa, (d), a transition to a peanut structure is observed as it has been reported previously by some authors [25, 29, 35]. At 6.0 GPa, (d), the pressure is rather large and the nanotube is approaching a very elongated structure, where two planes interact. After a further slight increase of the pressure, the nanotube breaks down. This elastic behavior is generally observed in all kinds of simulated nanotubes (shorter or longer), the only major difference is in the transition pressure value. It is noteworthy that beyond 3.0 GPa we observe a rocking mode, *i.e.*, the nanotube exhibits a torsion around its principal axis before the cross section becomes planar. This mode cannot be observed in the case of infinite nanotubes (with periodic boundary conditions) [29, 35]. This vibrational mode could be observed experimentally, for example by Raman spectroscopy, if the nanotube under pressure is free at both ends as in our finite systems.

By increasing the applied hydrostatic pressure, SWCNTs are able to excite different radial or axial vibrational modes that are responsible for the observed structural transitions. This can be concluded by analyzing the velocity autocorrelation function (VACF). Some of the vibrational peaks appearing at low pressures disappear as the pressure is increased. This observation is consistent with recent experimental results, where shifts of the radial modes for SWCNTs bundles were observed as the pressure was applied [18, 38]. In those experimental works, bundles of nanotubes are immersed in a gasketed diamond anvil cell filled with methanol-ethanol as a pressure transmitting medium. To study the behavior of the radial breathing mode frequency, ω_R , as function of the nanotube diameter, Venkateswaran *et al.* [39] was able to fit the experimental data with a functional form obtained from a simple elastic model. Beyond the transition pressure, where the nanotubes have passed to

have a noncircular cross section, the breathing mode has changed its symmetry and other vibrational modes become more important. These modes can provoke abrupt transitions by combining their effects (increasing or changing anisotropically the atomic mean square amplitude in different directions and disrupting carbon-carbon bonds). Even though recognizing vibrational modes from a velocity autocorrelation function (VACF) analysis could be difficult, we were able to assign the breathing mode for very low pressures and we did obtain an inverse of the diameter dependence as reported in Ref. [18]. An accurate description of the vibrational modes should be obtained from the force constants obtained from a static calculation.

The behaviour of the vibrational modes across the transition the transition has been also analyzed by calculating again the VACF. We considered just 3 cases: 0.0, 0.6 and 1.2 GPa for (10,10) tubes and 0.0, 4.0 and 10.0 GPa for (5,5), and analysed the main peaks observed for each case. These results showed that before the transition which is located at 1.2 GPa for (10,10) and at 8 GPa for (5,5), peaks at values close to the experimental radial breathing and axial modes were found. After the structural transition, those peaks related to the circle-oval cross section are reduced or suppressed for both (5,5) and (10,10) tubes. Moreover, frequency peaks in the power spectra are diameter tube dependent, particularly the radial breathing mode (RBM) ω_R that has been calculated for (6,0), (5,5), (15,0), (10,10) and (20,0) tubes. We have obtained that RBM decreases with the diameter following the fitting curve D^{-1} which is the same behavior reported in Refs. [39, 40].

This kind of structural changes was studied by Raman spectroscopy techniques reported by Venkateswaran *et al.* [18]. They examined the pressure dependence of the radial and tangential vibrational modes and observed that the radial mode intensity decreases beyond 1.5 GPa for diameters associated with (10,10) nanotubes, suggesting that the system undergoes a phase transformation. Also, Peters *et al.* [41], based on Raman shifts, have determined a structural phase transition at 1.7 GPa on nanotubes with an average diameter of 13.5 Å.

for the transition. Chesnokov *et al.* also found that nanotubes still undergo reversible deformations up to this pressure. It is important to note that the majority of experiments have been performed on nanotubes bundles where confinement

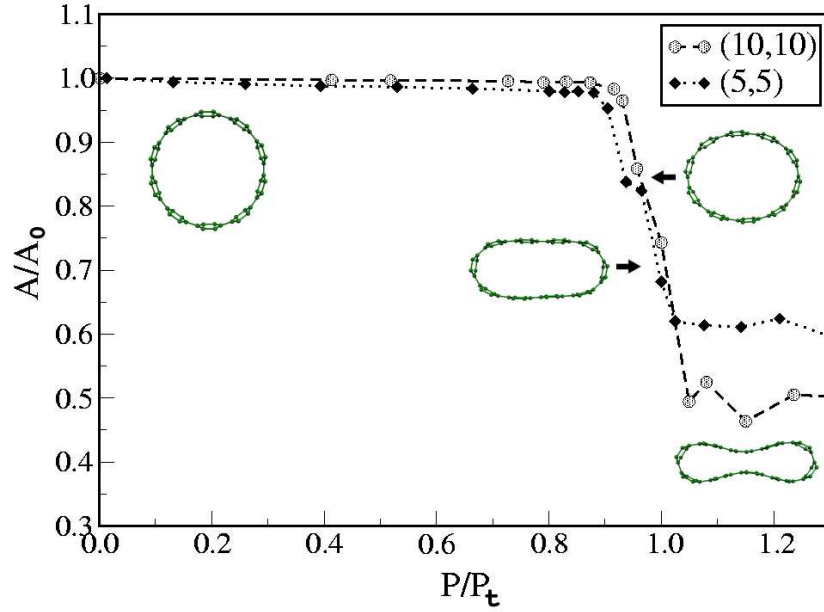


Figure 5.3: Cross sectional area as a function of pressure for capped (5,5) and (10,10) nanotubes. Statistics were collected and averaged during 10 ps, after thermodynamic equilibrium is reached. Here, pressure has been normalized to the transition pressure (see text).

affects the transition pressure. The Fig. 5.3 shows the behavior of the normalized cross sectional area (A/A_0) for long (5,5) and (10,10) nanotubes as a function of the reduced pressure (P/P_t) at a temperature of 100 K. The reduced pressure is calculated by dividing the pressure P by the transition pressure (P_t) defined as the pressure at the maximum value of the slope of the A vs. P curve. Upon increase of pressure, we can clearly distinguish two different regimes. At low pressures we observe a slow compression which corresponds to the gradual change from circular (area A_0 , $P = 0$) to an oval shape. In this regime we also observed fluctuations between the circular and the oval shape. This shows that the sharp transition from the circular to the oval shape, as suggested from $T = 0$ calculations by Zang *et al.* [29], does not exist at finite temperature. Upon further increase of pressure we observe an abrupt drop at P_t where the shape rapidly changes from oval to peanut (area A_1). From Fig. 5.3 we can see that this behaviour is the same for different nanotubes, which indicates that the scenario of the structural change is independent of nanotube diameter. However, we have verified that the ratio A_1/A_0 is different for

the two tubes. These results are in agreement with the collapse transition of Capaz *et al.* [35] and the loading curves shown by Elliott *et al.* [25]. On the other hand our results differ from those of Zang *et al.* [29] since we find that at finite temperature the oval shape of the cross section is neither unique nor stable.

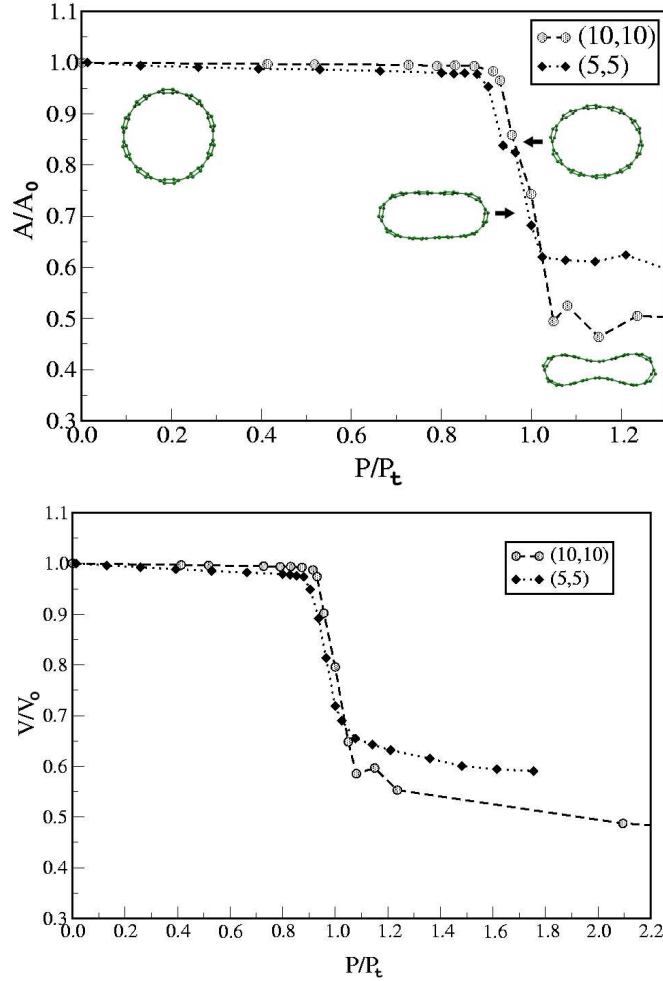


Figure 5.4: Volume as a function of applied pressure at different temperatures for a (5,5) nanotube (370 atoms) of length of 42 Å (upper panel) and for a (10,10) nanotube (920 atoms) of length of 53 Å (lower panel).

In order to systematically study the temperature effect on the pressure-induced structural transitions, we chose to focus on the case of short nanotubes for both studied chiralities. Simulations were performed at several temperatures: 50, 100, 200, 300 K for (5,5) nanotube and 50, 100, 200, 400 K for a (10,10) nanotube. The results are shown in Fig. 5.4. In general, with increasing temperature the abrupt

structural transition from circular to a flattened cross section becomes broader and more smooth. Similar effects are also found in the case of longer tubes, which indicates that the temperature effects are rather independent of the nanotube length.

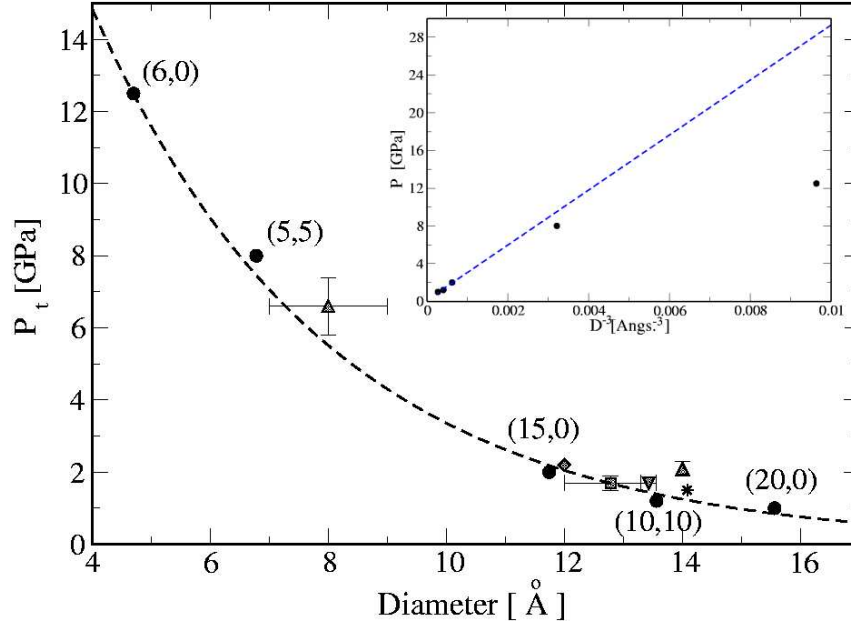


Figure 5.5: Transition pressure as a function of the tube diameter, D . Dashed line is a guide line through our calculated circular points (see text for details). Up triangles come from Ref. [25], diamond symbol is coming from Ref. [38], star symbol is from Ref. [19], square symbol comes from Ref. [18] and down triangle is from Ref. [41]. Inset tests the D^{-3} functional fitting for all diameters.

Finally, we studied the transition pressure as a function of the tube diameter. This dependence can be already seen in Fig. 5.4 and is of great practical importance as it may have a great impact in the design of electromechanical sensors (pressure sensors) or mechanical energy storage devices using carbon nanotubes. If the devices contain mixtures of carbon nanotube with different diameters, the response to pressure can be obscured by a combination of different elastic deformations of the nanotubes. In Fig. 5.5 we show the transition pressure as a function of the tube diameter as obtained for the longest considered nanotubes. The transition pressure decays rather fast and beyond a diameter of 12 Å it becomes very small. For large nanotube diameters, the behavior can be interpolated very close to a D^{-3} functional form obtained from continuum arguments (here D is the nanotube diameter) [42].

For small nanotube diameters, the D^{-3} fails to reproduce the simulations, which is related to the fact that in this regime the continuum approximation is no longer valid as the nanotube diameter becomes comparable to the carbon-carbon distance. In general, our predictions are in fair agreement with reported experimental results as represented by symbols in the same figure. It is important to mention that these experimental values have been obtained for nanotube bundles and represent an average over a large number of nanotubes with different diameter and chirality. There is also an important difference between an isolated carbon nanotube and one in a bundle since the confinement effect due to the other nanotubes changes both the rigidity and the transition pressure. On the other hand, we find a good agreement when comparing our results with those reported in other theoretical calculations, like the one by Capaz *et al.* [35].

Discussion and Conclusions

The study of the properties of isolated carbon nanotubes is becoming of great importance due to the recent developments in producing those nanotubes. On the other hand, there are only few experimental and theoretical results regarding the mechanical and structural properties of isolated SWCNTs under applied pressure. From the theoretical side, Yakobson *et al.* [30] and Cornwell and Wille [43] used the Tersoff-Brenner [33] many-body interatomic potential for carbon-made systems for simulations of SWCNTs under generic mechanical loads: axial compression, bending and torsion. Yakobson *et al.* found a singular behavior of the nanotube energy at certain strain levels that corresponds to abrupt changes in morphology, which they explained within a continuous tubule model. Also, Cornwell and Wille [43] found that under axial compression, nanotubes deform plastically once a certain critical threshold strain is reached, this behavior being dependent of the tube radii. The cylindrical structure and the asymmetry along one of the directions result in different rigidity along different directions of the nanotube. In particular, the axial direction has a high rigidity compared with the radial direction and this property is clearly reflected in the deformation pattern of the nanotubes under pressure. While

the nanotube undergoes quite dramatic changes in the radial direction, there is almost no change of the caps.

It is clear from Fig. 5.3 (see also Fig. 5.2) that upon increasing pressure a single transition, from an oval to a peanut cross section shape, is observed. The transition pressures obtained from our simulations are in good agreement with recently published results [25]. The rapid transition of the cross section from the oval one to a peanut starts in the middle of the nanotube and propagates towards the ends. Since our hydrostatic pressure implementation uniformly applies pressure on the whole system, these computational experiments are well suited to calculate the radial compressibility of SWCNTs, which can be directly compared with experimental measurements. We calculated the volume compressibility $\kappa = -\frac{1}{V} \frac{\partial V}{\partial P}$ in the elastic regime at different temperatures for the short (10,10) nanotube, and found a good agreement with experimental values. We have found a pronounced temperature dependence of κ , where the compressibility values range from 0.015 to 0.05 GPa⁻¹ when T changes from 100 K up to 400 K. The value at $T = 300$ K for short and long (10,10) tubes is $\kappa = 0.03$ GPa⁻¹ and $\kappa = 0.034$ GPa⁻¹, respectively. These values are in good agreement with the experimental results of $\kappa = 0.024$ GPa⁻¹ (Tang *et al.* [19]) and $\kappa = 0.028$ GPa⁻¹ (Chesnokov *et al.* [5]). Theoretical calculations by Girifalco *et al.* [44] assuming a Lennard-Jones potential for the interaction between carbon atoms in a continuum model found the value of $\kappa = 0.022$ GPa⁻¹, and Tersoff and Ruoff [28] by using a similar model found $\kappa = 0.011$ GPa⁻¹, which are also in fair agreement with our results.

From Fig. 5.5 we can also conclude that the transition pressure depends only on the diameter of the nanotube but not on its chirality. This agrees with conclusions of a recent paper [25] where Elliott *et al.* reported that the collapse of SWCNTs under hydrostatic pressure is diameter dependent ($1/D$ for low diameters), and that this collapse does not depend on the nanotube chirality. We found a D^{-3} behavior of the transition pressure for large nanotube diameters with strong deviations in the case of small diameters, where the elastic theory fails. This observation is in agreement with results published by Elliott *et al.* [25] and also agrees with the $1/D^3$ behavior suggested by Capaz *et al.* [35] at large diameters.

To summarize, in this work we used a surface definition based on the Delaunay's triangulation which provides a fairly good estimation of the surface and volume of the finite system under consideration. The agreement between reported experimental work and our simulations confirms that our methodology is appropriate. The external pressure has been taken into account by applying external forces to the triangulation surface surrounding the structure. The methodology is used to study the behavior of finite capped SWCNT's under pressure and to characterize the shape changes as function of pressure. We discuss how those changes depend on the nanotube diameter, chirality and temperature. At small pressures (in the elastic regime), the nanotube response to pressure has been discussed extensively in the literature and we find a fair agreement with those observations. In particular, the dependence of the frequency of the RBM on the diameter is found. Also, we studied the behaviour of some relevant peaks in the power spectra across the structural transitions. With respect to the structural transitions (circular to peanut), we find agreement with previous calculations and experiments **but not with Zang et al.** We find that the transition pressure is diameter dependent following a D^{-3} decay for large nanotube diameter (as predicted from elastic theory). The transition pressure is also in fair agreement with experimental results for small nanotube diameters where the elastic theory does not hold anymore.

Bibliography

- [1] C.Á. Mirkin, R.Ĺ. Letsinger, R.Č. Mucic, and J.Ĵ. Storhoff. A dna-based method for rationally assembling nanoparticles into macroscopic materials. *Nature*, 382:607, 1996.
- [2] A. Star, J.-C. Gabriel, K. Bradley, and G. Grüner. Electronic detection of specific protein binding using nanotube fet devices. *Nano Lett.*, 3:459, 2003.
- [3] D.P. ONeal, L.R. Hirsch, N.J. Halas, J.D. Payne, and J.L. West. Photo-thermal tumor ablation in mice using near infrared-absorbing nanoparticles. *Cancer Lett.*, 209:171, 2004.
- [4] J. Cao Q. Wang and H. Dai. Electromechanical properties of metallic, quasimetallic and semiconducting carbon nanotubes under stretching. *Phys. Rev. Lett.*, 90:157601, 2003.
- [5] S.Á. Chesnokov, V.Á. Nalimova, A.Ĝ. Rinzler, R.Ĕ. Smalley, and J.Ĕ. Fisher. Mechanical energy storage in carbon nanotube springs. *Phys. Rev. Lett.*, 82:343, 1999.
- [6] H.Č. Andersen. Molecular dynamics simulations at constant pressure and/or temperature. *J. Chem. Phys.*, 72:2384, 1980.
- [7] M. Parrinello and A. Rahman. Crystal structure and pair potentials: A molecular-dynamics study. *Phys. Rev. Lett.*, 45:1196, 1980.
- [8] R. Martoňák, C. Molteni, and M. Parrinello. Ab initio molecular dynamics with a classical pressure reservoir: Simulation of pressure-induced amorphisation in a $si_{35}h_{36}$ cluster. *Phys. Rev. Lett.*, 84:682, 2000.

- [9] M. Parrinello C. Molteni, R. Martoňák. *J. Chem. Phys.*, 114:5358, 2001.
- [10] R. Martoňák, L. Colombo, C. Molteni, and M. Parrinello. *J. Chem. Phys.*, 117:11329, 2002.
- [11] A. I. Landau. A new method of molecular dynamic computer simulation at constant temperature and pressure. *J. Chem. Phys.*, 117:8607, 2002.
- [12] D.Ÿ. Sun and X.Ĝ. Gong. Structural properties and glass transition in al_n clusters. *Phys. Rev. B*, 57:4730, 1998.
- [13] F. Calvo and J. P.Ě. Doye. Pressure effects on the structure of nanostructures. *Phys. Rev. B*, 69:125414, 2004.
- [14] J. Kohanoff, A. Caro, and M. W. Finnis. *CHEMPHYSCHEM*, 6:1848, 2005.
- [15] S.Ě. Baltazar, A.Ĥ. Romero, J.Ĺ. Rodríguez-López, H. Terrones-Maldonado, and R. Martonak. Assessment on isobaric-isothermal (npt) simulations for finite systems. *COMPUTATIONAL MATERIALS SCIENCE*, 37:526, 2006.
- [16] S. Iijima. Helical microtubules of graphitic carbon. *Nature*, 354:220, 1991.
- [17] M.R. Falvo, G. J. Clary, R. M. Taylor, V. Chi, F. P. Brooks, S. Washburn, and R. Superfine. Bending and buckling of carbon nanotubes under large strain. *Nature*, 389:582, 1997.
- [18] U.Ď. Venkateswaran, A.Ĺ. Rao, E. Richter, M. Menon, A. Rinzler, R.Ě. Smalley, and P.Ě. Eklund. Probing the single-wall carbon nanotube bundle: Raman scattering under high pressure. *Phys. Rev. B*, 59:10982, 1999.
- [19] J. Tang, L. Qin, T. Sasaki, M. Yudasaka, A. Matsushita, and S. Iijima. Compressibility and polygonalization of single-walled carbon nanotubes under hydrostatic pressure. *Phys. Rev. Lett.*, 85:1887, 2000.
- [20] G. Gao, T. Çagin, and W. A.Ĝoddard III. *Nanotechnology*, 8:184, 1998.
- [21] M.Ě. Nardelli and J. Bernholc. Mechanical deformations and coherent transport in carbon nanotubes. *Phys. Rev. B*, 60:R16338, 1999.

- [22] A. Maiti, A. Svizhenko, and M. P. Anantram. Electronic transport through carbon nanotubes: effects of structural transformation and tube chirality. *Phys. Rev. Lett.*, 88:126805, 2002.
- [23] S. Kazaoui, N. Minami, H. Yamawaki, K. Aoki, H. Kataura, and Y. Achiba. Pressure dependence of the optical absorption spectra of single-walled carbon nanotube films. *Phys. Rev. B*, 62:1643, 2000.
- [24] H. Jiang, G. Wu, X. Yang, and J. Dong. Linear optical properties of deformed carbon nanotubes. *Phys. Rev. B*, 70:125404, 2004.
- [25] J. A. Elliott, J. K. W. Sandler, A. H. Windle, R. J. Young, and M. S. P. Shaffer. Collapse of single-walled carbon nanotubes is diameter dependent. *Phys. Rev. Lett.*, 92:095501, 2004.
- [26] S.-P. Chang, W.-L. Yim, X. G. Gong, and Z.-F. Liu. Carbon nanotube bundles under high pressure: Transformation to low-symmetry structures. *Phys. Rev. B*, 68:075404, 2003.
- [27] M. H. F. Sluiter, V. Kumar, and Y. Kawazoe. Symmetry-driven phase transformations in single-wall carbon-nanotube bundles. *Phys. Rev. B*, 65:161402, 2002.
- [28] J. Tersoff and R. S. Ruoff. Structural properties of a carbon-nanotube crystal. *Phys. Rev. Lett.*, 73:676, 1994.
- [29] J. Zang, A. Treibergs, Y. Han, and F. Liu. *Phys. Rev. Lett.*, 92:105501, 2004.
- [30] B.I. Yakobson, C.J. Brabec, and J. Bernholc. Nanomechanics of carbon tubes: Inestabilities beyond linear response. *Phys. Rev. Lett.*, 76:2511, 1996.
- [31] V. M. Harik. Ranges of applicability for the continuum-beam model in the constitutive analysis of carbon nanotubes: Nanotubes or nano-beams. *Solid State Commun.*, 120:331, 2001.

- [32] M. J. Buehler, Y. Kong, and H. Gao. Deformation mechanisms of very long single-wall carbon nanotubes subject to compressive loading. *J. of Eng. Mater and Tech.*, 126:245, 2004.
- [33] J. Tersoff. New empirical model for the structural properties of silicon. *Phys. Rev. Lett.*, 56:632, 1986.
- [34] Y. Yamaguchi and S. Maruyama. A molecular dynamics simulation of the fullerene formation process. *Chem. Phys. Lett.*, 286:336, 1998.
- [35] R. B. Capaz, C. D. Spataru, P. Tangney, M. L. Cohen, and S. G. Louie. *Phys. Status Solidi B*, 241:3352, 2004.
- [36] C. B. Barber, D. P. Dobkin, and H. Huhdanpaa. The quickhull algorithm for convex hulls. *ACM Trans. Math. Softw.*, 22:469, 1996.
- [37] S. W. Hughes, T. J. D'Arcy, D. J. Maxwell, J. E. Saunders, C. F. Ruff, W. S. C. Chiu, and R. J. Sheppard. Application of a new discret form of gauss theorem for measuring volume. *Phys. Med. Biol.*, 41:1809, 1996.
- [38] J. Sandler, M. S. P. Shaffer, A. H. Windle, M. P. Halsall, M. A. Montes-Morán, C. A. Cooper, , and R. J. Young. Variations in the raman peak shift as a function of hydrostatic pressure for various carbon nanostructures: A simple geometric effect. *Phys. Rev. B*, 67:035417, 2003.
- [39] U. D. Venkateswaran, D. L. Masica, G. U. Sumanasekera, C. A Furtado, J. Kim, and P. C. Eklund. Diameter dependent wall deformations during the compression of a carbon nanotube bundle. *Phys. Rev. B*, 68:241406, 2003.
- [40] J. Kürti, G. Kresse, and H. Kuzmany. *Phys. Rev. B*, 58:R8869, 1998.
- [41] M. Peters, L. E. McNeil, J. P. Lu, , and D. Khan. *Phys. Rev. B*, 61:5939, 2000.
- [42] M. Levy. *Journal des Mathematiques Pures et Appliquees*, 10:5, 1884.
- [43] C. F. Cornwell and L. T. Wille. Simulations of the elastic response of single walled carbon nanotubes. *Comp. Mater. Sci.*, 10:42, 1998.

- [44] L.Á. Girifalco, Miroslav Hodak, and Roland S. Lee. Carbon nanotubes, buckyballs, ropes, and a universal graphitic potential. *Phys. Rev. B*, 62:13104, 2000.

Chapter 6

Conclusions

The present work, has been developed following the main goal to obtain a good description of molecular systems under equilibrium and non equilibrium conditions. Transport properties of molecules at surfaces have been calculated under several conditions and the possibility to control those properties has been also considered. We have study the influence of the molecule-surface interaction in the electronic transport finding interesting phenomena that are characteristic properties of electronic components.

From the work that has been made, we can come to the following conclusions:

- We found associated properties to clusters and surfaces such as: energy levels, band structures, densities of states, charge density by using several theoretical models to describe systems (Extended Hückel, local density approximation, etc.)
- The extended Huckel model, used to describe the electronic properties in the system, has been found in good agreement when compared with tight-binding and ab-initio calculations.
- For the silicon cluster $\text{Si}_{29}\text{H}_{24}$ on Si[111], a new peak in the DOS was found in the energy gap of the silicon surface, which is created by the cluster-surface interaction. The gap diminishes the effect of the new peak in the I-V characteristic as well as in the dI/dV case. The new state has a charge distribution

close to the surface and its position is unaffected by the external applied bias. In addition, for comparison, we have studied the influence of a metallic surface on the electronic transport through the molecule. In this case the ohmic behavior of the I-V characteristics is clearly observed in contrast to the diode-like behavior when a semiconductor surface is considered. The surface doping applied to consider a n-type and a p-type surface showed a small difference in the electronic transport due to the cluster-surface interaction.

- For the Styrene molecule $C_6H_5CH = CH_2$, we have found a negative differential resistance regime (NDR), which can be even observed for doped surfaces. This effect can be associated with the behavior of the molecular states close to the Fermi level. In this case, we have considered two geometric configurations for the molecule interacting with the surface. The presence of a negative differential resistance regime at positive bias is given by the shifting of the molecular levels that are close to the energy gap of the surface.
- Doped surfaces can act as controllers to change the transport properties and to increase or reduce effects like NDR. For the Styrene molecule, and considering both stable geometric configurations obtained from ab initio calculations, we have found a strong dependence of the doping effect. In the first configuration (the A case), the NDR effect is found for the neutral and the p-type surface. In contrast, if the B case is considered, only the p-type Si[111] surface shows a negative resistance that is due to the states getting closer to the energy gap of the surface. Additionally, we have considered the inclusion of sharp metallic tips in the metallic electrode finding that the NDR effect is suppressed. In this case the electric field created between the surface and the tip and acting on the molecule is smaller than in the case evaluated for the flat electrode.
- A non-metallic surface has interesting properties with respect to metallic ones, allowing to control the transport with the appropriate conditions. In our case, we have non-conducting behavior of the system at low (positive and negative) voltages. These results strengthen the idea to use silicon clusters as possible components in large-voltage valves or diodes in electronic devices.

- The importance of distortions in molecules, in order to evaluate the electronic conductance, has been considered in the study of organic molecules such as biphenyl molecules where we are studying the different responses associated to each system when natural distortions created by the vibrations are found.
- We have also developed our study in nanostructures under pressure following a classical molecular dynamics approach. In particular, the methodology is used to study the behavior of finite capped SWCNT's under pressure and to characterize the shape changes as function of pressure. We have also discussed how those changes depend on the nanotube diameter, chirality and temperature. At small pressures (in the elastic regime), the nanotube response to pressure has been discussed extensively in the literature and we find a fair agreement with those observations. In particular, the dependence of the frequency of the RBM on the diameter is found. In addition, we studied the behaviour of some relevant peaks in the power spectra across the structural transitions.

6.1 Future work

- We plan to study systematically the effect of distortion in organic molecules on their transport properties. We have evaluated the different responses when a molecule, like biphenyl, is considered to change its conformation finding a different response in their conductivity. In particular, the conformation with the lowest energy, has the bigger conductance, according to the I-V characteristics.
- Besides this, we are studying the electron-phonon interaction in electronic transport at different regimes (quantum and classical) [1–3]. In particular, temperature effect and the coupling between the molecule and the contacts can be studied following a classical or quantum point of view [1].

Regarding the part of this work related to quantum transport we have written two papers. The first paper is 'Quantum electronic transport through supported $\text{Si}_{29}\text{H}_{24}$ clusters on ideal Si[111] surface' that has been submitted to Journal of Applied

Physics and now is under review [4]. In this article, we did focus on the transport properties of silicon clusters deposited on a silicon buffer. Our paper shows how the electronic transport properties can change as a function of the cluster-surface interaction and how the cluster electronic states are modified as a function of the applied voltage. The theoretical approach is based on an extended Hückel theory to describe the electronic properties and the application of non-equilibrium Green's functions to calculate the transport properties.

The second paper is entitled: 'Negative differential resistance of styrene on an ideal Si[111] surface: dependence of the I-V characteristics on geometry, surface doping and shape of the STM-tip', to be submitted [5]. This article contains the I-V characteristics and the differential conductance of the Styrene molecule calculated using a self consistent approach based on non-equilibrium Green's functions. Two different adsorption configurations for the molecule on the surface were considered which corresponds to a global and a local minimum of the total energy. In both cases we find a negative differential resistance (NDR) in a given interval of bias voltages. In particular, this effect is controlled by the states available close to the Fermi level of the surface and can be manipulated by properly doping the substrate. The influence of a sharp metallic tip is considered comparing the I-V characteristics with the flat metallic electrode.

During this period we have also been working in other different projects. We can summarize them in the following list:

- We have continued working on the project about finite systems under pressure. The objective was to obtain reliable methods that could be applied to other finite nanostructures. These methods reveal the existence of new structures that could be metastable under normal conditions and with different mechanical and electrical properties under pressure conditions. This work was published with the title 'Assessment of isobaric-isothermal (NPT) simulations for finite systems', in the Computational Materials Science review [6]. Also, we have focused our attention on carbon nanotubes under pressure in order to see their mechanical response and considering different parameters such as temperature and diameter. The article 'Single walled carbon nanotubes under

hydrostatic pressure', has been submitted and published during the last year (2006). [7]

- SWCNTs under pressure have been also used as pressure cells of other molecular systems. In this direction, we are studying the effect produced in gold nanowires embedded in carbon nanotubes, finding some interesting properties about structural transitions, such as the formation of concentric layers.
- The doping effect in graphene sheet effect has been also theoretically studied to see how the electronic properties are modified when the surface is doped with S (sulphur) and P (phosphorous) atoms. The doped graphene has been found to have stable configurations being more stable the inclusion of phosphorous than sulphur. In the case of pirydinic sites, the absorption of molecules is more suitable taken into account the reactivity of the graphene sheet. This study opens the possibility to use these systems in nanocatalysis and/or as nanosensors [8].

Bibliography

- [1] A. Mitra, I. Aleiner, and A. J. Millis. Phonon effects in molecular transistors: Quantal and classical treatment. *Phys. Rev. B*, 69:245302, 2004.
- [2] J. Koch and F. von Oppen. Franck-Condon blockade and giant fano factors in transport through single molecules. *cond-mat*, page 0409667, 2004.
- [3] J. Koch, F. von Oppen, Y. Oreg, and E. Sela. Thermopower of single-molecule devices. *Phys. Rev. B*, 70:1951107, 2004.
- [4] S. E. Baltazar, M. De Menech, U. Saalman, A. H. Romero, and M. E. García. Quantum electronic transport through supported $\text{Si}_{29}\text{H}_{24}$ clusters on an ideal Si(111) surface. *submitted to Journal of Applied Physics*, 2007.
- [5] S. E. Baltazar, M. De Menech, U. Saalman, A. H. Romero, and M. E. García. Transport properties in styrene on an ideal Si(111) surface: Negative differential resistance effect. *To be published*, 2007.
- [6] S. E. Baltazar, A. H. Romero, J. L. Rodríguez-López, H. Terrones-Maldonado, and R. Martonak. Assessment on isobaric-isothermal (npt) simulations for finite systems. *COMPUTATIONAL MATERIALS SCIENCE*, 37:526, 2006.
- [7] S. E. Baltazar, A. H. Romero, J. L. Rodríguez-López, and R. Martonak. S. e. baltazar and m. de menech and u. saalman and a. h. romero and m. e. garcía. *JOURNAL OF PHYSICS-CONDENSED MATTER*, 18:9119, 2006.
- [8] Ale. Garcia, A. H. Romero, J. F. Perez Robles, S. E. Baltazar, and A. Rubio. Influence of s and p atoms on graphene sheet. *to be published*, 2007.